Lehrstuhl E15
Univ.-Prof. Dr. F. von Feilitzsch
Institut für Astro-Teilchenphysik
der Technischen Universität München

X-Ray Microanalysis with Transition Edge Sensors
The Future of Material Analysis
with Scanning Electron Microscopes

Christian Hollerith

Vollständiger Abdruck der von der Fakultät für Physik der Technischen Universität München zur Erlangung des akademischen Grades eines

Doktors der Naturwissenschaften

genehmigten Dissertation.

Vorsitzender:		Univ.- Prof. Dr. M. Kleber
Prüfer der Dissertation:	1.	Univ.- Prof. Dr. F. von Feilitzsch
	2.	Univ.- Prof. Dr. R. Krücken

Die Dissertation wurde am 30.05.2006 bei der Technischen Universität München eingereicht und durch die Fakultät für Physik am 05.07.2006 angenommen.

For Lisa

Abstract

In current experiments and technical applications the demand for new and advanced concepts for the detection of radiation and particle is increasing. Low temperature detectors such as Transition Edge Sensors (TES) have been developed as ultrahigh-resolution radiation and particle detectors offering advantages in manifold applications. They were designed primarily for astrophysical experiments such as the dark matter search. In material analysis they have been introduced to revolutionize mass spectroscopy of biological molecules and Energy Dispersive X-ray Spectroscopy (EDS). EDS is the determination of the elemental constitution of samples in scanning electron microscopes (SEMs) with characteristic X-ray radiation excited by the electron beam. The use of TES detectors improves the EDS analysis of small volumes such as particles or thin layers. This is especially important for the semiconductor industry because of the continual shrinking of device size. Current structure sizes of 65 nm are already demanding new approaches in analytic methodology.

In this thesis the introduction and improvement of a fully automated TES detector system in the industrial environment of a semiconductor failure analysis lab is described. This system, marketed under the trade name of 'Polaris' by the manufacturer, is based on a mechanical pulse tube cooler in combination with an adiabatic demagnetization refrigerator (ADR) for cooling the TES detector to its operating temperature. Several large improvements had to be made to the system during the total system integration. The energy resolution could be improved significantly thus enabling a better peak separation and the measurement of chemical shifts. Due to the small area of TES detectors compared with conventional EDS detectors the efficiency of the system proved to be too low for everyday use. A polycapillary X-ray lens was added to the system in order to solve this problem. The application of the lens, however, brought its own problems and appropriate and practicable adjustment methods had to be developed. With the lens the count rate could be increased by more than two orders of magnitude. In order to identify X-ray peaks correctly, an accurate energy calibration correcting the nonlinear behavior of the TES detector is absolutely necessary. A new approach to the linearization of TES has been developed and enables a calibration accuracy for TES spectra fulfilling all the needs of material analysis. This linearization method is also easy to handle for the future user of the system. With the achieved degree of automation and extended analysis possibilities such as a superior peak separation, a lower element detection limit and easy peak identification, TES-EDS spectrometers hold the potential to replace conventional Si(Li) detectors in the near future.

Contents

Chapter 1

X-Ray Microanalysis

X-ray microanalysis is the detection of characteristic X-rays produced during the interaction of a specimen with a high energy electron beam. It is a powerful and non destructive technique for revealing elemental information of a small area of a specimen. In combination with an imaging electron beam instrument such as a scanning electron microscope (SEM), X-ray microanalysis is capable of analyzing elements heavier than helium with a spatial resolution of less than a micrometer.

The X-rays generated by the electron beam can be detected with an energy dispersive spectrometer (EDS) or a wavelength dispersive spectrometer (WDS). Conventional EDS detectors are semiconductors such as high-purity germanium (HPGe) or lithium-drifted silicon detectors (Si(Li)). But for future applications also low temperature detectors such as transition edge sensors (TES) will be used in growing numbers due to their superiority to semiconducting detectors. WDS detectors use a diffracting crystal to select X-rays of a specific energy. Thus only one energy can be detected at once and therefore the measurement time for a complete X-ray spectrum is quite long.

X-ray microanalysis provides both, qualitative and quantitative information of structures with sizes well below one micrometer. The energy spectrum of the detected X-rays displays only the characteristic X-ray intensities of the elements in the specimen. But by understanding the X-ray generation process also the mass fractions of these elements can be calculated. So the X-ray spectrum also provides quantitative information about the specimen[1].

1.1 Electron-Specimen Interaction

When primary-beam electrons with energies larger than 1 keV penetrate a specimen they interact with the atoms in various ways [Wei04]. The interactions can be generally divided into elastic and inelastic interactions.

The interactions are elastic when only the momentum of the electrons is changed

[1] see section 6.5

while the energy remains nearly constant. The energy actually lost in an elastic process is in the order of magnitude of eV so that it can be neglected compared to the energy of the primary electrons. The cross-section $Q_{>\Phi}$ in the case of a deflection larger than the angle Φ is a function of the atomic number Z and the electron energy E [Wei04]:

$$Q_{>\Phi} \propto \frac{Z^2}{E^2} \tag{1.1}$$

This cross section is much larger for high-Z elements than for light elements. Thus, the amount of backscattered electrons that leave the specimen depends on the atomic number. Additionally, the lower the energy of the primary-beam electrons, the larger the cross section will be. So the probability for large changes of momentum due to elastic scattering increases with decreasing electron beam energy.

Interactions are deemed to be inelastic when the energy loss of the primary beam electrons is significant compared to their total energy. This energy loss generates various excitations in the specimen such as plasmons, high-energy phonons, conduction band electrons and X-rays [Wei04]. The spectroscopy of these excitations reveals various details about the specimen. The energy loss per unit distance covered by an electron due to inelastic interactions, dE/dx, can be approximated by Bethe's law [Bet33]:

$$\frac{dE}{dx} = 2 \cdot \pi \cdot e^2 \cdot N_0 \cdot \frac{Z \cdot \rho}{A \cdot E_m} \cdot ln(\frac{1.166 \cdot E_m}{(9.76 \cdot Z + 58.8 \cdot Z^{0.19}) \cdot 10^3 \cdot keV}) \tag{1.2}$$

where:

$N_0 =$ Avogadro's number

$E_m =$ Mean electron energy

$\rho =$ Density of the target material

The volume where the interactions between primary beam electrons and specimen take place is called the interaction volume. The size and shape of this volume depends on the mean atomic number of the specimen and the electron beam energy. For example, a high-energy electron in a low-Z material undergoes inelastic scattering losing its energy without large changes in direction. In a depth where the energy is low enough that elastic scattering becomes probable the direction of the electron changes significantly with time. So the interaction volume will be narrow where the beam enters the material and will widen with increasing depth (e.g. Carbon in fig. 1.1). This pear-shaped volume is typical for larger beam energies in EDS analysis. For high-Z materials or low beam energies elastic scattering is dominant from the beginning and the interaction volume will be more spherical. The shape of the interaction volume can be calculated using Monte Carlo simulations of the electrons in the specimen [Hov97]. Fig. 1.1 shows the interaction volume for dif-

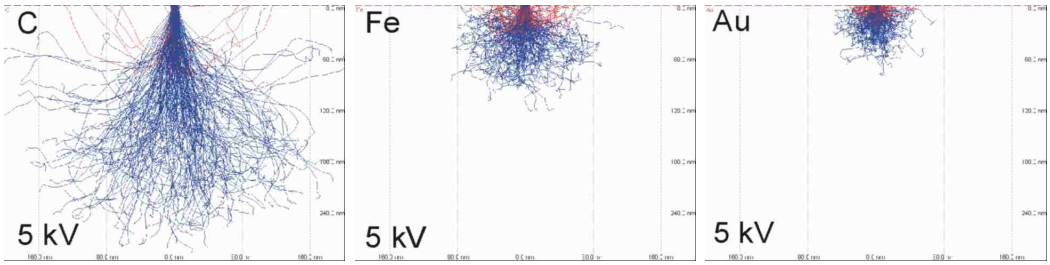

Figure 1.1: Monte Carlo simulations [Hov97] of 5 keV electron trajectories in different materials with increasing Z, from low (Carbon) to high Z (Gold); size of each simulation box is 400 nm·300 nm; red trajectories are backscattered electrons leaving the specimen, blue trajectories are absorbed electrons

ferent materials but with similar beam energies. For a low-Z material, carbon for instance, the volume is in total larger than that in heavier materials. Additionally, the electrons spread out with increasing depth. A similar behavior occurs if the

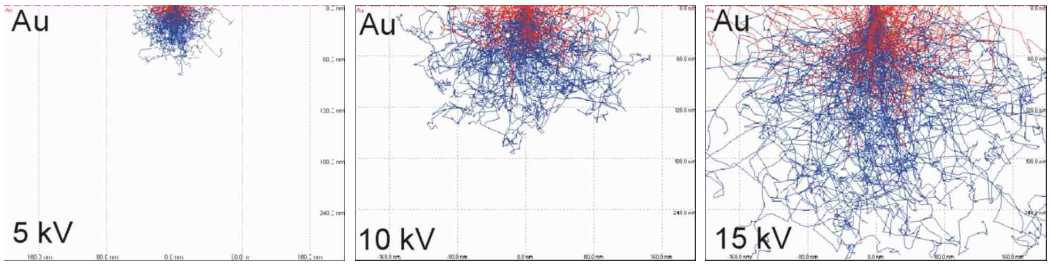

Figure 1.2: Monte Carlo simulations [Hov97] of electron trajectories with various energies in gold; size of each simulation box is 400 nm · 300 nm; red trajectories are backscattered electrons leaving the specimen, blue trajectories are absorbed electrons

beam energy is increased for the same material, as shown in fig. 1.2; the size of the interaction volume increases proportional to beam energy.

1.2 X-Ray Generation

The X-ray radiation emitted in the processes under study here can be divided into characteristic X-ray radiation and bremsstrahlung. Bremsstrahlung is generated by the inelastic scattering of primary electrons. The electrons are decelerated during this scattering and the energy loss is emitted as X-ray radiation with a continuous energy spectrum. The range of the spectrum is from nearly zero up to the energy of the incident beam. Bremsstrahlung is the main source of background in an electron beam excited X-ray spectrum [Fri03].

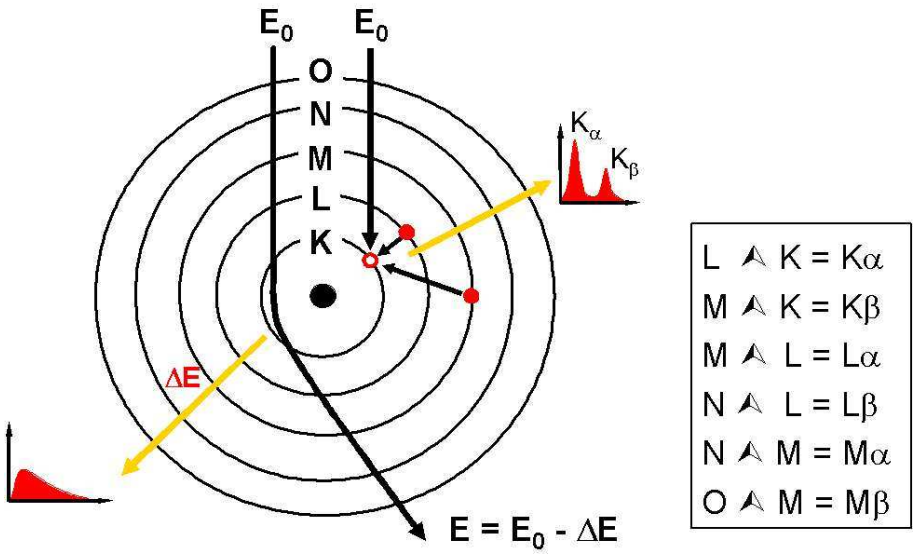

Figure 1.3: Schematic illustration of X-ray generation in an atom

If an electron with sufficient energy interacts inelastically with an atom it can cause the ejection of an inner shell electron, leaving the atom in an ionized state. The probability for this process is described by the ionization cross-section [Isa04] of the concurrent element and electron energy. The ionized state of the atom is unstable and results in an electron transition from an outer shell to fill the vacancy in the ionized atomic level (see fig. 1.3). The different transitions in an atom are described in section 1.3, a simplified illustration is shown in fig. 1.3. The released energy during this transition can be emitted as an X-ray or a so-called Auger electron. The Auger electron is emitted from the shell which is also the origin of the transition. The energy of this electron equals the difference between the transition energy and the energy of the shell from which it is ejected. The fraction of ionizations resulting in an X-ray emission and therefore not in an Auger electron emission, is called fluorescence yield. It increases with increasing atomic number Z and is also larger for K transitions than for L and M transitions as shown in fig. 1.4. So the yield is largest for high-energy transitions such as the K lines of heavy element whereas for low-energy lines Auger electron emission is dominant. Auger electron spectroscopy (AES) shows advantages for the detection of low-energy transitions in terms of emission yield whereas low energy X-ray spectroscopy has to deal with the disadvantage of a low yield. Therefore a good detection efficiency of the emitted X-rays is necessary.

A scanning electron microscope (SEM) generates an image of the sample by scanning with a fine focused electron beam across the sample. The electrons interact with the atoms of the specimen in various ways enabling different analysis methods. These interactions take place in the so called interaction volume as described in the

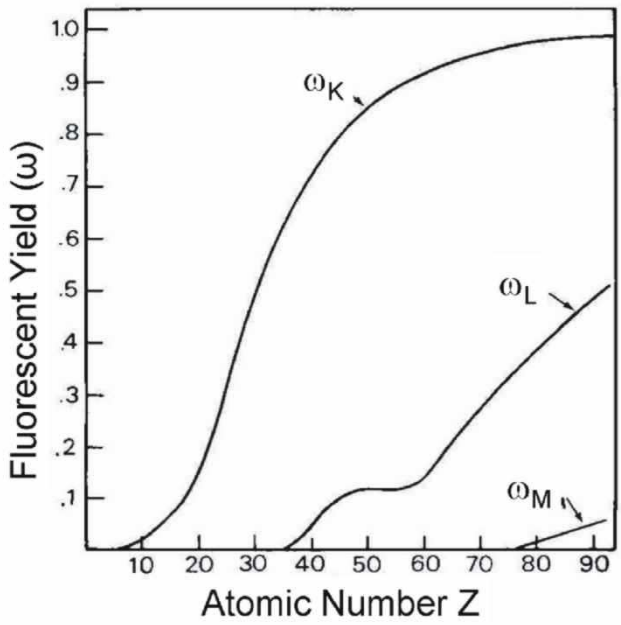

Figure 1.4: Fluorescence yield as function of atomic number for different transitions (K, L and M), [Fri03]

previous section. X-rays are excited in regions of the interaction volume where the electron energy is still larger than the ionization energy of a specific inner atomic shell. So the X-ray excitation volume is smaller than the total interaction volume. An approximation for the size of the excitation volume is given by [And66]:

$$R = \frac{0.064 \cdot (E_0^{1.68} - E_c^{1.68})}{\rho} \tag{1.3}$$

where:

$R =$ spatial resolution in μm (diameter of excitation volume)

$E_0 =$ beam energy in keV

$E_c =$ critical energy to ionize an inner atomic shell, leading to an X-ray transition

$\rho =$ mean density of the specimen in g/cm^3

In order to get optimum intensity from an X-ray emission line, the incident beam energy must be about three times larger than the critical excitation energy of an inner atomic shell [Fri03]. When this condition is fulfilled the excitation volume is approximately of the same size as the interaction volume and Monte-Carlo simulations for

the calculation of the interaction volume can also be used for the determination of the excitation volume.

The size of the excitation volume of the L line excitation volume of a medium-Z material such as Fe is about 100 nm for a beam energy of 5 keV. This is significantly larger than the structure size of contemporary semiconductor devices. Thus, in semiconductor EDS analysis low beam energies have to be used and therefore detectors are needed that are able to resolve all low-energy X-ray lines.

High-energy electrons entering a specimen generate X-rays due to the interaction with the matter of the specimen. But the generated X-ray intensity of a characteristic emission line is a function of the mass depth in the sample. The intensity is described by the depth distribution function Φ which is defined as the ratio of the X-ray intensity of an infinitesimally thin layer in mass depth ρz to the intensity of an identical layer in vacuum [Cas55]. Φ is measured with the so called tracer method as shown in fig. 1.5. A sample is prepared that contains a thin tracer layer buried in

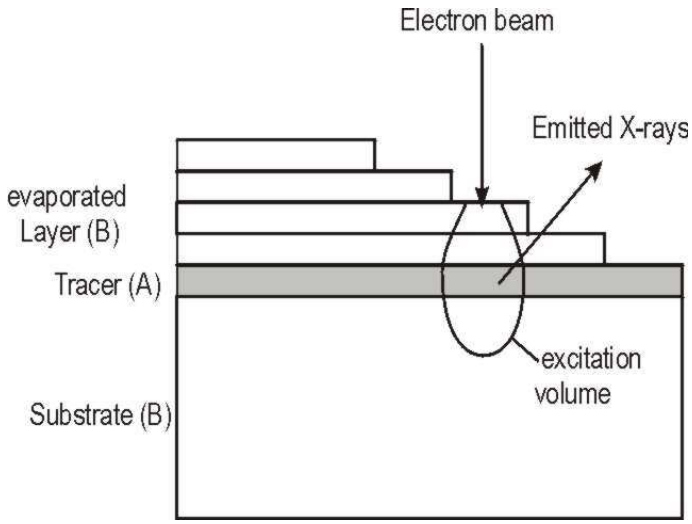

Figure 1.5: Sample used to measure $\Phi(\rho z)$ with the so called Tracer method

varying distance to the surface. The atomic number of the bulk material resembles to the atomic number of the tracer layer. Φ is the ratio of the intensity of the buried layer to the intensity of the tracer layer on a low-Z material such as boron or carbon. Calculating this ratio for varying depth, Φ can be measured as function of the mass depth. Using the so called PAP model [Pou91, Isa04] the depth distribution function Φ can be parametrized with two parabolas. This parametrization results in a good approximation of the measured function Φ. An example is shown in fig. 1.6.

The generation of X-rays takes place in the specimen where the primary electrons interact with the matter as described with $\Phi(\rho z)$. On their way through the sample some of the X-rays are absorbed. This has an influence on the X-ray intensity that is emitted by the sample. Beer's law (Eq. 1.4) describes the ratio of the transmitted

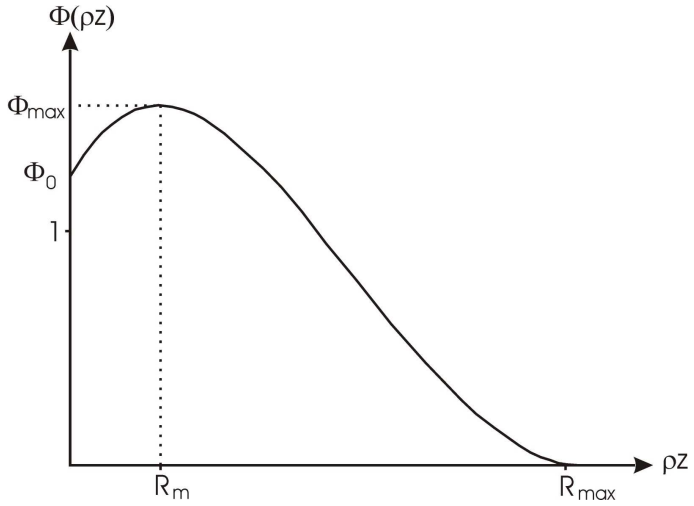

Figure 1.6: Depth distribution function Φ as function of mass depth ρz according to PAP model [Pou91, Isa04]

X-ray intensity I to the incident X-ray intensity I_0:

$$\frac{I}{I_0} = e^{-(\mu/\rho)\rho x} \tag{1.4}$$

with:

$\mu/\rho =$ the mass absorption coefficient of the absorbing material

$\rho =$ density of the material

$x =$ thickness of material

The mass absorption coefficient of the material depends on the mass absorption coefficients of the elements and their mass fractions C_i in the absorbing material:

$$(\mu/\rho) = \sum C_i \cdot (\mu/\rho)_i \tag{1.5}$$

The mass absorption coefficient of a specific component in the material is a function of its atomic number and the energy of the incident X-ray [Fri03]:

$$\mu/\rho = \frac{k \cdot Z^3}{E^3} \tag{1.6}$$

Eq. 1.6 is valid (k=const.) for energies between absorption edges of the element. These edges correspond to the energies of the various electronic levels in the atom. When the X-ray energy exceeds the shell energy, k changes abruptly because more electrons contribute to the absorption of the X-rays. This change is called absorption edge and it is shown in fig. 1.7.

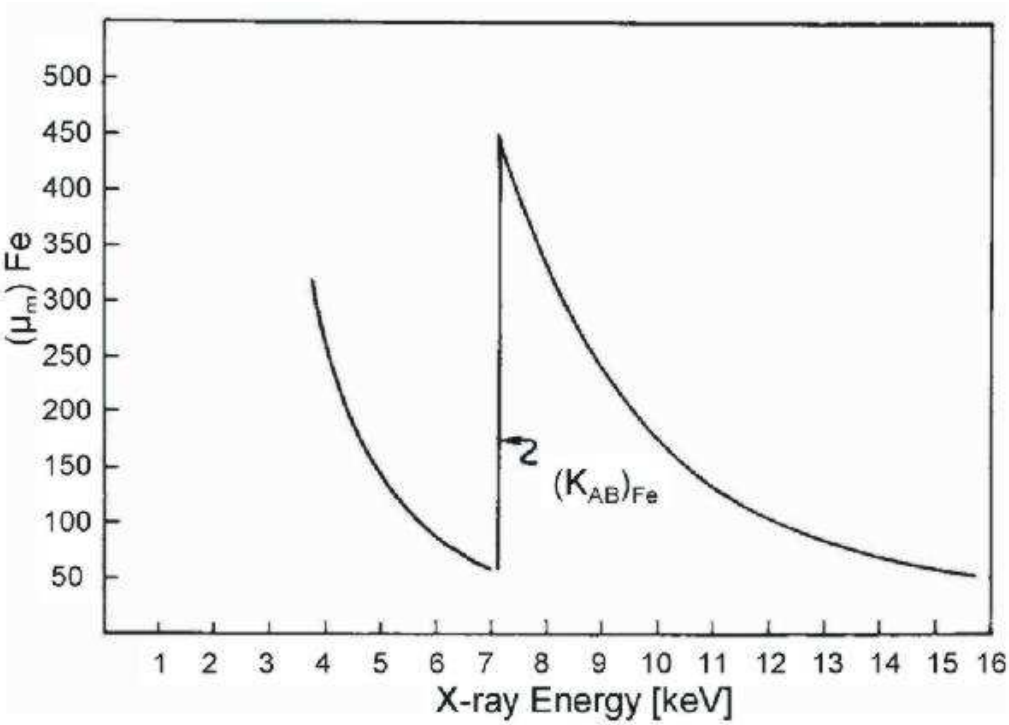

Figure 1.7: Absorption coefficient μ of Fe vs. X-ray energy [Fri03]

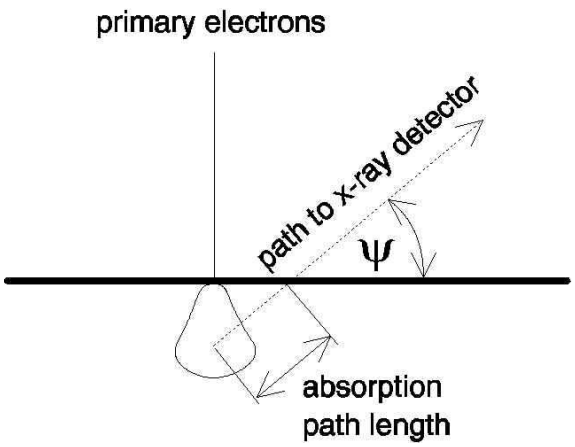

Figure 1.8: Illustration of the absorption path length in the specimen that is excited by an electron beam

The absorption length that a generated X-ray has to pass through before exiting the sample depends on the generation depth z and the take-off angle of the detector Ψ as shown in fig. 1.8. Beer's law for this case is:

$$\frac{I}{I_0} = e^{-(\mu/\rho)\cdot cosec(\Psi)\cdot z} \tag{1.7}$$

Absorption of X-rays leaves the absorbing atoms in an excited state. These atoms can lose their energy by emitting X-rays. This radiation is called fluorescence. It is generated in the volume illuminated by primary X-rays. This volume is typically much larger than the excitation volume generated by the primary electron beam. So also characteristic radiation of this volume contributes to the detected X-ray spectrum. Thus, elements can emerge in the spectrum that are not present in the excitation volume. However, this fluorescence intensity is much lower than the primary X-ray intensity and the influence of the fluorescence radiation on the measurement can be neglected.

1.3 X-Ray Emission Lines

An electron shell in an atom is described by its quantum numbers. These are [Wei04]:

$n =$ principal quantum number

$l =$ angular momentum quantum number, describes the angular momentum of the electron

$j = l \pm s$ spin-orbit quantum number

Shell	K	L			M				
n	1	2			3				
l	0	0	1		0	1		2	
j	1/2	1/2	1/2	3/2	1/2	1/2	3/2	3/2	5/2
E	K	L(I)	L(II)	L(III)	M(I)	M(II)	M(III)	M(IV)	M(V)

Table 1.1: Shells (E) assigned to atomic quantum numbers n, l, j [Wei04]

The atomic shell notation used for spectroscopy (E) connected with the atomic quantum numbers (n, l, j) is shown in table 1.1.

If an electron is removed of one of the inner shells, the generated hole is almost instantly filled by an electron from a shell with a larger principal quantum number n. For a radiating transition various selection rules have to be fulfilled [Wei04]:

$$\Delta n > 0,\ \Delta l = \pm 1;\ \Delta j = \pm 1, 0$$

	Initial Ionization Level								
	K	L_I	L_{II}	L_{III}	M_I	M_{II}	M_{III}	M_{IV}	M_V
L_I									
L_{II}	$\mathbf{K\alpha_2}$								
L_{III}	$\mathbf{K\alpha_1}$								
M_I			$L\eta$	Ll					
M_{II}	$K\beta_3$	$L\beta_4$		$L\sigma$					
M_{III}	$\mathbf{K\beta_1}$	$L\beta_3$	$L\beta_{17}$	$L\tau$					
M_{IV}	$K\beta_5$	$L\beta_{10}$	$L\beta_1$	$\mathbf{L\alpha_2}$					
M_V	$K\beta_5$	$L\beta_9$		$\mathbf{L\alpha_1}$					
N_I			$L\gamma_5$	$L\beta_6$					
N_{II}	$K\beta_2$	$L\gamma_2$						$M\zeta_2$	
N_{III}	$K\beta_2$	$L\gamma_3$							$M\zeta_1$
N_{IV}	$K\beta_4$		$L\gamma_1$	$L\beta_{15}$			$M\gamma_2$		
N_V	$K\beta_4$			$L\beta_2$			$M\gamma_1$		
N_{VI}			$L\upsilon$					$M\beta_1$	$\mathbf{M\alpha_2}$
N_{VII}			$L\upsilon$						$\mathbf{M\alpha_1}$
O_I			$L\gamma_8$	$L\beta_7$					
O_{II}		$L\gamma_4$							
O_{III}	$K\delta_2$	$L\gamma_4$							
O_{IV}	$K\delta_1$		$L\gamma_6$	$L\beta_5$					
O_V				$L\beta_5$					

Table 1.2: Siegbahn notation assigned to different transitions [Wei04] (from the shell in a specific row to the shell in a specific column), the most important used transitions are in bold type;

The emitted characteristic X-rays are described by the Siegbahn notation [Sie31, Web29]. Table 1.2 shows the notation of allowed transitions between shells. The energies of these transitions can be approximated by Moseley's law:

$$E = C_1 \cdot (Z - C_2)^2 \tag{1.8}$$

where:

$E =$ Energy of the emission line

$Z =$ Atomic number

C_1 and C_2 Constants, depending on type of transition

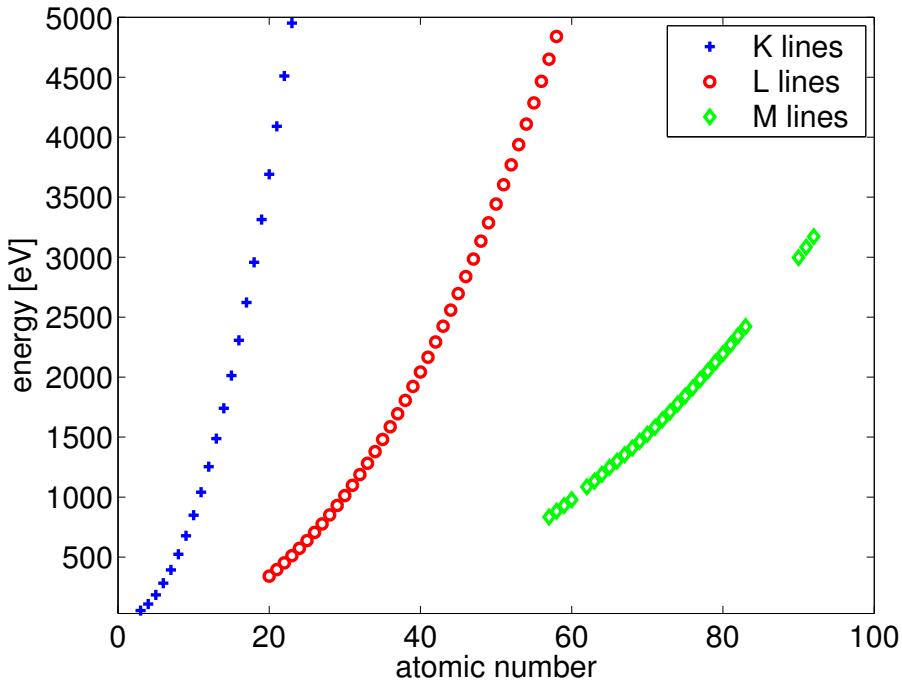

Figure 1.9: Energy of different X-ray emission lines as function of atomic number Z according to [Joh70]. Note: For the same energy several emission lines of different orders exist below 3 keV

The measured energies of various transitions (K, L, M) as function of the atomic number Z are plotted in fig. 1.9. This plot fits quite good to Moseley's law for according constants C_1 and C_2. This graph also shows that K, L and M transitions of elements with different atomic numbers exist in the energy range below 3 keV. These K, L and M lines are in several cases closely neighboring ($\Delta E < 50\,\mathrm{eV}$). The resolution of these lines leads to problems for Si(Li) detectors as shown in section 6.1.

The measured energies and relative intensities of all X-ray lines can be looked up in tables such as [Joh70]. Such a table enables the association of elements with detected X-ray lines and therefore the determination of the composition of a specimen.

In solids the energy levels spread out forming electron energy bands with finite energy width and with an internal structure of the density of states. This influence increases with increasing main quantum number n and is strongest for valence electrons. As the energy levels are broadened to energy bands the energy of the emitted X-rays is distributed around a mean transition energy. The width of this distribution is called natural line width of an X-ray line. Natural line widths have an order of magnitude of single electron volts. The chemical surroundings of an atom have an influence on the band structure which is also strongest for valence electrons. It influences the mean energy of an electron shell and also the shape of the density of states. This leads to changes in the shape and the mean energy of X-ray lines. Additionally it can influence the probability of X-ray transitions [Dod68]. It can be concluded that X-ray spectra contain information about the elements in the sample and also about the chemical surrounding of these elements. The information about chemical shifts has the ability to open a completely new field in EDS analysis.

1.4 X-Ray Detectors

Characteristic X-ray radiation is emitted by atoms in specimens in electron beam instruments such as scanning electron microscopes (SEM). This radiation can be detected by various kinds of spectrometers. According to their detection principle, they are divided into wavelength and energy dispersive spectrometers.

One important detector property is the energy resolution. This is the ability of the detector to resolve neighboring X-ray emission lines which can be characterized by the full width at half maximum (FWHM) of the detector response to X-rays with a specific energy. The FWHM is the energy range where the distribution of the measured X-ray intensity has more than half the value of the maximum. For a gaussian distribution the FHWM is correlated with the standard deviation σ by:

$$FWHM = 2.35 \cdot \sigma \tag{1.9}$$

Another important property is the detection efficiency ϵ, defined as the ratio of the number of detected to the number of incident X-rays. The detector efficiency is a function of X-ray energy.

1.4.1 Wavelength Dispersive Spectrometers

In wavelength dispersive spectroscopy (WDS), a crystal is used to select X-rays of a specific wavelength which are then detected with a proportional counter. The wavelength selection is done by Bragg diffraction in the crystal:

$$n \cdot \lambda = 2 \cdot d \cdot sin\theta \tag{1.10}$$

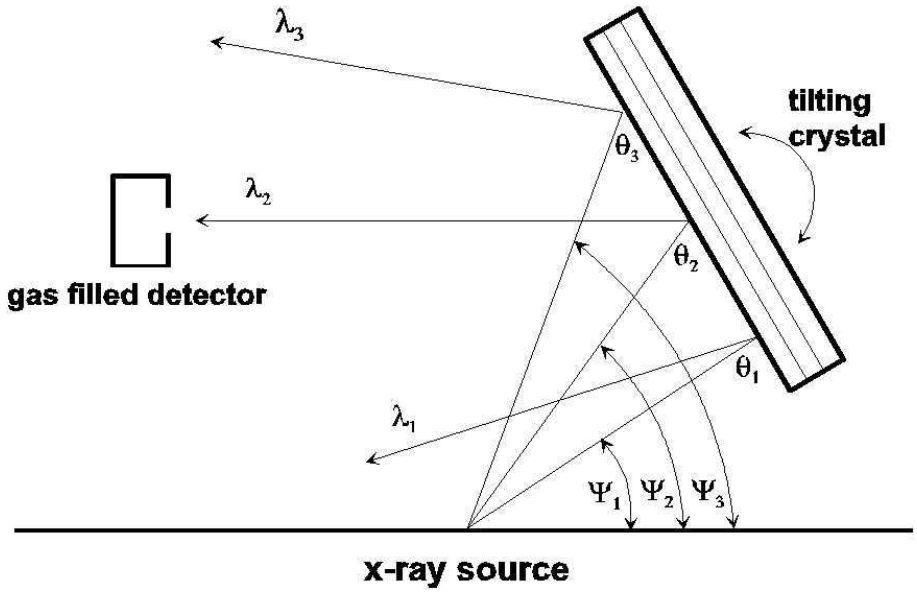

Figure 1.10: Schematic diagram of a WDS spectrometer [Wei04]

where

$n =$ An integer number, specifying the order of the diffracted beam

$\lambda =$ Wavelength

$d =$ The distance between lattice planes in a crystal

$\theta =$ Diffraction angle

The relation between energy and wavelength is given by:

$$E[keV] = 1.24/\lambda[nm] \tag{1.11}$$

To measure X-ray intensities of all possible energies it is necessary to cover a specific range of diffraction angles and to use crystals with different values for d. The quantum efficiency of WDS systems is usually about 30 % [Gol03]. This value can be explained with losses in the diffraction crystal, in the counter window material and in the counter tube. Because it is additionally only possible to detect X-rays with one specific wavelength at once, WDS measurements are time consuming, even if a high beam current is used.

The advantage of WDS systems is their very good energy resolution. A FWHM better than 10 eV is common for these systems, but also resolutions better than 1 eV have been achieved [Gra77].

1.4.2 Semiconducting Energy Dispersive Spectrometers

In an energy dispersive X-ray spectrometer, X-rays are absorbed in a detector that is able to determine the X-ray energy. Manifold X-ray energies are detectable at the same time because these detectors are, in contrast to WDS systems, operated without wavelength selection.

The most common detectors are semiconducting detectors such as lithium-drifted silicon detectors (Si(Li)) or high-purity germanium detectors (HPGe). The absorbing area of these detectors is typically $10\,\mathrm{mm}^2$ or $30\,\mathrm{mm}^2$. The absorbed X-rays generate electron-hole pairs that are separated by an electric field. After separation the total charge is measured. This charge is proportional to the X-ray energy as long as the recombination of electron-hole pairs can be neglected. For silicon the mean deposited energy per electron-hole pair is 3.76 eV [Fri03], for germanium this value is 2.96 eV. These energies are larger than the energy gaps of the semiconductors because a certain fraction of the deposited energy is converted into heat. The energy needed to create an electron-hole pair also determines the spectral resolution. This is the case because the resolution is mainly limited by statistical fluctuations and therefore depends on the number of created electron-hole pairs. The lower the energy per electron-hole pair is, the larger is the number of electron-hole pairs for a specific energy. The FWHM for semiconducting detectors can be calculated with [Fri03]:

$$FWHM_{intrinsic} = 2.35 \cdot \sqrt{F \cdot E \cdot \epsilon} \tag{1.12}$$

where:

$F =$ Statistical factor, called Fano factor (about 0.12)

$\epsilon =$ The energy required to produce an electron-hole pair in the crystal

$E =$ The energy of the X-ray in eV

In addition to intrinsic noise there are also other external contributions to FWHM such as amplifier noise and quality of the crystal but these effects are minor compared to the intrinsic FWHM of contemporary Si(Li) or germanium detector systems. For germanium detectors the intrinsic resolution is better than for Si(Li) detectors because the energy per electron-hole pair is lower. For Si(Li) detectors the FWHM is about 89 eV at the Si Kα emission line with 1739 eV.

The detection efficiency of EDS systems depends on the absorbing matter between specimen and active region of the detector. Fig. 1.11 shows the detection efficiency of a typical Si(Li) detector. One contribution to the efficiency is a vacuum window that is needed to protect the detector. Typically, on top of the detector crystal are absorbing layers, a contact layer and also a dead layer. The dead layer is a Si layer which generates no signal upon X-ray absorption. Another effect that contributes to efficiency is the fact that not all X-rays are absorbed in the Si crystal. But this effect is for typical Si(Li) detectors only relevant for energies larger than

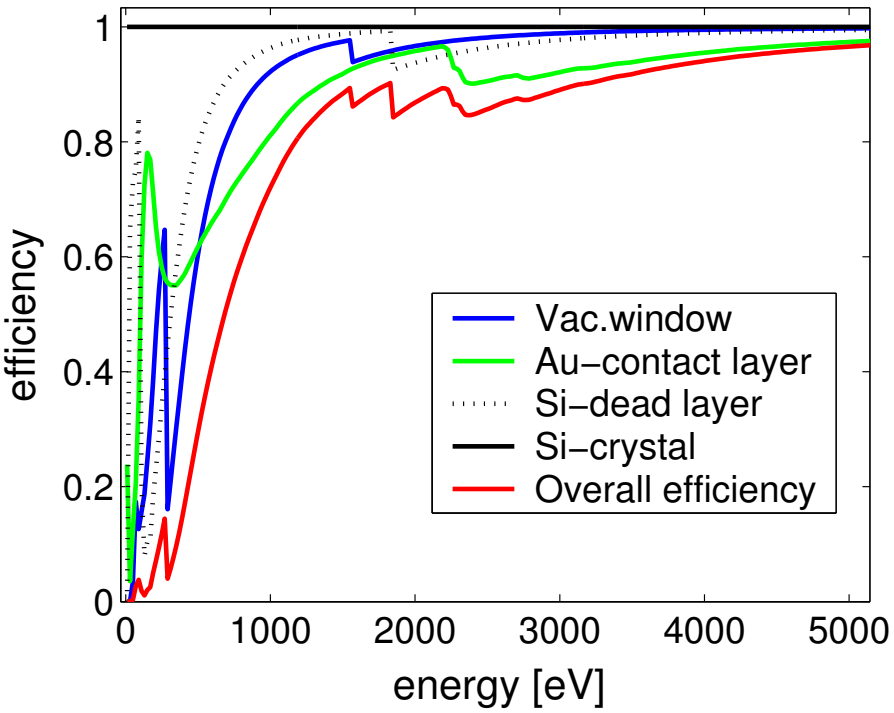

Figure 1.11: Detection efficiency of a typical Si(Li) detector with an ultrathin vacuum window (fabricated by Moxtek technologies) vs. X-ray energy

15 keV. Concluding, it can be stated that semiconducting EDS detectors are fast and easy to use whereas their spectral resolution is rather poor.

1.4.3 Low-Temperature Detectors

EDS with semiconducting detectors and WDS are complementary X-ray analysis methods with differing advantages and disadvantages. Other types of EDS detectors exist that overcome the disadvantages of semiconducting detectors. Promising candidates for future EDS detectors are low-temperature detectors such as superconducting tunnel junctions [Hub04, Rot04], magnetic calorimeters [Fle04], semiconducting thermistors [Ale99] and transition edge sensors (TES) which are described in this thesis. These detectors are superior to semiconducting detectors especially in terms of energy resolution. The FWHM is approximately the same as the FWHM of standard wavelength dispersive systems ($\sim 10\,\mathrm{eV}$ or better). This ability allows the resolution of closely neighboring lines in EDS analysis as shown in section 6.1. This is especially important for low-energy X-ray analysis (compare section 1.3).

Another advantage of the application of low-temperature detectors in EDS is the improved peak to background ratio. This value is defined as the ratio of the peak maximum to the background at the same energy. The sum of all X-ray events in the peak and also the background intensity only depend on sample and measurement conditions. Because the integral of the peak is constant, the intensity at the peak maximum in the spectrum is indirectly proportional to the FWHM. Therefore the peak to background ratio (PTBR) is indirectly proportional to the FWHM:

$$PTBR \propto \frac{1}{FWHM}$$

So a low FWHM leads to a high peak to background ratio and therefore a good detectability of characteristic X-ray radiation as illustrated in section 6.2. A low FWHM also enables the measurement of chemical shifts of emission lines (mentioned in section 1.3) as shown in section 6.3.

For low-energy X-ray analysis a good spectral resolution is needed to avoid peak overlaps. Additionally a good detection efficiency is necessary to enable analysis with low beam currents in acceptable measurement times. Low-temperature detectors combine the advantages of conventional WDS and EDS detectors. So they are the ideal choice for low-energy X-ray analysis enabling elemental analysis of small volumes.

1.5 Quantitative Information in X-Ray Spectra

In X-ray spectra, relative intensity ratios of characteristic X-ray lines are measured. But for some applications this qualitative information about the elements is not sufficient. The determination of the mass fractions in a sample with the help of

an X-ray spectrum is called electron probe quantitation. The detected intensity of a characteristic X-ray line as a function of the elemental mass fractions (C_A) can be calculated if the generated X-ray intensity, the absorption, the fluorescence and the properties of the detector are taken into account. This calculation, for a given element A and atomic shell l, leads to [Isa04, Ree93]:

$$\begin{aligned} I_A &= C_A \cdot \frac{\Omega}{4\pi} \cdot \epsilon_{det} \cdot \omega_A^l \cdot g_A^l \cdot (1+f) \cdot (1+g_{ck}) \cdot \frac{N_0}{A_A} \cdot Q_A^l(E_0) \cdot N_e \cdot \\ &\quad \cdot \int_0^{R_{max}} \Phi(\rho z) \cdot exp\left[-\chi_A \cdot (\rho z)\right] \cdot d(\rho z) \end{aligned} \tag{1.13}$$

The expressions in Eq. 1.13 are explained in table B.2. Eq. 1.13 can be used for electron probe quantitation[2] because it defines the relation between the mass fractions of different elements in the sample and the measured intensities of characteristic X-ray lines.

[2] see section 6.5

Chapter 2

Cooling System for the Operation of Low Temperature Detectors

For the operation of a low-temperature detector a cooling system is needed that cools down to the operating temperature of the detector and stabilizes this temperature for a sufficiently long measurement time. For the Polaris TES-EDS system this temperature is about 100 mK. The cooler has to be independent of liquid coolants for precooling because for the required application of the system in cleanroom environment liquid coolants are forbidden. Additionally, the operation of the cooler on a SEM requires a low-vibration cooling system which does not disturb the high-resolution SEM imaging. It is also advantageous if the whole system has a low weight because this simplifies the attachment of the system to the SEM. To meet these requirements for the Polaris TES-EDS system, a mechanical two-stage pulse tube cooler is used for precooling as shown in the upper part of fig. 2.1. An adiabatic demagnetization refrigerator (ADR) is attached to the second stage of the pulse tube cooler to cool down to the operating temperature of the detector. The ADR stage consists of a superconducting magnet and a paramagnetic salt pill consisting of ferric ammonium alum (FAA). A copped rod leads from the salt pill into the snout to cool the detector. The snout is needed to place the detector near to the intersection point of electron beam and specimen in the vacuum chamber of the SEM.

2.1 Pulse Tube Cooler

The Polaris TES-EDS system is cooled down to the starting temperature of the ADR stage by a two stage pulse tube refrigerator as described in [Wan98]. The pulse tube cooler requires a helium compressor (1 in fig. 2.2) which generates a high and a low pressure level. These pressure levels are successively connected to the pulse tube cooler by an external rotary valve (2 in fig. 2.2). This generates an oscillating pressure in the helium gas inside the pulse tube cooler. The frequency of the rotary valve is about 1 Hz. The reservoir (3 in fig. 2.2) causes a phase shift

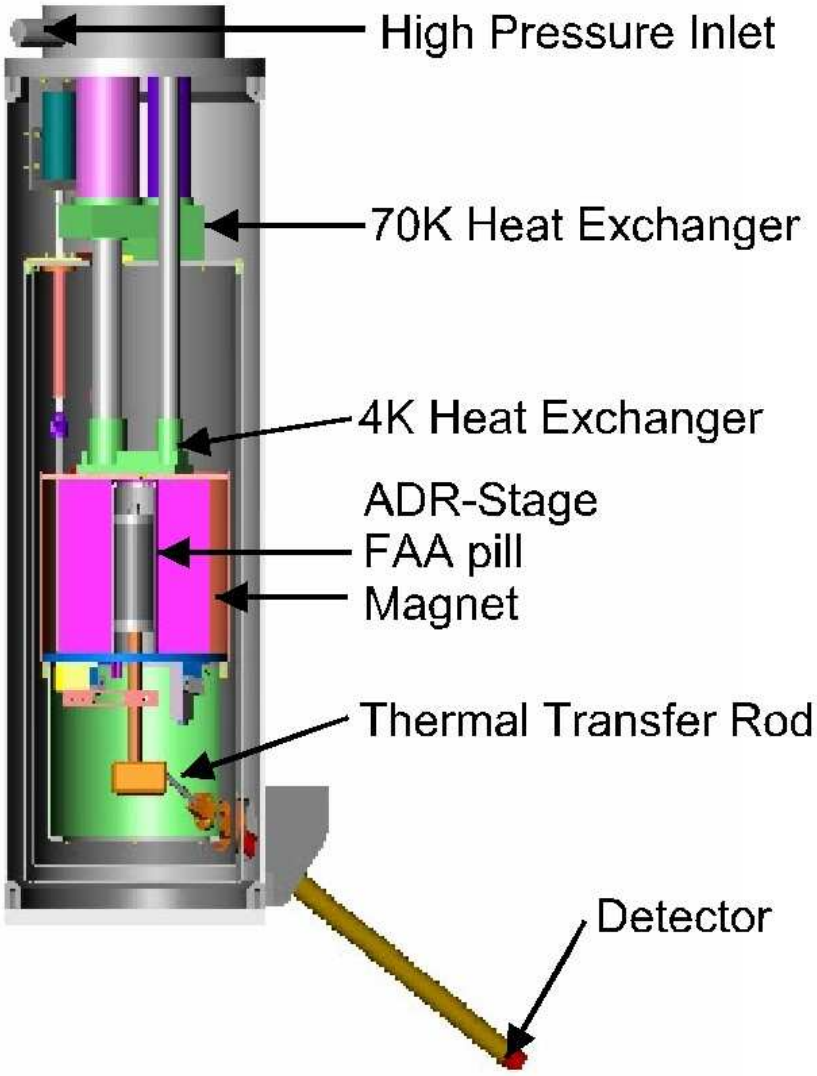

Figure 2.1: Cross section of the Polaris TES EDS system

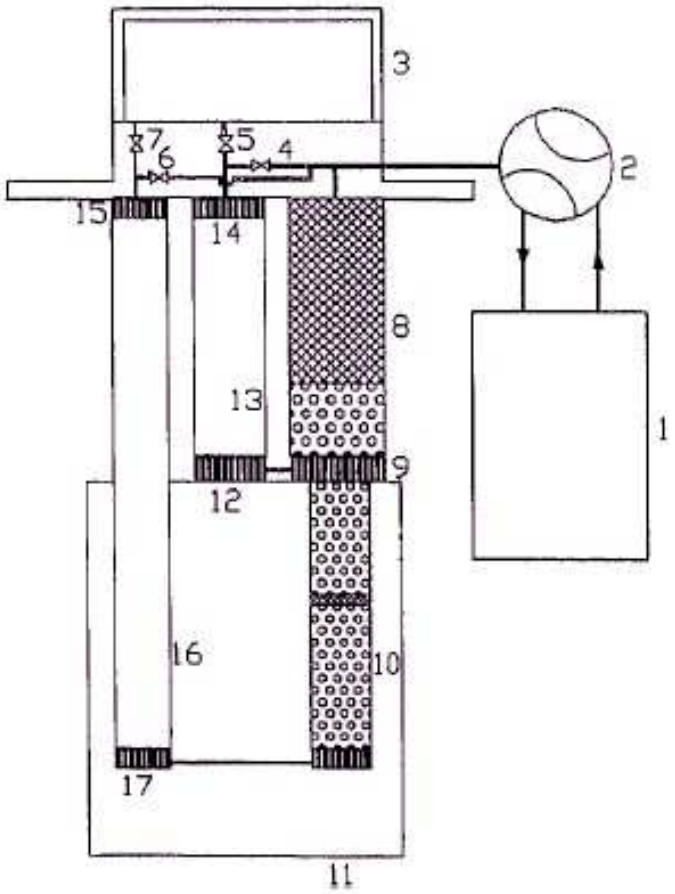

Figure 2.2: Schematic view of a two-stage pulse tube cooler[Wan98]; 1: compressor; 2: rotary valve; 3: reservoir; 4,6: double inlet valves; 5,7: orifice valves; 8: 1st stage regenerator; 9: flow straightener and heat exchanger; 10: 2nd stage regenerator; 11: radiation shield; 12: 1st stage cold head; 13: 1st stage pulse tube; 14,15: heat exchanger; 16: 2nd stage pulse tube; 17: 2nd stage cold head

between gas pressure and mass flow in the pulse tube. The phase shift leads to a cooling of the cold ends of the pulse tubes (12 and 17 in fig. 2.2). A detailed description of this process for a resembling pulse tube cooler setup can be found in [Yua99]. The design has two stages and a lowest base temperature of 2.4 K at the second stage cold end could be achieved [Wan98] with a cooling power of 500 mW at 4.2 K. The use of an external rotary valve enables the operation without moving parts in the cooler. Only the helium gas is moving in the cooler whereas the rotary valve is coupled to the cooler via a flexible tube. The separation of the rotary valve enables low-vibration operation.

Mechanical pulse tube coolers are operated without liquid gases such as nitrogen or helium. This enables cleanroom compatibility and easy operation of the cooler because it only needs electricity and cooling water for the compressor.

2.2 Adiabatic Demagnetization Refrigeration

As described in [Som77] adiabatic demagnetization refrigeration (ADR) requires a strong magnetic field and a paramagnetic material. The ADR cycle starts by applying a magnetic field to the paramagnetic material. The field aligns the magnetic moments parallel to the magnetic field and leads to a decrease of entropy. This is done at a constant temperature (T_1) as shown as arrow 1 in fig. 2.3. The temperature

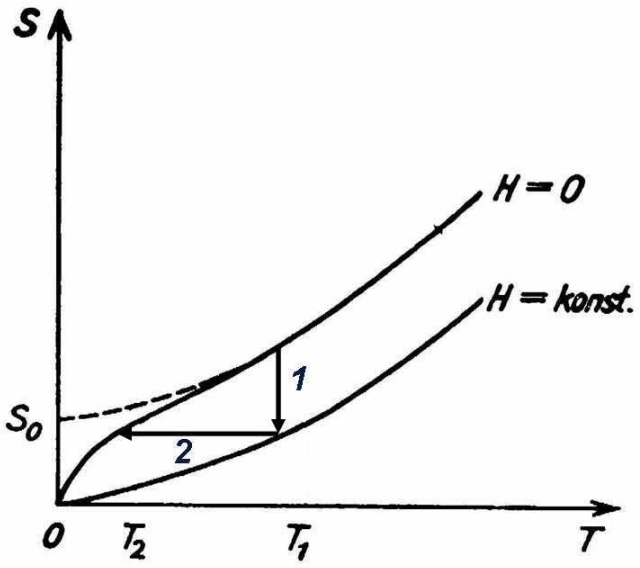

Figure 2.3: Entropy (S) of a paramagnetic salt in dependency of temperature (T) for different magnetic fields (H)[Som77]

is held constant by thermally coupling the paramagnetic material to a heat bath

(compare phase 1 in fig. 2.4). After decoupling the paramagnet from the heat bath, any changes of the temperature and other state variables, as long as they are slow, take place adiabatically, that is, without changes of the entropy. Upon demagnetizing the paramagnet the disorder of the magnetic moments increases, thereby decreasing the order in the rest of the system, which leads to a temperature decrease as shown in fig. 2.3. The temperature decreases from T_1 to T_2 at constant entropy (compare arrow 2 in fig. 2.3).

In the Polaris TES-EDS system the adiabatic demagnetization refrigerator (ADR) consists of a superconducting magnet and a paramagnetic salt pill consisting of ferric ammonium alum (FAA). The Fe atoms are separated in the lattice of the alum; they can not couple to a ferromagnetic state and the salt is therefore paramagnetic. The process of adiabatic demagnetization is shown in the temperature diagram of the salt pill in fig. 2.4. At the beginning of the recharge cycle a thermal contact (or

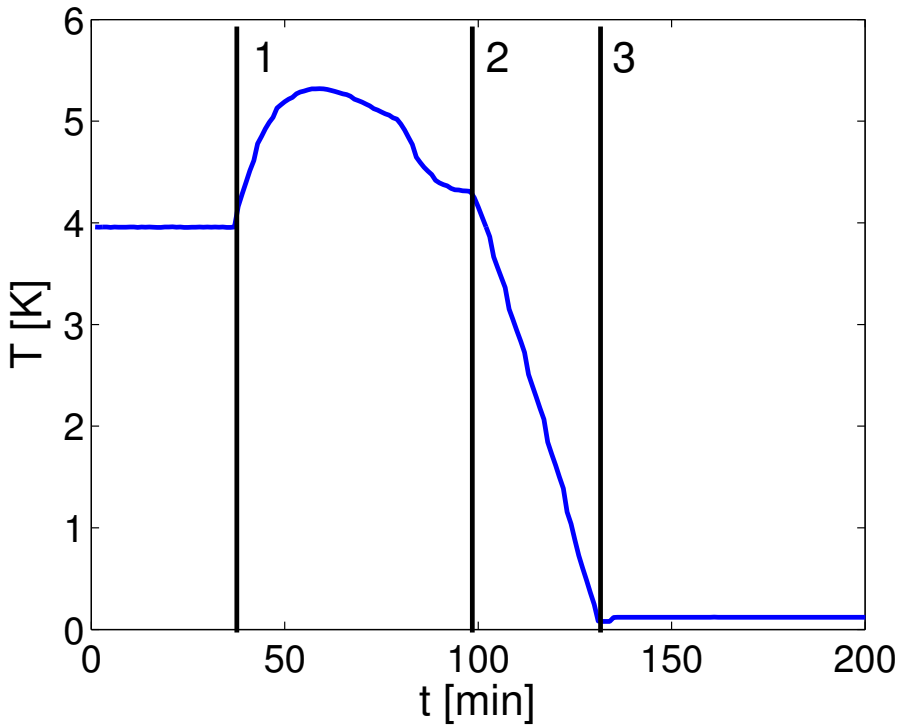

Figure 2.4: Temperature of ADR stage during recharge cycle. Different conditions are marked and described in the text

'heat switch') between the salt pill and 4K stage of the pulse tube cooler is closed and a magnetic field of 6 T is gradually applied to the salt pill. Due to the aligning of the magnetic moments in the field the pill warms up. The heat thus generated is transfered to the 4K stage of the pulse tube cooler (Phase 1). As soon as the salt pill has cooled to the bath temperature, the thermal link between pulse tube cooler and salt pill is opened and the pill is demagnetized adiabatically until the

working temperature of the detector is reached (Phase 2). The working temperature of the detector is stabilized by regulating the remaining magnetic field (Phase 3). The heat flow to the pill via infrared radiation and the remaining mechanical connection to the 4K stage leads to a steady decrease of the magnetic field. In the described setup, after about 8 hours the magnetic field is depleted and another adiabatic demagnetization cycling is necessary.

2.3 Automation of Cooler Functions

For the industrial user of the Polaris TES-EDS system it is important to control the system with a minimum of automated functions. These functions include the cooling down and warming up of the pulse tube cooler but above all the adiabatic demagnetization cycling and the regulation of the ADR. For these tasks a cooler control software was developed by VeriCold Technologies GmbH. After the recharge cycle the software stabilizes the working temperature of the detector. The temperature fluctuations are below 100 μK enabling a good operation of the TES detector.

Chapter 3

Operation of Transition Edge Sensors

Transition edge sensors (TES) have been developed as high-resolution particle and radiation detectors. TES are a special kind of calorimeters that can determine small temperature changes after X-ray absorption (see section 3.1). Such a temperature change causes a large resistance change in the superconducting to normal-conducting phase transition leading to a current change in a readout circuit (see section 3.3) that is measured with a SQUID amplifier (see section 3.2). The amplitude of the current change is approximately proportional to the X-ray energy and used to calculate an X-ray spectrum.

3.1 X-Ray Transition Edge Sensors

The detection principle of a low temperature microcalorimeter is the measurement of the heat ΔE deposited in an absorber with heat capacity C due to an absorbed X-ray . This heat leads to a temperature rise $\Delta T = \Delta E/C$ of the absorber that can be measured with a thermometer. After the energy deposition the detector returns

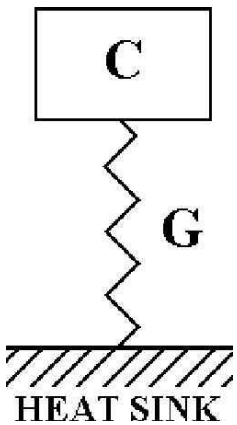

Figure 3.1: Simplified thermal model of TES detector

to equilibrium condition via a thermal link G (see Eq. 3.1) to a heat bath. A simple model of this process is shown in fig. 3.1. Fig. 3.2 shows a schematic view of the

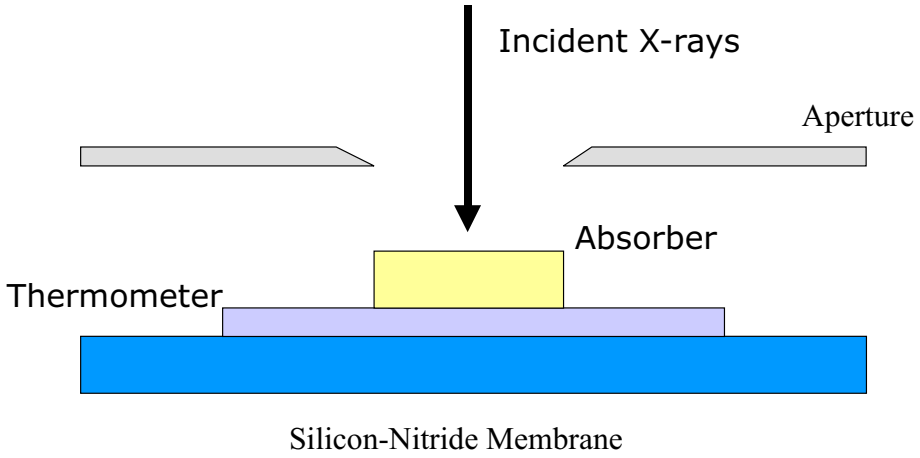

Figure 3.2: Schematic view of TES detector

TES detector. The detector consists of an aperture, an absorber with heat capacity C, a superconducting phase transition thermometer and a thermal link to a heat bath G realized with a Si_3N_4 membrane.

The aperture consists of a Pt-metal sheet with a laser-cutted hole in the middle that is slightly smaller than the absorber. It is needed to collimate X-rays on the absorber because X-rays that are absorbed in the thermometer or the membrane cause a different type of signal [Wol97] and therefore generate artifact peaks in the X-ray spectrum.

For the TES described in this thesis, gold is used as absorber material. Gold is a normal conducting metal with a large atomic number Z and therefore a relatively high mass absorption coefficient. The use of a normal conducting metal has the advantage that the absorbed heat thermalizes very fast (in the order of magnitude of ns [Irw98]) due to the presence of free electrons. The thermalization time is much faster than with other types of absorbers such as superconductors or isolators leading to a low signal rise time and therefore a large bandwidth of the signal. The disadvantage of metallic absorbers is a quite large heat capacity compared to other types of absorbers. The heat capacity C is dominated by the heat capacity of free electrons and is therefore proportional to the temperature T: $C = \gamma \cdot T$. Due to the large heat capacity the absorber has to be quite small to generate a detectable signal after X-ray absorption or, alternatively, the temperature has to be quite low. To combine the requirements of a low heat capacity, a large absorbing area, a high detection efficiency and also a simple and reliable setup of the cooler, most of the detectors used in the Polaris had an absorber size of $250\,\mu\text{m} \cdot 250\,\mu\text{m} \cdot 0.5\,\mu\text{m}$ and were operated at about 100 mK. The detection efficiency is the ratio of measured to incident X-rays. The detection efficiency ϵ of a $0.5\,\mu$m Au layer is shown in fig. 3.3.

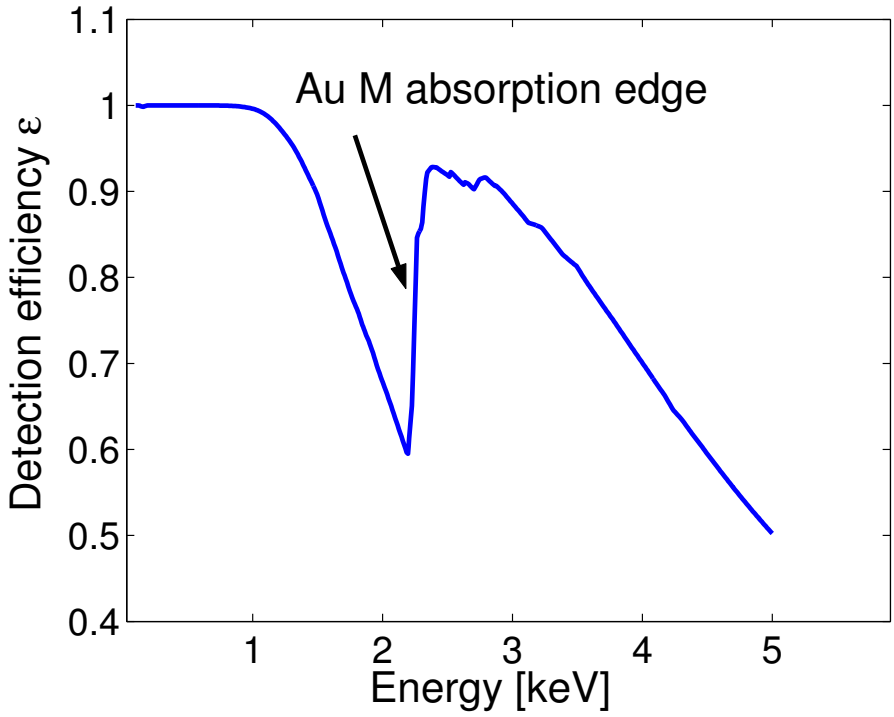

Figure 3.3: Detection efficiency ϵ of the detector absorber as function of X-ray energy

For a thin absorbing layer as used for the TES detectors in this work, there are still deviations from complete absorption, especially below the Au M absorption edge and at energies larger than 3 keV.

The thermometer is a superconductor biased in its narrow transition between the normal-conducting and the superconducting state. Fig. 3.4 shows the transition

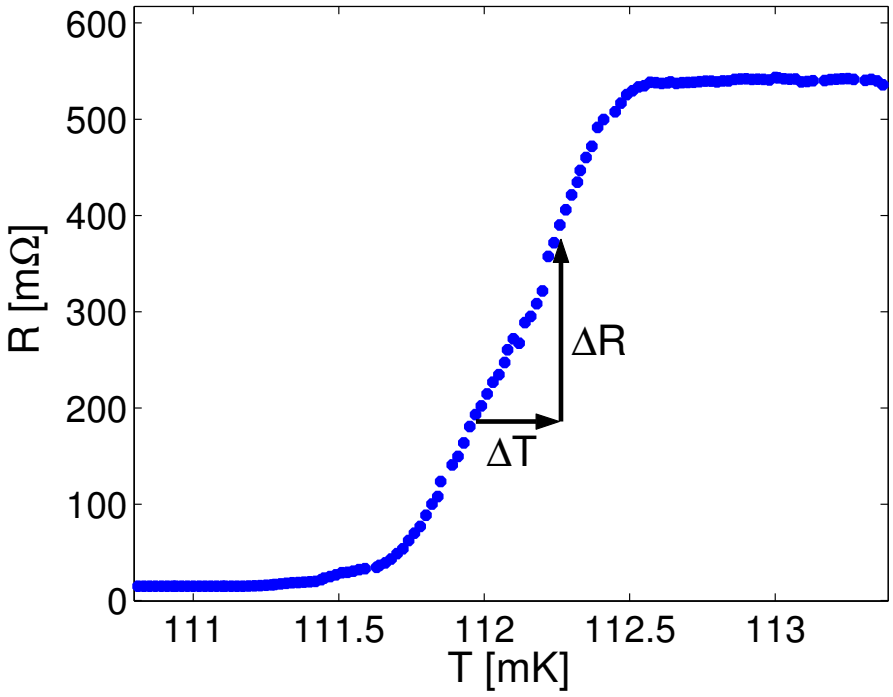

Figure 3.4: Phase transition of TES (Det. 1 of table B.1)

curve for detector 1 (see table B.1) that was used for most measurements in this thesis. The detector is stabilized within the phase transition and the resistance is therefore very sensitive to small temperature changes ΔT. The used superconductor is a proximity-effect superconductor [Höh98]. A thin superconducting layer is in contact with a thin normal conducting metal layer. The layer system behaves like a superconductor with a transition temperature that is adjustable between 0 mK and the transition temperature of the superconductor by changing the layer thicknesses. For det. 1 (see table B.1), the used materials are gold and iridium. Iridium is a superconductor with a transition temperature of 110 mK [Höh98] and Au is a normal conducting metal. As shown in fig. 3.4 the transition temperature of about 112 mK is even higher than for bulk Ir. The reason for this might be e.g. tensions in the Ir/Au film that influence the transition temperature.

After the temperature rise due to X-ray absorption the detector has to return to equilibrium conditions. This is achieved with a thermal coupling to a heat bath

which in case of an X-ray TES consists of a 300 nm thick Si_3N_4 membrane[1]. The use of such a membrane also helps to avoid losses of high-energy phonons that emerge in the beginning of the thermalization process. The heat loss via the membrane $\triangle P_{mem}$ is in first order approximation [Gal03]:

$$\Delta P_{mem} = G_{mem} \cdot \Delta T = -\frac{d\Delta U}{dt} = -C \cdot \frac{d\Delta T}{dt} \tag{3.1}$$

$$G_{mem} = G_0 \cdot T^{\beta} \tag{3.2}$$

G_0 and β are material constants of the detector. For a TES on a Si_3N_4 membrane, β has a value of about 3 [Irw95]. The temperature signal can be calculated by solving Eq. 3.1 as described in [Höh98]:

$$\Delta T = \Delta T_0 \cdot e^{-\frac{t}{\tau_0}} \tag{3.3}$$

$$\text{with } \tau_0 = \frac{C}{G_{mem}} \tag{3.4}$$

where τ_0 is the thermal decay time (about 1 ms) and ΔT_0 the signal amplitude. For Eq. 3.3 it is assumed that the whole detector is heated up instantly. After the instant thermalization the temperature decays exponentially due to losses via the thermal coupling.

3.2 SQUID Amplifier

The readout of the TES resistance is done with a SQUID[2] that works as low-impedance current amplifier [Ens00]. The SQUID consists of a superconducting loop that is separated by two Josephson junctions as shown in fig. 3.5. A constant bias current is applied to this device. Additionally a superconducting screening current is flowing in the SQUID that is periodical with a periodicity of one flux quantum $\Phi_0 = h/2e = 2.07 \cdot 10^{-15}\,\mathrm{Vs}$ [Ens00]. This current causes a voltage drop across the tunnel junctions as shown in fig. 3.5 (lower part) that is periodical, too. Thus, the voltage drop depends sensitively on the magnetic flux and can be used for measurements of the flux in the SQUID.

This device can be used as a linear current amplifier in the so called flux locked loop mode (FLL) [Dru01]. The FLL mode works with help of two coils. With a so called feedback coil a magnetic flux is applied to the SQUID in order to keep the SQUID voltage and therefore the flux in the SQUID constant. Thus, the current applied to the feedback coil is proportional to the external flux applied to the SQUID. The current that has to be measured is applied to a so called input coil. This coil changes the magnetic flux in the SQUID loop whereas the feedback coil compensates

[1] so far, electrothermal feedback (see sec 3.4) is neglected

[2] Superconducting QUantum Interference Device

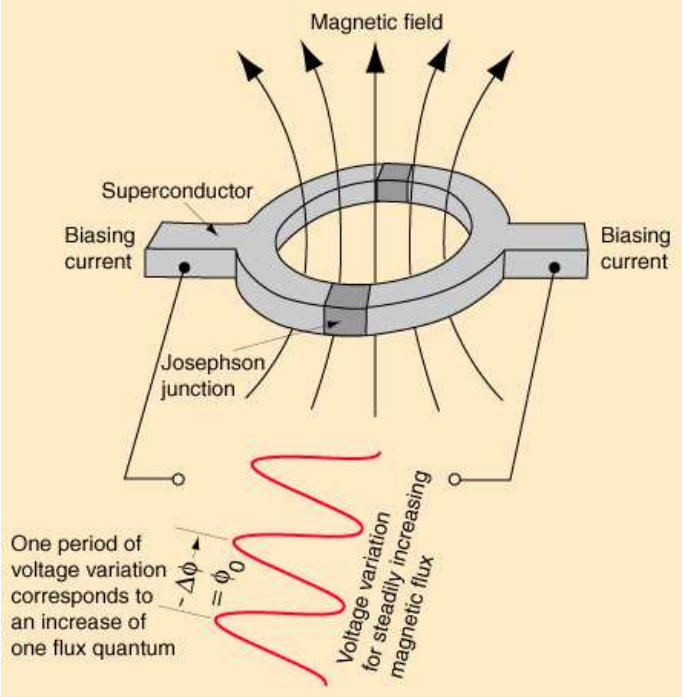

Figure 3.5: Schematic view of SQUID [Hyp]

this flux. So the current change in the feedback coil is proportional to the current change in the input coil. The signal applied to the feedback coil is the output signal of the SQUID that sensitively measures even very small current changes (see e.g. fig. 3.9) in the input coil. But the output signal is not proportional to the input current, because the SQUID can be operated at multiple flux values divided by Φ_0. Therefore only current changes in the input coil are proportional to signal changes whereas the offset can not be measured directly.

3.3 Readout of TES Resistance

The signal of a TES detector is a resistance change due to the temperature rise after the absorption of an X-ray. To measure this resistance change with a SQUID amplifier, the readout circuit shown in fig. 3.6 is used [Höh98]. A constant bias current is divided in a current flowing through a constant shunt resistor R_S and a current I_{det} through the detector. The current through the detector is determined by:

$$R_S \cdot I_{Bias} = L\dot{I}_{det} + I_{det} \cdot (R_{det} + R_S) \tag{3.5}$$

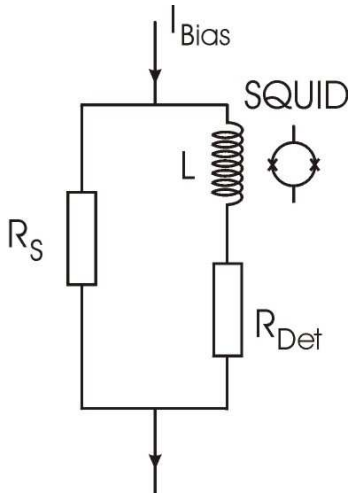

Figure 3.6: Readout circuit of the TES resistance, including a SQUID amplifier

The variables in Eq. 3.5 are described in fig. 3.6. In a quasi-stationary situation ($L\dot{I}_{det} \ll I_{det} \cdot (R_{det} + R_S)$), I_{det} is a function of R_{det}:

$$I_{det} = \frac{I_{Bias}}{1 + \frac{R_{det}}{R_S}} \tag{3.6}$$

The described readout circuit is used for nearly all TES detectors. The signal is the current change in the SQUID amplifier. For a given resistance change and working point[3] of the detector, it can be maximized by the optimization of the shunt resistance [Hol01]. The signal amplitude is determined by the derivation of the detector current (Eq. 3.6) with respect to the detector resistance (with a constant bias current):

$$\frac{dI_{det}}{dR_{det}} = -\frac{I_{Bias}}{(1 + \frac{R_{det}}{R_S})^2} \cdot \frac{1}{R_S} \tag{3.7}$$

The detector is heated up by the detector current I_{det} due to its resistance R_{det}. So the detector behavior is mainly determined by the temperature and the detector current. For the choice of I_{Bias} on the other hand there are no restrictions. So, with

$$I_{Bias} = I_{det} \cdot (1 + \frac{R_{det}}{R_S}) \tag{3.8}$$

Eq. 3.7 is:

$$\frac{dI_{det}}{dR_{det}} = -\frac{I_{det}}{(1 + \frac{R_{det}}{R_S})} \cdot \frac{1}{R_S} = -\frac{I_{det}}{R_{det}} \cdot \frac{1}{(1 + \frac{R_S}{R_{Det}})} \tag{3.9}$$

This means that the signal amplitude is optimum for a shunt resistance that is very low compared to the detector resistance. With such a shunt resistance the detector

[3]The working point is detemined by the bias current and the bath temperature

is voltage biased meaning that the voltage applied to the detector is independent of the detector resistance. A low shunt resistor is also necessary for the application of negative electrothermal feedback (see section 3.4). In the Polaris setup a bias resistance of 8 mΩ is used.

Due to the inductance L of the SQUID input coil L_{SQUID} and the wires L_{wires} in the readout circuit in series with the resistances of the detector R_{det} and the shunt R_S, the readout circuit forms a low pass filter (compare Eq. 3.5). The time dependant behavior of the detector current is determined by the solution of Eq. 3.5:

$$I_{det} = I_0 + e^{-\frac{R_{det}+R_S}{L}\cdot t} = I_0 + A \cdot e^{-\frac{t}{\tau_r}} \tag{3.10}$$

Thus, the low pass filter limits the rise time of an electrical signal to [Höh98]:

$$\tau_r = \frac{L_{SQUID} + L_{wires}}{R_{det} + R_S} \tag{3.11}$$

The response time of the TES to an X-ray is in the order of magnitude of ns [Irw98]. Therefore, the response time in the described setup is much faster than the electrical rise time and the measured rise time of the detector can be approximated with the electrical rise time of about 3 μs (see fig. 3.9).

3.4 Electrothermal Feedback

The change of the detector resistance is measured in a readout circuit as described in section 3.3. The shunt resistance R_S (compare fig. 3.6) is typically chosen to be much smaller than the detector resistance R_{det} at the used working point of the detector. Thus -to good approximation- the detector is voltage biased. This means that the voltage V at the detector is given by $R_S \cdot I_{Bias}$ and is almost independent of the resistance R_{det} when a constant bias current I_{Bias} is flowing through the readout circuit. The (very small) current through R_{det} leads to a heating of the detector. Thus the TES temperature is slightly higher than the bath temperature of the cryostat due to the heating power that is dissipated in the TES. The amount of the heating power depends on R_{det} and leads to a stabilization of an equilibrium resistance in the TES transition: the heating power of approximately V^2/R_{det} increases when the temperature drops because the resistance R_{det} decreases with temperature (see Fig. 3.4); on the other hand, V^2/R_{det} decreases with rising temperature. Thus, resistance and temperature are kept in equilibrium. This effect is called negative electrothermal feedback (ETF) [Sei90, Irw95]. If additional power is deposited in the detector, the temperature rises and therefore the ETF heating power is reduced. The reduction of ETF heating power ΔP_{etf} is proportional to the temperature change ΔT [Gal03]

$$\Delta P_{etf} = G_{etf} \cdot \Delta T \tag{3.12}$$

$$where\, G_{etf} = \frac{P_{el}}{T} \cdot \frac{R_{det} - R_S}{R_S + R_{det}} \cdot \alpha \tag{3.13}$$

$$with\, \alpha = \frac{T}{R_{det}} \cdot \frac{dR_{det}}{dT} \tag{3.14}$$

P_{el} is the total electric power dissipated in R_{det}. G_{etf} is the coupling constant to the heat bath via ETF and α is the transition steepness. ETF is one way in which the TES can relax to equilibrium after absorption of an X-ray of energy E_{X-ray}. The other way is the thermal coupling of the TES to the heat bath, for example in the case of X-ray TES via a Si_3N_4 membrane, Eq. 3.1. G_{mem} and G_{etf} are the two couplings to the heat bath and described in [Gal03]. Taking ETF into account, Eq. 3.1 changes to:

$$\Delta P = (G_{mem} + G_{etf}) \cdot \Delta T = -\frac{d\Delta U}{dt} = -C \cdot \frac{d\Delta T}{dt} \tag{3.15}$$

So the effective decay time, (with ETF taken into account) is (compare Eq. 3.3):

$$\tau_{eff} = \frac{C}{G_{mem} + G_{etf}} \tag{3.16}$$

In linear approximation ($\Delta I \propto \Delta T$ for big values of t), the response of the detector S(t) to an X-ray absorption at time t_0 can be described by [Höh98, Prö95]:

$$S(t) = I_0 + \Theta(t - t_0) \cdot A \cdot (-exp^{-\frac{t-t_0}{\tau_r}} + exp^{-\frac{t-t_0}{\tau_{eff}}}) \tag{3.17}$$

where:

$I_0 =$ Equilibrium current through the detector (see Eq. 3.10)

$\Theta(x) =$ Heaviside step function ($= 1\, for\, x > 0, = 0\, for\, x > 0$)

$A =$ Amplitude of detector response

$t_0 =$ Start time of X-ray absorption

$\tau_r =$ Rise time (Eq. 3.11) of detector response

$\tau_{eff} =$ Effective decay time (Eq. 3.16)

The heating due to the bias current I_{Bias} affects the detector behavior and leads to effects such as ETF. This influence can be measured by slowly ramping the bias current while recording the detector current for all temperatures accessible to the ADR. The changes in bias current have to be slower than the decay time of the thermometer to allow a measurement of the detector current in a quasi equilibrium situation, so the ramp time is chosen to be 1 s. Such a measurement, done for a temperature range between 60 mK and 110 mK, takes about 20 minutes. A set of

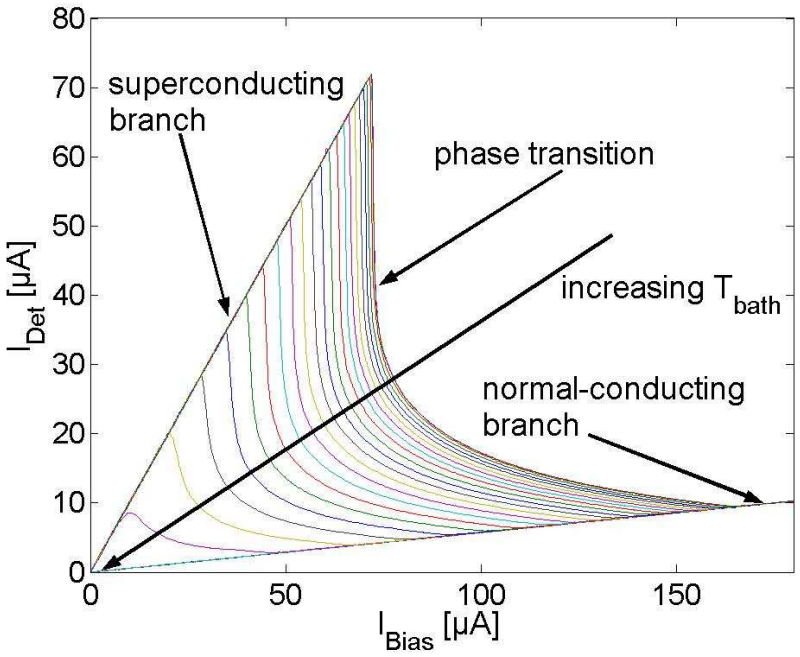

Figure 3.7: Detector current as function of bias current for different temperatures

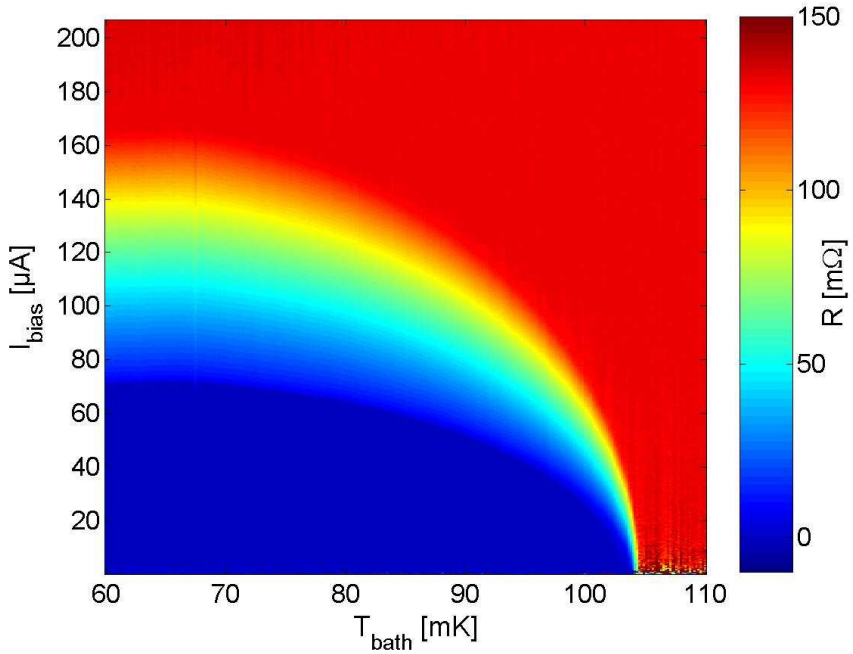

Figure 3.8: Detector resistance R_{det} as function of temperature T and bias current I_{Bias}

the measured curves is shown in fig. 3.7. With these curves, detector parameters as the resistance (see fig. 3.8) or the detector current at a given working point can be determined. Also an optimized working point can be found by the help of this measurement.

The advantage of the use of ETF for TES detectors is the shortening of the decay time of the X-ray pulse, a self regulation of the detector temperature [Irw98] and also a lower noise of the detector [Gal03]. Thus, ETF improves the detector properties.

3.5 TES Signal Processing

The signal of the TES readout circuit amplified by a SQUID is triggered and recorded with a transient recorder[4]. An example for a recorded TES response to a Si Kα X-ray, a so called pulse, is given in fig. 3.9. In the first part of the detector response the

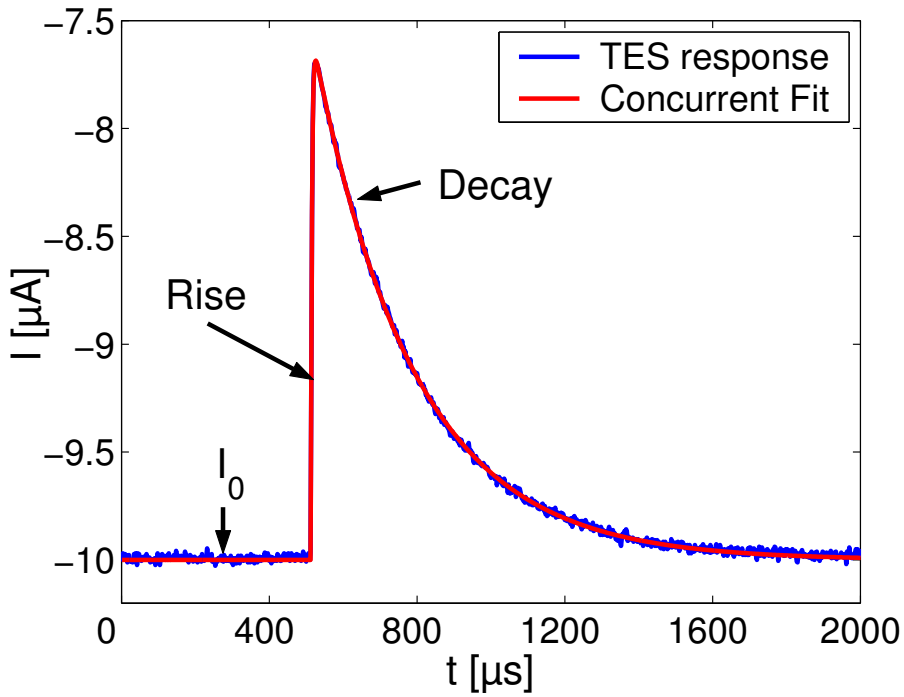

Figure 3.9: Recorded detector response to Si − Kα X-ray (1739 eV) and concurrent fit (done with Eq. 3.17); measurement conditions: bath temperature 55 mK, bias current 100 μA, Det. 1 of table B.1;

equilibrium signal is measured. If the offset of the SQUID output is known (compare section 3.2), the equilibrium current I_0 can be calculated with this value. Then, after

[4]National Instruments NI-DAQ 6065E

X-ray absorption the temperature rises steeply together with the detector resistance. So the current decreases as shown in fig. 3.9 marked as 'rise' of the detector response. After the thermalization of the heat in the TES the temperature returns together with the measured current to equilibrium condition (decay).

The measured signal I(t) is a combination of the detector response to the absorbed X-ray S(t) (Eq. 3.17), the thermodynamical noise N(t) and disturbance D(t):

$$I(t) = S(t) + N(t) + D(t)$$

A least-square fit of Eq. 3.17 applied to the detector response in fig. 3.9 is in good accordance with the measured detector response (blue line in fig. 3.9).

Noise arises from thermodynamical processes in the detector, the readout circuit and the amplifier system such as Johnson noise of shunt and detector resistance, phonon noise due to a finite thermal coupling G_{mem} and SQUID noise. The noise of low temperature detectors including TES is described and calculated in [Gal03]. Disturbances are influences of the environment of the detector system on the measured signal such as electromagnetical disturbance from AC power lines or microphonic pickup caused by vibrations. Fig. 3.10 shows a spectrum of the noise power

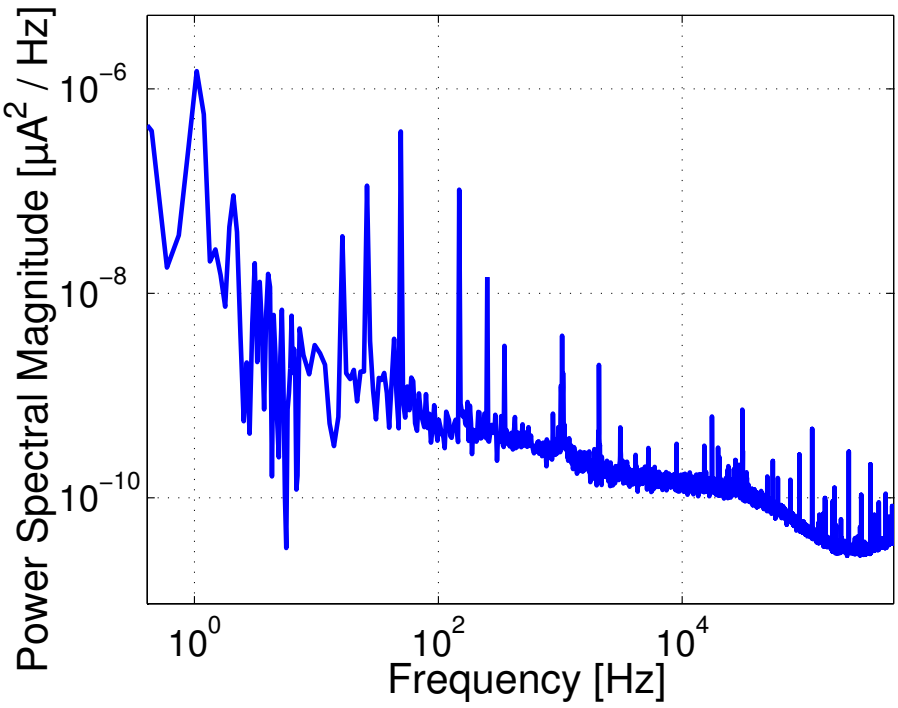

Figure 3.10: Noise power spectrum of TES detector, measured under conditions similar to conditions in fig. 3.9;

amplitude, measured in the Polaris EDS system. The noise spectrum is measured as follows. With the transient recorder 10 s of the detector signal are sampled

with a sample frequency of 1.25 MHz. With this recorded signal a power spectrum with 0.1 Hz resolution is calculated[5]. At higher frequencies a mean power spectral magnitude of a larger energy range $\Delta f \propto \sqrt{f}$ is calculated to suppress statistical fluctuations of the noise spectrum. The peaks in the spectrum in fig. 3.10 show disturbances as changes of bath temperature caused by the pulse tube cooler at approximately 1 Hz. Also peaks at 50 Hz and its multiples are observable. They are caused by electromagnetic influences of AC power lines. Small peaks at about 1 kHz are caused by vibrations of readout circuit leads in adjacent magnetic fields. The vibrations are excited by the pulse tube cooler (compare section 5.2). The decrease of the noise power at about 50 kHz is caused by the combination of the SQUID input coil and the whole resistance in the readout circuit, see section 3.3. This combination filters the signal with a cut-off frequency $f = 1/2\pi\tau_r = R/2\pi L$.

In first order approximation the amplitude A is proportional to the energy of the absorbed X-ray. So the amplitude of each detected X-ray event has to be determined with the least possible error to obtain a spectrum. The error in the determination of the amplitude is mainly caused by the noise on the detector signal. But also small changes of the detector responsitivity contribute to the error. For example the shape of the detector response changes slightly due to changes of the equilibrium temperature of the detector because of the non-linearities in the superconducting to normal-conducting phase transition of the detector (see fig. 3.4). To minimize these errors an appropriate filter has to be applied to the recorded detector signal. In the case of stationary noise and a constant signal shape the best filter is the so called Wiener filter [Wie50]. But the noise of the TES is a function of the temperature and therefore changes during the X-ray event. Additionally the signal shape varies with X-ray energy and also with the equilibrium temperature. So the presumptions for the Wiener filter delivering the optimum energy resolution are not completely fulfilled. For the Polaris signal processing, a digital emulation of a chebyshev band pass filter [Par87] is used. Such a filter enables a spectral resolution comparable to an optimum filter. Additionally this filter is much faster in computation because no fast fourier transformation is necessary. This enables real time processing of Polaris-EDS spectra. After filtering the signal, its amplitude is calculated by the determination of the maximum of the filtered signal. In first order approximation the amplitude of the filtered signal is proportional to X-ray energy. But to obtain accurate X-ray energies in the spectrum, a non-linear calibration has to be performed as described in chapter 4.

In conventional EDS spectrum analysis the spectrum is divided in so called bins. These are small energy regions covering the whole energy range. The number of X-ray events as function of the mean energy of the concurrent bins forms the spectrum. With changing the bin width W_{bin} the spectrum can be smoothed because the statistical fluctuation σ per number of events in each bin is a function of the bin

[5]with Matlab function PSD

width W_{bin}:

$$\frac{\sigma}{N} = \frac{1}{\sqrt{N}} \propto \frac{1}{\sqrt{W_{bin}}}$$

So a large bin width leads to low relative statistical fluctuations. But if the bin width is too large, the peak FWHM increases because the bin width contributes as additional error to the detector FWHM. Also an accurate determination of the peak energy becomes difficult because each X-ray energy is assigned to the mean energy of an energy region leading to an error in energy determination of a peak. TES spectra need a low bin width due to the good FWHM. As the total number of counts can also be quite low, the statistical fluctuations can become too large to detect smaller peaks. So for Polaris spectra the so called gaussian binning is used.

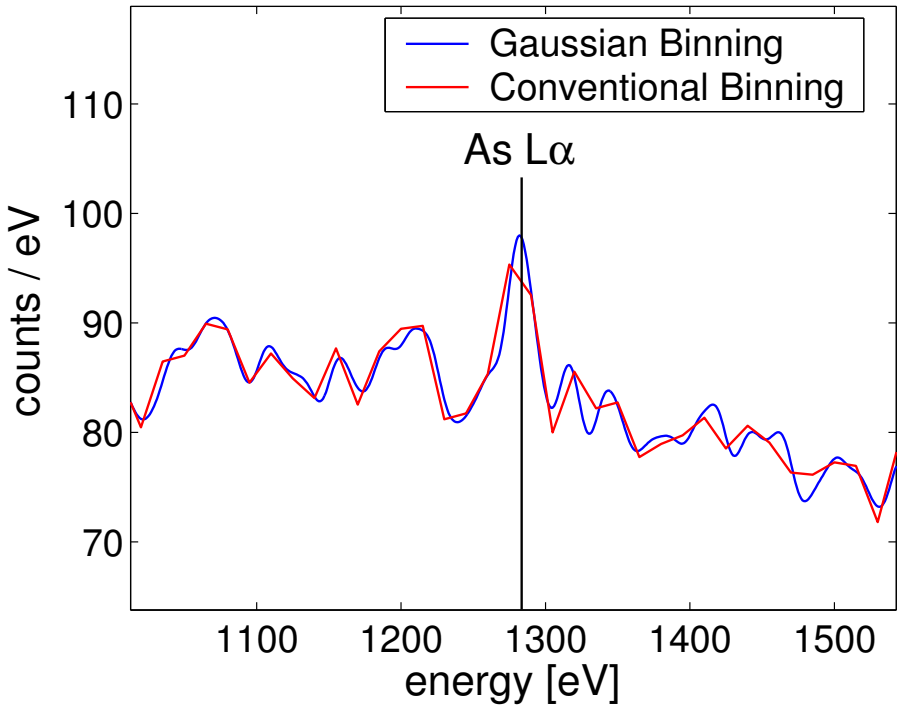

Figure 3.11: Spectrum of As-doped Si (compare section 6.2), with two different kinds of binning (both with 15 eV), black line marks $As - L\alpha$ line; both spectral intensities are normed to be equivalent to an 1 eV binning

In this method, for each event a gaussian distribution function around its energy is calculated. The sum of all these gaussians then forms the Polaris spectrum. The width of the gaussian is variable but the integral of each gaussian function is normalized. So integration over the energy axis of the spectrum results in the total number of X-ray events. Due to the variable width, the spectrum can be smoothed to suppress statistical fluctuations. Thus, also small peaks are clearly recognizable. Additionally, the mean X-ray energy of a peak is preserved. Fig. 3.11 shows a

comparison of the two methods, both binned with 15 eV. The measured specimen is Si doped with As (see section 6.2). The intensity of the As peak is quite low so the determination of the peak in the continuum radiation is difficult. The peak to background ratio of the spectrum with gaussian binning is better and also the energy is better determined (compare with the black line in fig. 3.11). All spectra in this thesis are binned with the gaussian binning method.

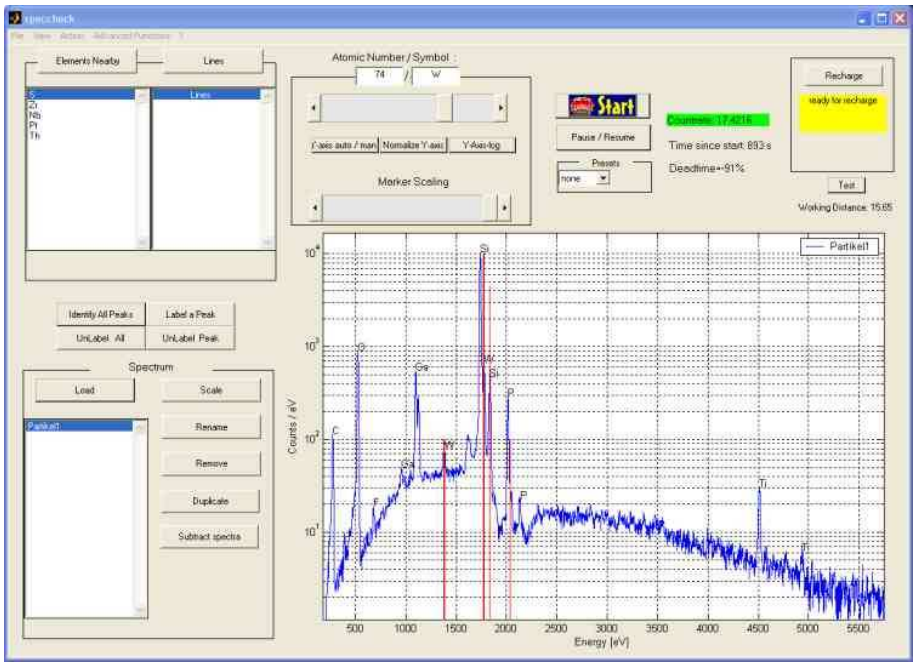

Figure 3.12: EDS graphical user interface 'SpecCheck'

The energy calibrated (compare chapter 4) binned spectrum is plotted in an EDS graphical user interface, called SpecCheck, that enables further analysis of the spectra such as automated peak identification, linescan/mapping (see section 6.4) or quantitation (see section 6.5). With the achieved degree of automation in spectral analysis the TES-EDS system Polaris can be fully integrated in the environment of a failure analysis lab.

3.6 Artifacts in TES Spectra

Background in TES EDS spectra is mainly caused by bremsstrahlung as described in section 1.2. But also detector artifacts contribute to the spectrum. Artifacts that are observable in the Polaris EDS spectra are pileup peaks and escape peaks.

Pileup peaks are peaks that are caused by simultaneous absorption of two X-rays. This means in case of TES detectors that the time difference between the absorption of the two X-rays is lower than the error of the rise time determination of a single

X-ray. The probability to absorb a second X-ray within the rise time error depends on the number of absorbed X-rays (input count rate) and the rise time error. The energy of the pileup peak is the sum of the energies of the two X-rays. Fig. 3.13

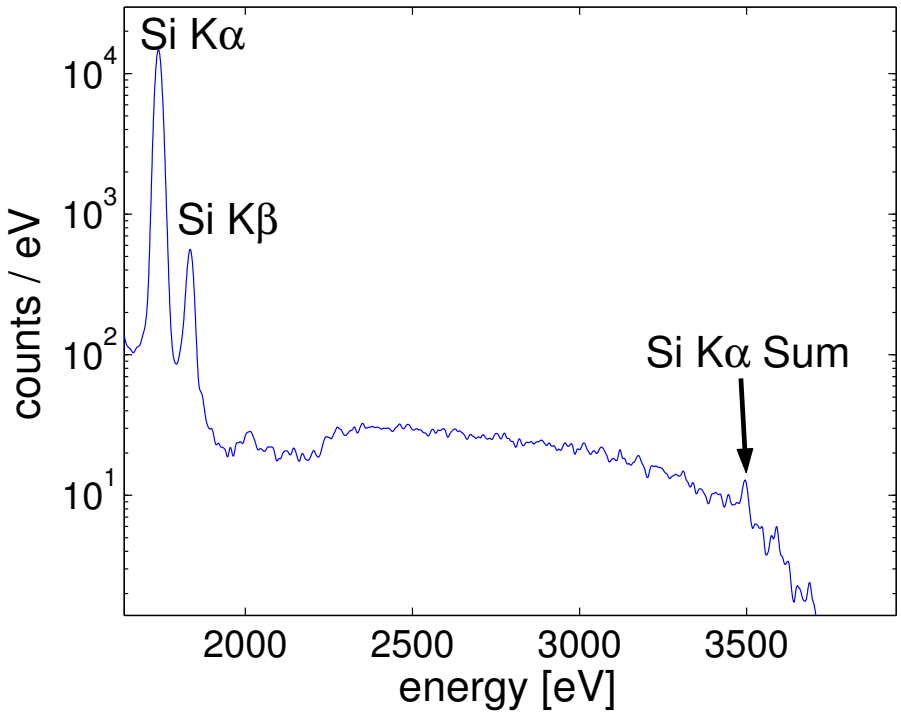

Figure 3.13: Spectrum of Si with a input count rate of 340 cps; beam energy is 5 keV

shows a spectrum of Si with an observable sum peak. The measured ratio of the Si Kα pileup peak to the Si Kα peak is $3.1(0.4) \cdot 10^{-4}$. So, although the input count rate is quite high (340 cps), the intensity of the sum peak is still low.

The absorber of the TES used for the Polaris consists of gold. If an absorbed X-ray has an energy larger than an Au M absorption edge, it is possible that the M shell of the Au atom is ionized. This can cause a fluorescent Au M X-ray. If this X-ray escapes the absorber, only the difference between the primary X-ray energy and the fluorescent X-ray is detected. The peaks that are caused by this process are called escape peaks. For excitation of a fluorescent Au Mα X-ray the M_V shell[6] with 2005 eV [Bea67] has to be ionized whereas for the emission of an Au Mβ X-ray the M_{IV} shell with 2291 eV [Bea67] has to be ionized. Fig. 3.14 shows a spectrum of NaCl that is sputter coated with Pt/Pd. The Cl Kα has an energy of 2621 eV and is very intensive in this spectrum. Thus, it excites escape peaks at $2621\,\text{eV} - 2121\,\text{eV} = 500\,\text{eV}$ for the Au Mα escape line and $2621\,\text{eV} - 2205\,\text{eV} = 416\,\text{eV}$ for the Au Mβ escape line that can be observed in the spectrum. In most spectra no sufficiently intensive

[6] compare section 1.3

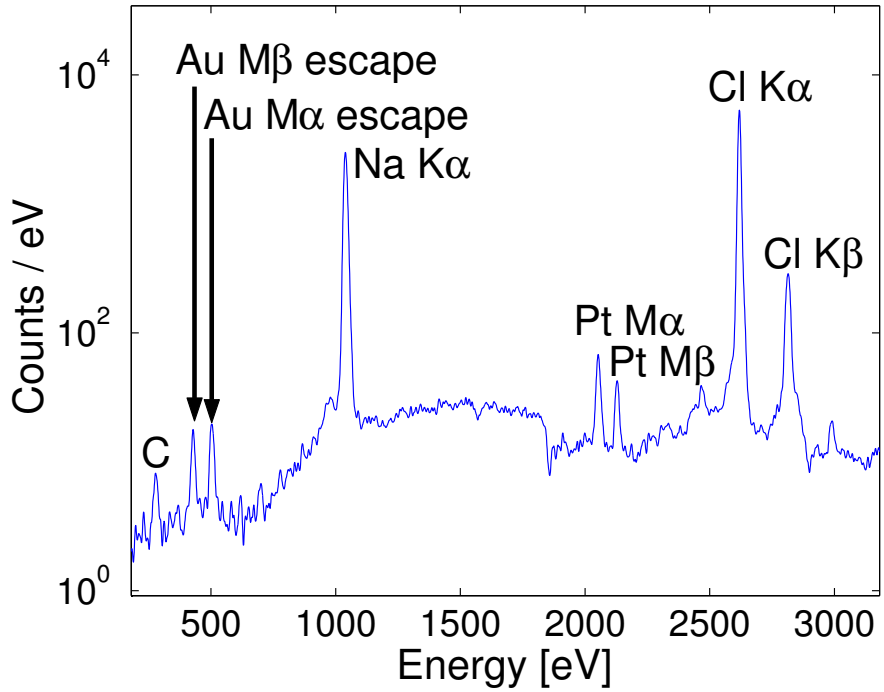

Figure 3.14: Spectrum with Au escape peaks caused by the Cl Kα line at 2621 eV

X-ray line with an energy larger than the energy of the absorption edges is present, so the observation of escape peaks only occurs in very few of the measured spectra.

Chapter 4

Linearization of the Pulse Height Spectrum

Transition Edge Sensors (TES) offer an excellent energy resolution. But the energy calibration of a TES-based spectrometer is problematic due to the non-linear behavior of the detector response. So a reliable calibration method is needed for everyday operation of TES-based spectrometers. The most promising method is the calculation of the energy dependence by the help of the detector signal. Operated in electrothermal feedback mode the pulse shape of the detector signal contains information about the energy of the X-ray event as shown in sec. 4.2. Using this information a calibration accuracy of a few eV in a range up to 6 keV is possible. Examples measured with several detectors demonstrate the quality of this method for everyday use of TES-EDS detectors in material analysis. For the measurements according linearity, the detectors of table B.1 were used.

4.1 Non-Linearity of TES Detectors

The measured signal of TES detectors is mainly determined by the resistance change of the TES due to a temperature rise caused by the absorption of an X-ray. The change of the resistance R as function of the temperature T is determined by the superconducting phase transition (see fig. 3.4). Because of its non-linear T dependence this phase transition leads to a non-linear detector response. In Fig. 4.1, the deviation $\Delta E = E_m - E_{tab}$ between measured peak position (E_m) and tabulated energy (E_{tab}) is plotted as a function of energy. The x-axis has been scaled to correctly reproduce the $Si\,K\alpha$ energy at 1739 eV. At higher energies the deviations increase to nearly 10% of the tabulated X-ray energy. This is much larger than the difference between X-ray lines to be distinguished, making any peak identification almost impossible. To solve this problem, usually a calibration function $E_{cal}(A)$ has to be found by using a multi element energy standard covering the whole energy spectrum of interest. The X-ray energy E is then determined from the detector response A by applying $E_{cal}(A)$. Unfortunately, in case of superconducting TES,

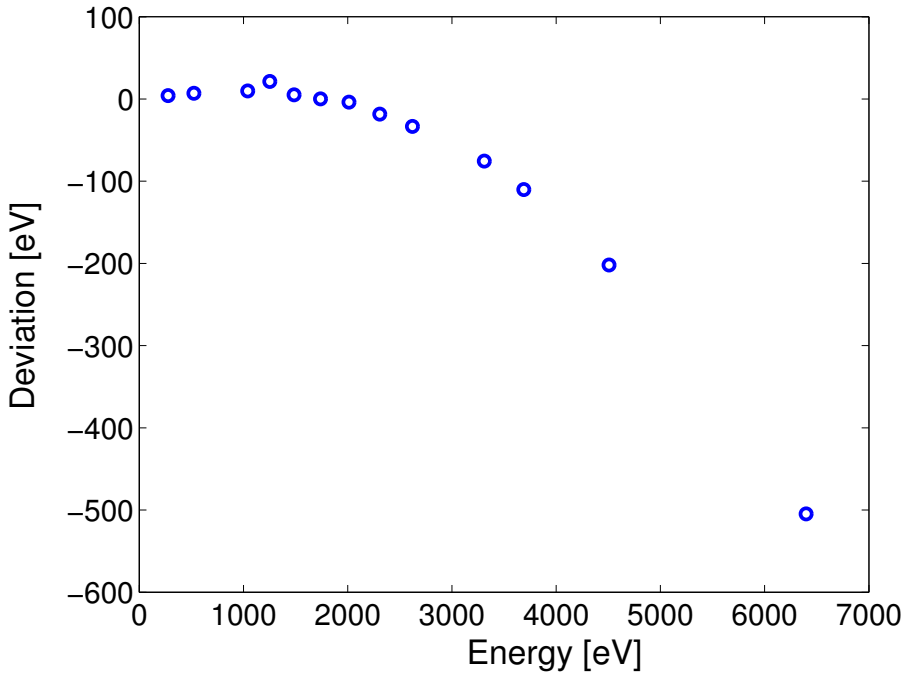

Figure 4.1: Deviation ΔE of measured pulse heights from tabulated X-ray energies $\Delta E = E_m - E_{tab}$ versus energy, Pulse heights are linearly scaled to fit in the low energy range to tabulated X-ray energies

the shape of the function $E_{cal}(A)$ changes with time. Especially after a recharge cycle of the adiabatic demagnetization refrigerator (ADR) changes in the calibration function have been observed. These changes are typically 40-50 eV. A possible reason for these changes is the variation in the magnetic flux in the superconducting electrical connection to the TES. This connection is made of Al that becomes a normal conductor during the recharge cycle of the ADR. When it becomes superconducting again still a high magnetic field can be present at the electrical connections and as a consequence, flux is trapped by the Al wires. This trapped flux changes the magnetic field present at the TES. Thus the properties of the superconducting transition change, leading to a change of the calibration function. Therefore an energy calibration has to be performed frequently, at least after every recharge cycle. For this reason, a practical solution for the calibration problem has to be found. One possibility would be the measurement of a known calibration standard before each measurement but this solution is time consuming and enables a calibration on only several particular energies [Wol97]. For a calibration of the full energy scale an interpolation between these energies has to be performed which causes some error. Also a set of so called heat pulses, artificial pulses generated by electrical heating of the detector, can be used for calibration [Hol01]. But this method proved to be too inaccurate for calibration because the deponated energy for a given heat pulse depends on the detector resistance which is varying. The method presented in this chapter overcomes these problems. An automated calibration routine is generated that fulfills the requirements for everyday use of TES detectors in material analysis. The method is based on the determination of $E_{cal}(A)$ using pulse analysis. As described in section 4.2, in a spectrum the energy of each detected X-ray pulse is calculated within a model that takes electrothermal feedback (ETF) into account and is otherwise characterized by only two unknown constants (c_1 and c_2). These constants have to be determined only once using two lines of known energies, either from a calibration standard, or, if possible, from the sample to be investigated itself. In addition, for each pulse the pulse amplitude A is calculated using an appropriate noise filter. Thereafter, to reduce the error in the determination of $E_{cal}(A)$, average values ($\overline{E}(\overline{A})$) are formed within a small range ΔA around a certain amplitude A and within a small energy range ΔE around the energy E corresponding to A. This process is repeated for many values of A. The average values determine the calibration function $E_{cal}(A)$ as described in section 4.3. The main advantage of this method is that it works without any calibration standards or artificial (e.g. heat) pulses after once determining the constants c_1 and c_2.

4.2 Calculation of the Deposited Energy

If heat is deposited in a TES detector operated in electrothermal feedback mode[1], e.g. after absorption of an X-ray, the detector returns to its equilibrium state via two

[1] see section 3.4

processes. One process is the coupling with the heat bath via the Si_3N_4 membrane, described in Eq. 3.1, the other process is the coupling via ETF as described in Eq. 3.12. So the energy after X-ray absorption can be described by these two heat loss processes:

$$E_{X-ray} = E_{mem} + E_{etf} = \int_{pulse} \Delta P_{mem} \cdot dt + \int_{pulse} \Delta P_{etf} \cdot dt \tag{4.1}$$

where the integration extends over the total length of the pulse. In case of extreme ETF the energy drain via the membrane can be neglected ($G_{mem} \ll G_{etf}$). The drain via ETF is then the only source of power drain [Irw95]. If the detector also has a perfect voltage bias ($R_S \ll R_{det}$) the X-ray energy can then be calculated as:

$$E_{X-ray} \approx E_{etf} \approx U \cdot \int_{pulse} \Delta I \cdot dt \tag{4.2}$$

where U is the voltage at the detector and ΔI is the pulse current. However, with this approximation the calibration of the energy spectra is not good enough, i.e. a calibration accuracy of about half the FWHM of the TES detector could not be reached. In addition the shunt resistor in the readout circuit has a value of about 1/20 of the detector resistance at the working point within the transition whereas for an accurate energy calculation with Eq. 4.2 a value of $<1/1000$ would be required. Finally also the ratio of G_{etf} to G_{mem} is not big enough to allow an approximation where the energy flow via the membrane is neglected. Therefore the calculation model has to be improved to include the changes in the voltage due to changes in the detector resistance and the energy flow via the Si_3N_4 membrane. In linear approximation, the temperature change ΔT is given by:

$$\begin{aligned} \Delta T &= \frac{\Delta P_{mem}}{G_{mem}} = \frac{\Delta P_{etf}}{G_{etf}} \\ \Rightarrow \Delta P_{mem} &= \Delta P_{etf} \cdot c \\ c &= \frac{G_{mem}}{G_{etf}} \end{aligned} \tag{4.3}$$

So the two forms of relaxation, via ETF (Eq. 3.12) and membrane (Eq. 3.1), are proportional to each other. The linear approximation can be used because the temperature change during an X-ray pulse is very small. According to Eq. 3.1, the relative change of G_{mem} is:

$$\frac{\Delta G_{mem}}{G_{mem}} = \beta \cdot \frac{\Delta T}{T} \tag{4.4}$$

So it is of the same magnitude as the relative temperature change ($\Delta T/T < 1/1000$). If the detector is stabilized at the temperature where α is maximal and therefore at the maximum of G_{etf}, the temperature dependence of G_{etf} (see Eq. 3.12) vanishes in first-order approximation. Thus, for small temperature changes, the constant c

changes only slightly. For the following calculation we assume c to be temperature independent during X-ray absorption. The constant c depends, however, on detector bias conditions such as bias current, detector temperature and also on nearby magnetic fields. Assuming c to be temperature independent, the relations in Eq. 4.1 and Eq. 4.3 lead to a proportionality between the energy loss via ETF and the energy of the absorbed X-ray:

$$\begin{aligned} \int \Delta P_{mem} \cdot dt &= c \cdot \int \Delta P_{etf} \cdot dt \\ E_{mem} &= c \cdot E_{etf} \\ E_{X-ray} &= E_{mem} + E_{etf} = (1+c) \cdot E_{etf} \end{aligned} \tag{4.5}$$

The energy loss via ETF can be calculated by integrating the deviation of the equilibrium electrical power ΔP_{etf} from the absorption of the X-ray until the return to the equilibrium temperature. Using the readout circuit scheme (fig. 3.6) the complete electrical power P_{el} (including varying bias voltage) dissipated in the detector can be calculated as:

$$P_{el} = I_{det}^2 \cdot R_{det} = I_{det}^2 \cdot R_S \cdot \left(\frac{I_{Bias}}{I_{det}} - 1\right) = R_S \cdot \left(I_{Bias} I_{det} - I_{det}^2\right) \tag{4.6}$$

The current through the detector can be divided in the equilibrium current I_0 and a signal current ΔI that is caused by energy absorption. Thus, the electrical power can be written as:

$$\begin{aligned} I_{det} &= I_0 - \Delta I \\ P_{el} &= R_S \cdot \left(\left(I_0 I_{Bias} - I_0^2\right) - (I_{Bias} - 2I_0) \cdot \Delta I - \Delta I^2\right) = P_0 - \Delta P_{etf} \\ P_0 &= R_S \cdot \left(I_0 I_{Bias} - I_0^2\right) \\ \Delta P_{etf} &= R_S \cdot \left((I_{Bias} - 2I_0) \cdot \Delta I + \Delta I^2\right) \end{aligned}$$

P_0 is the equilibrium electrical power that heats up the detector to its equilibrium temperature in ETF mode whereas ΔP_{etf} is an additional heat power leaving the detector via ETF e.g. after absorption of an X-ray. Integration of this power results in the heat energy due to ETF. Including P_{mem} the energy of the X-ray is:

$$E_{X-ray} = (1+c) \cdot \int_{pulse} R_S \cdot ((I_{Bias} - 2I_0) \cdot \Delta I + \Delta I^2) \cdot dt \tag{4.7}$$

$$= c_1 \cdot \int_{pulse} (\Delta I + c_2 \Delta I^2) \cdot dt \tag{4.8}$$

$$\begin{aligned} c_1 &= (1+c) \cdot R_S \cdot (I_{Bias} - 2I_0) \\ c_2 &= \frac{1}{I_{Bias} - 2I_0} \end{aligned}$$

The main difference of the energy calculated in Eq. 4.7 to Eq. 4.2 is the quadratic term that is derived from the accurate calculation of the detector voltage. It is not the same as a polynomial fit of second order in a calibration function as it takes care of the energy dependence of the pulse shape. In fact, the calibration function shows large deviations to a polynomial of second order. For practical reasons it is better to determine c_1 and c_2 for a constant operating condition of the detector than I_0 and c. The constant c_1 is used as factor of proportionality of the spectrum whereas c_2 corrects the nonlinearity. With the knowledge of c_1 and c_2 the X-ray spectrum can be completely energy scaled. Once fitted to a known spectrum, these parameters can be used for calibration. The constant c_2 is very stable over time and different recharge cycles as it only depends on the constant bias current and the equilibrium current flowing through the detector that is -according to [Gal03]- connected with temperatures of bath and detector:

$$T_{det}^{\beta+1} - T_{bath}^{\beta+1} = \frac{\beta+1}{G_0} \cdot P_0 = \frac{\beta+1}{G_0} \cdot R_S \cdot (I_0 I_{Bias} - I_0^2) \tag{4.9}$$

As G_0 and β are material constants, the detector current is determined by the temperatures of the heat bath T_{bath} and of the detector T_{det} which are constant and lead to a constant detector current I_0 and therefore a constant c_2.

The value of the constant c_2 can be determined in two ways. One way is by a measurement of the equilibrium current I_0 through the detector, another one is by fitting this constant to a multi element X-ray spectrum. I_0 can not be measured directly with the SQUID amplifier because the SQUID only determines current changes. For this reason the function $I_{det}(I_{Bias})$ has to be measured to determine I_0. This function is recorded by measuring I_{det} while slowly ramping I_{Bias} from 0 to 400 μA (ramping time equals 1s). An example is given in fig. 4.2. Using the plot of fig. 4.2, c_2 can be determined directly for the working point of the detector. We get $c_2 = 3.06\text{E}-2(\pm 1\%)[1/\mu\text{A}]$. The fit of a multi element spectrum results in $c_2 = 3.08\text{E}-2(\pm 3\%)[1/\mu\text{A}]$. Within error bars, both values are in good agreement. The values for c_2 are constant with time and do not change when the ADR is recharged. With the knowledge of c_2, the nonlinearity in the energy spectrum can be removed.

99.7%	99.7%	100.3%	99.8%	100.5%

Table 4.1: Values of the constant c_1 obtained for detector 2 (see table B.1) after several recharge cycles of the ADR. All values are scaled relative to the mean value of c_1

As table 4.1 shows, the constant c_2 changes by less than 1% from recharge to recharge due to a change of the ETF coupling constant G_{etf} with magnetic fields. These magnetic fields can be caused by trapped flux close to the TES.

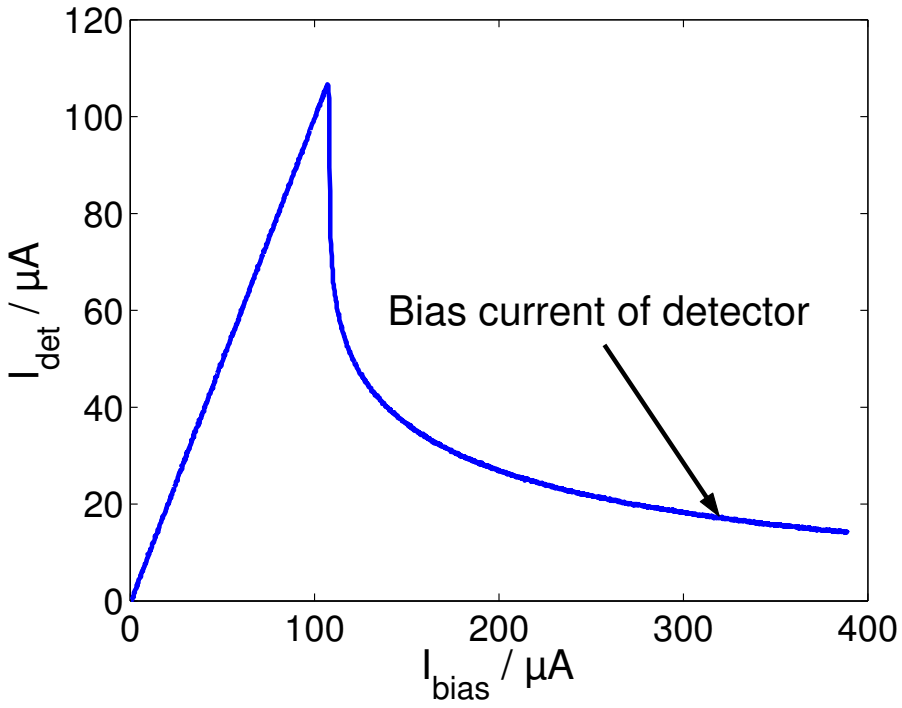

Figure 4.2: Detector current I_{det} vs. bias current I_B at an ADR temperature $T_{bath} = 120\,\mathrm{mK}$, measured with detector 3 (see table B.1)

Even without an exact value for c_1, the energy spectrum is already linearized when c_2 is known and can be completely calibrated by adjusting c_1. The premise for this procedure is the knowledge of the energy of only one X-ray line in the spectrum.

4.3 Energy Calibration of the Pulse Height Spectrum

The creation of a histogram of calculated pulse energies E results in a spectrum with a very good energy calibration. Unfortunately, the energy resolution of such a spectrum is poor (in this setup >60 eV) because usually detector noise is not taken into account. For optimum energy resolution (in this setup ∼10 eV) it is necessary to filter the detector pulses digitally and determine the pulse height A of the filtered pulses (see section 3.5). However, the spectrum of the pulse heights is not linear in X-ray energy so the pulse height spectrum has to be calibrated with respect to energy using a calibration function $E_{cal}(A)$.

The calibration function is determined in the following manner. First, the constants c_1 and c_2 have to be determined by one of the methods described at the end of section 4.2. Thereafter a pulse height spectrum is taken from the sample under investigation. Using Eq. 4.7, for each pulse its energy E is numerically calculated and its pulse height A is recorded. Fig. 4.3 shows an example (small dots). The energy resolution at a particular pulse height A obtained with this procedure is rather poor (∼60 eV in this example) mainly due to detector noise. To improve the energy resolution for a certain pulse height A and its corresponding energy E average values are calculated within a (small) pulse-height window ΔA. This procedure is repeated for many values of A. Fig. 4.4 shows the result (crosses): in this case about 60 different A values have been chosen. The calibration function is obtained for all pulse heights by interpolation between the crosses. The number of pulses used for forming the average within the windows ΔA and ΔE depends upon the intensity present at this particular point (A, E). The average involves many pulses if an X-ray line happened to be close to this point (A, E). This is fortunate, because the averaging process is most accurate at those points in the spectrum where X-ray lines appear.

Thus using $E_{cal}(A)$ for every pulse with pulse height A its energy can be calculated, i.e., a calibrated pulse-height spectrum is formed that combines an optimum energy resolution with a correct energy calibration. This method leads to a rather exact energy calibration (see section 4.4 for examples) if enough pulses are available to form average values for the calibration function with sufficiently low statistical error. The statistical error is given by:

$$\sigma = \frac{\sigma_1}{\sqrt{N}} = \frac{FWHM}{2.35 \cdot \sqrt{N}} \tag{4.10}$$

where σ_1 is related to the full width at half maximum for the energy E of one pulse

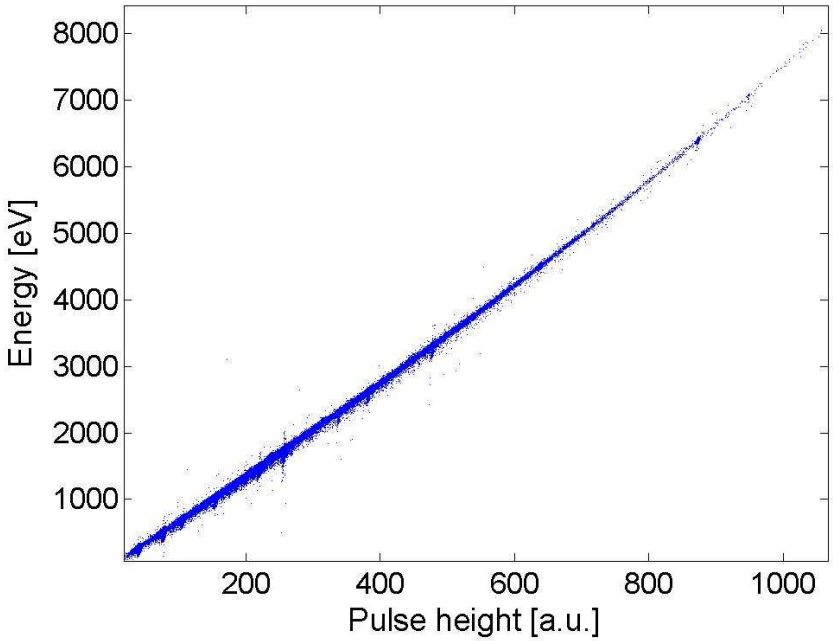

Figure 4.3: Pulse energies calculated (using Eq. 4.7) from corresponding pulse heights for 10000 pulses (small dots) within an energy range of ∼8 keV

(∼ 60 eV) and N is the number of pulses used for forming the average. In the case of the Polaris, already for spectra with a rather low total number (∼1000) of pulses recorded, a sufficiently precise ($\Delta E \leq 10$ eV) energy calibration is possible for all peaks. With longer measurement times the statistical error can be made negligibly small.

4.4 Calibration Results

A glass multi element standard (produced by NIST) and a stone of solidified lava from Etna (a volcano on Sicily) were used to perform the calibration measurements. Both of these samples offer many different X-ray lines in a wide energy range. Fig. 4.5(a) shows a calibrated pulse-height spectrum of the NIST standard measured with detector 1. The calibration function was determined as described in section 3. The constants c_1 and c_2 were obtained from a least-squares fit to the spectrum minimizing the deviations of the calculated peak energies from the tabulated ones. The peak positions in the multi element spectrum in Fig. 4.5(a) were obtained from a Gaussian fit. Fig. 4.5(b) shows the deviations of the tabulated from the fitted energies as a function of the X-ray energy. The deviations are much smaller than the FWHM of the detector (∼10 eV). Fig. 4.6(a) shows a spectrum of the solidified lava measured with detector 2. This detector has the same dimensions

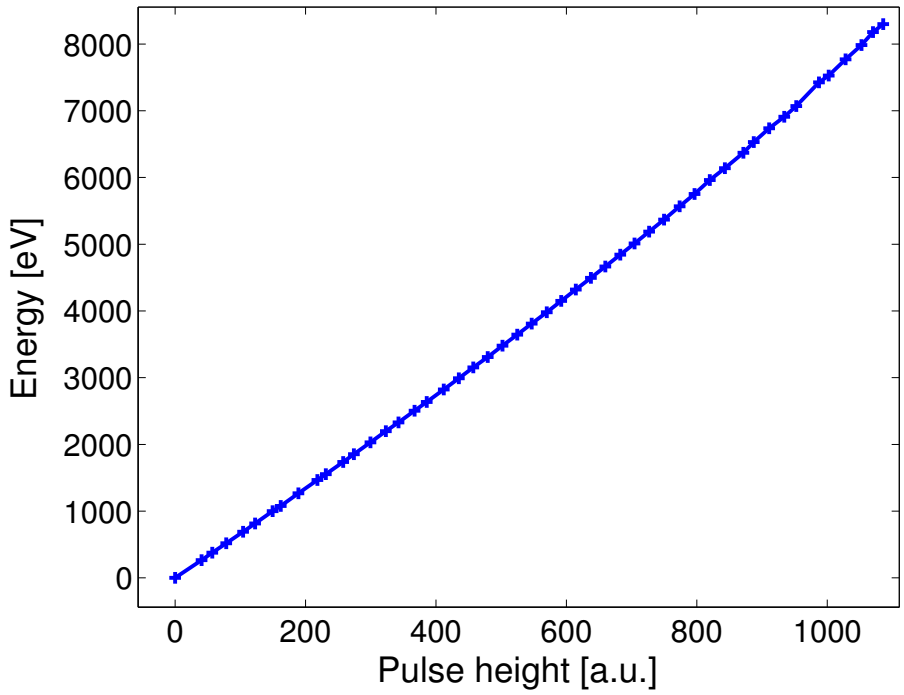

Figure 4.4: Calibration function $E_{cal}(A)$ obtained by an averaging procedure (see text) to determine the energies from the measured pulse heights

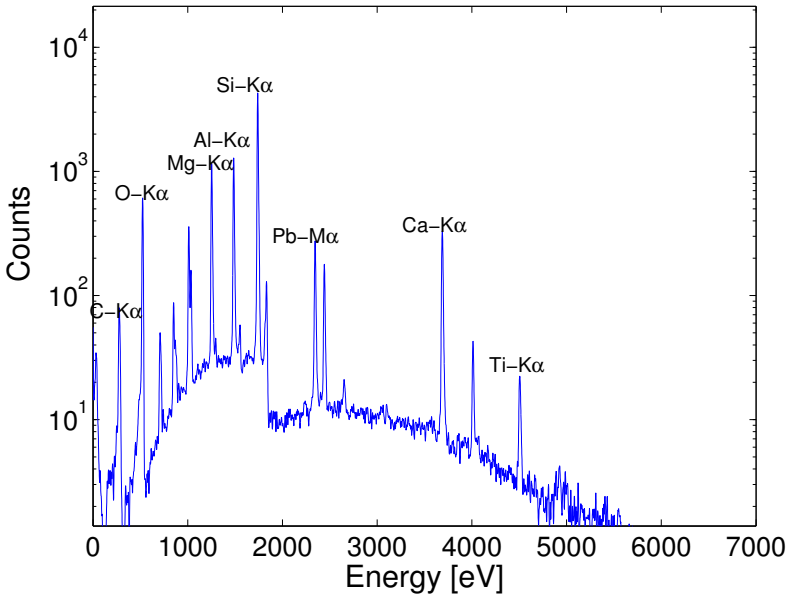

(a) Calibrated pulse height spectrum

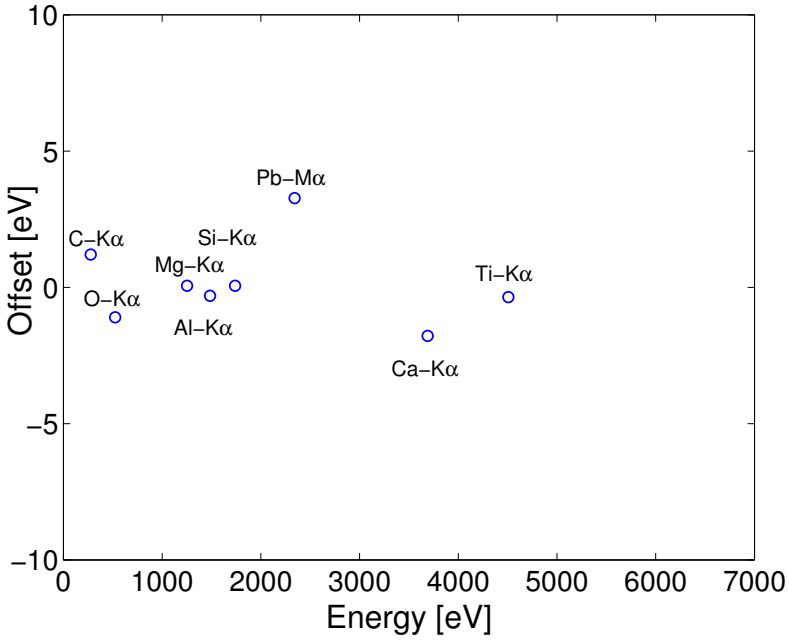

(b) Deviation of peak energies from tabulated energies

Figure 4.5: Calibration result of detector 1 (table B.1), measured with NIST multi-element standard

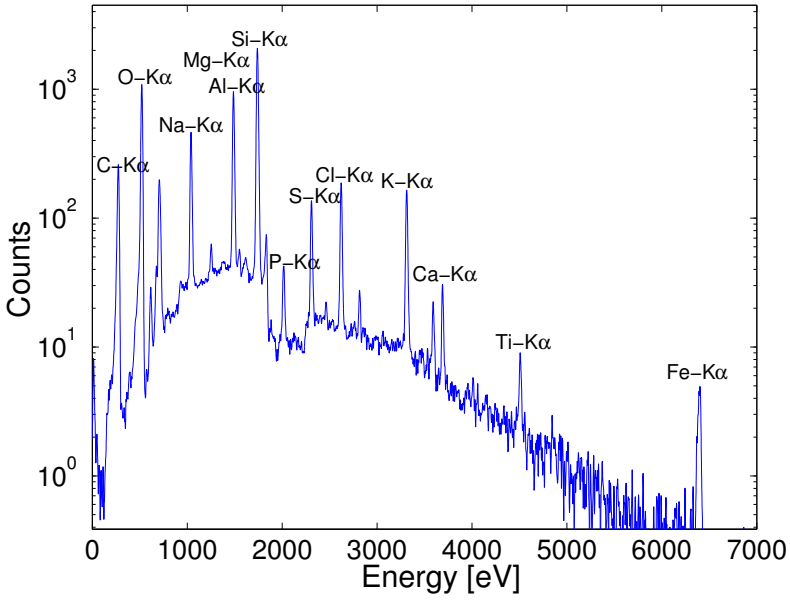

(a) Calibrated pulse height spectrum

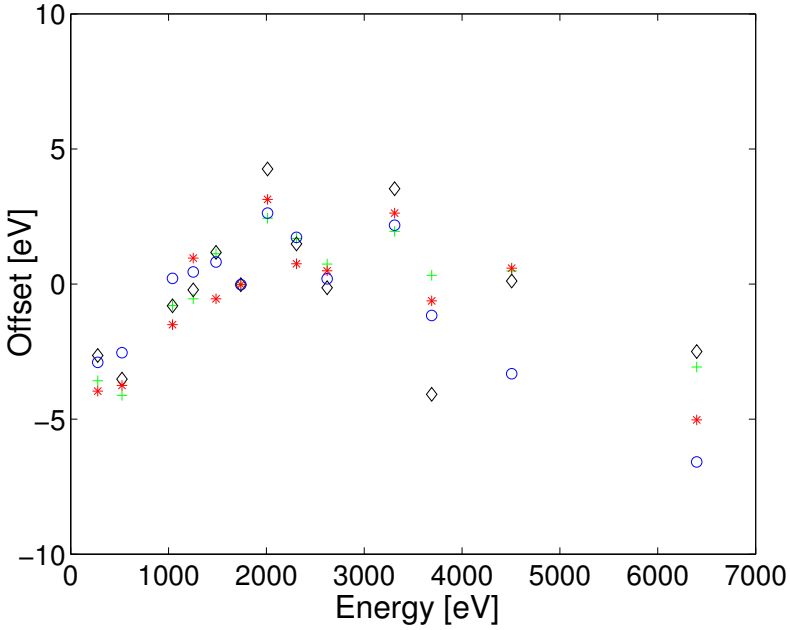

(b) Deviation of peak energies from tabulated energies. The symbols characterize measurements after different recharge cycles.

Figure 4.6: Calibration result of detector 2, measured with solidified lava

as detector 1 but a higher transition temperature of 160 mK. Fig. 4.6(b) presents the deviations of the calculated energies from the tabulated energies of the X-ray lines in Fig. 4.6(a). In this plot different measurements with the same working conditions for the detector after different recharge cycles are displayed. The constant c_2 was fitted once and then used for all measurements whereas c_1 was scaled in each measurement to reproduce the Si $-$ Kα line (1739 eV). A similar measurement has been performed using detector 3 which has a smaller absorber and therefore a lower heat capacity. Due to the lower heat capacity a bigger error in the calibration might be expected than for detector 2. However, as Fig. 4.7 demonstrates, the measurements

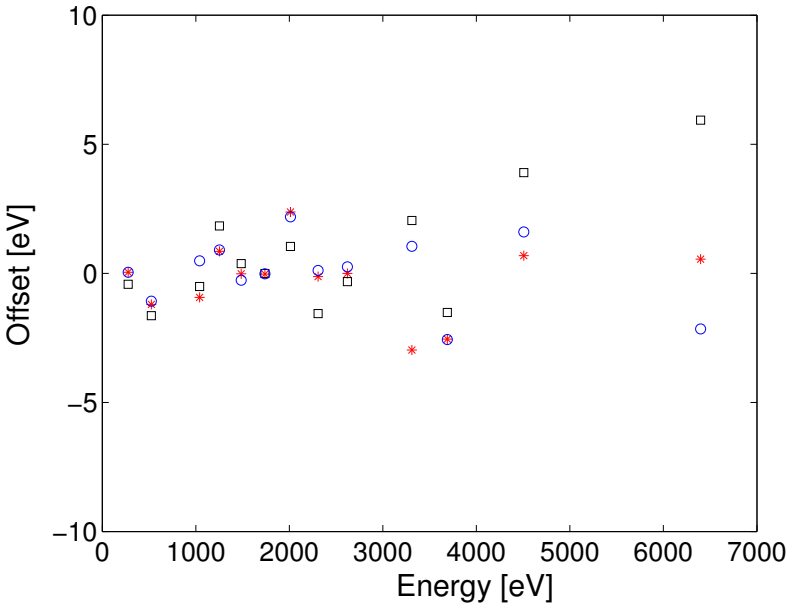

(a) gg

Figure 4.7: Deviation of peak energies in a calibrated pulse height spectrum of solidified lava from tabulated energies, measured with detector 3. The symbols characterize measurements after different recharge cycles.

show an even better result than for the other detectors. This could be caused by smaller nonlinearities in the superconducting transition of this detector or by a better working point. These measurements show that the calibration method described in this paper works convincingly well for different TESs for a wide energy range and is usable over many recharge cycles for a long period of time.

4.5 Conclusion

The presented calibration method for TES sensors has the advantage that the energy information used for calibration is fully derived from X-ray pulses and no further technical modifications such as additional heaters are necessary. Furthermore, no interpolation between large energy ranges has to be made to obtain a complete calibration for all energies as for all interesting peaks an energy value can be calculated. This calibration method is realized by combining two different kinds of pulse analysis, one for optimum energy resolution and another for calibration. Concerning the latter, the possibility of determining the X-ray energy by pulse analysis alone depends on the validity of the relation between the power flow via ETF and via the membrane, Eq. 4.3. As long as this relation is valid and the constant of proportionality c (see Eq. 4.5) is only weakly dependent on temperature it is possible to calibrate TES detectors using Eq. 4.7. Biasing the detector at the maximum value of α enables a very good energy resolution. In first order, α and therefore G_{etf} are independent of temperature. Even if a linear temperature dependence of G_{etf} would be present, the X-ray energy is still calculable, but it would lead to a change in c_2 and to a cubic term of ΔI. In the cases investigated, Eq. 4.7 appears to be accurate enough to correct for the nonlinearity of the superconducting transition of the TES. Changes in the proportionality factor c_1 that are caused by possible changes in G_{etf} due to recharge cycles of the ADR just require the knowledge of one X-ray line in the spectrum to be analyzed. With this method accuracies within a few eV could be achieved in a series of measurements including three different detectors and several recharge cycles. A good energy calibration is important for a correct interpretation of EDS spectra especially if only a few elements and X-ray lines are known. The described method fulfills the needs of a calibration procedure for EDS as it enables calibration accuracies better than the energy resolution of the detector.

Chapter 5

Integration of TES Detector, Pulse Tube Cooler and SEM

For the development of a TES based microanalysis system, a mechanical pulse tube cooler, a TES detector and a SEM had to be combined.

The application of a pulse tube cooler has the advantage that no liquid gases such as nitrogen and helium are needed. This is the presumption for the operation of the system in a cleanroom environment where liquid coolants are forbidden and also has the advantage of easier operation of the system because refilling is unnecessary. Another advantage is the lower weight of this cooling system compared to a filled liquid helium system. This simplifies the attachment of the TES-EDS system on a SEM. Mechanical coolers have the disadvantage that mechanical vibrations can cause disturbances for the operation of the TES and the SEM. Although the used pulse-tube cooler is low-vibrational due to the separated rotary valve, vibrational influences on the SEM and the TES detector occurred.

Another integration problem that had to be solved was an unacceptable long measurement time for standard spectra due to the low number of X-ray events measured by the TES detector in the SEM. The low number of absorbed X-ray events was caused by the small absorbing area of the detector in addition to a quite low X-ray intensity in the used SEM that only allows low beam currents of about 1 nA at 5 kV acceleration voltage.

By solving these integration problems a powerful microanalysis system could be developed, enabling several new applications for EDS analysis.

5.1 Influence of Cooler Vibration on the SEM

One problem of the pulse tube cooler attached to a high-resolution SEM is the vibrational influence on the SEM image. These vibrations were a serious problem for high-resolution imaging in the SEM [Hol01]. This could be improved by two changes in the system. One was the construction of a new rotary valve holder that succeeded in reducing the movements of the rotary valve due to pressure changes. Thus, the

Figure 5.1: TES EDS system Polaris attached on LEO 1550 SEM

transfer of these movements to the cooler was suppressed and the cooler vibrations could be reduced. The other advance was the construction of a new slide block including big areas of sorbothane, an elastic material that absorbs vibrations. With these two changes the vibrations were reduced by a factor of about 4 in comparison to [Hol01]. So an acceptable SEM operation with attached Polaris system is possible. Fig. 5.2 shows the remaining vibrations with an amplitude of 3 nm. Line integration mode for the SEM is the repeated scanning and adding up of each line of the SEM image. This mode enables the further reduction of the remaining influence on the SEM image.

5.2 Microphonic Disturbance

Another problem caused by the vibrations of the pulse tube cooler is the influence on the TES signal. As the measured current change in the TES (see fig. 3.9) is quite low it can be easily influenced by external disturbances leading to a decrease in energy resolution. So the components in the readout circuit are, as far as possible, covered with a superconducting shield to protect the circuit from external magnetic fields such as the fields generated by the SEM. But this shield can not completely protect the readout circuit because it can not be applied to all components e.g. the detector. So the external influence on the readout circuit can not be suppressed completely. Fig. 5.3 shows the recorded TES signal influenced by cooler vibrations. This disturbance has a very large amplitude when the gas flows into the pulse tube cooler. Fig. 5.4 shows an X-ray pulse with a large vibrational influence (start of gas

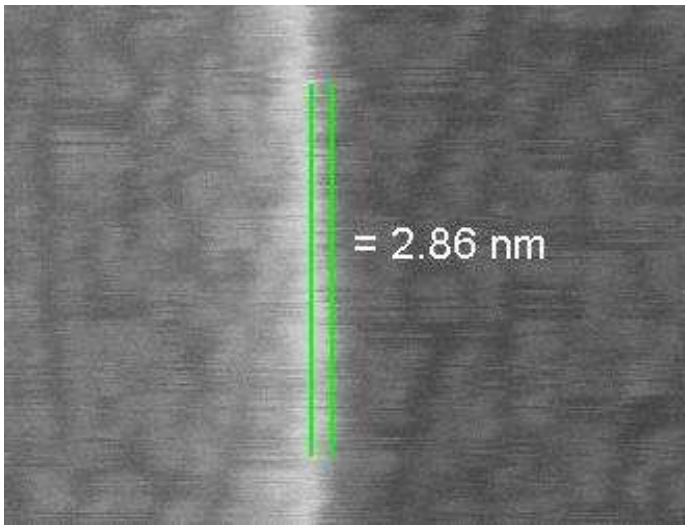

(a) SEM image with vibrations of pulse tube cooler

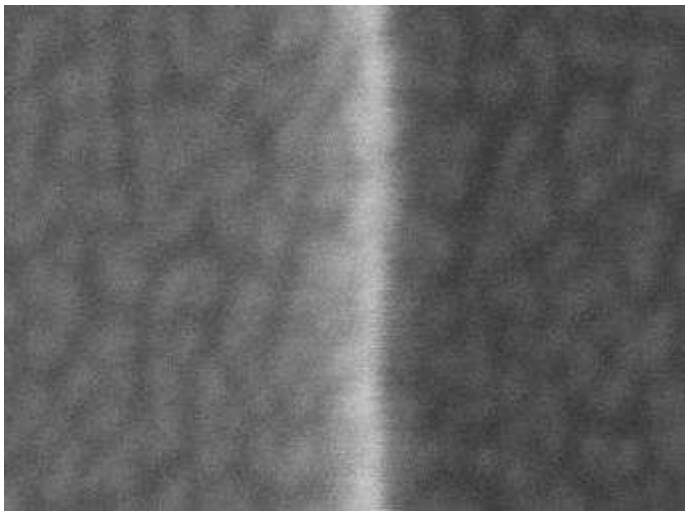

(b) SEM image without pulse tube cooler

Figure 5.2: Comparison of SEM images with and without operating pulse tube cooler

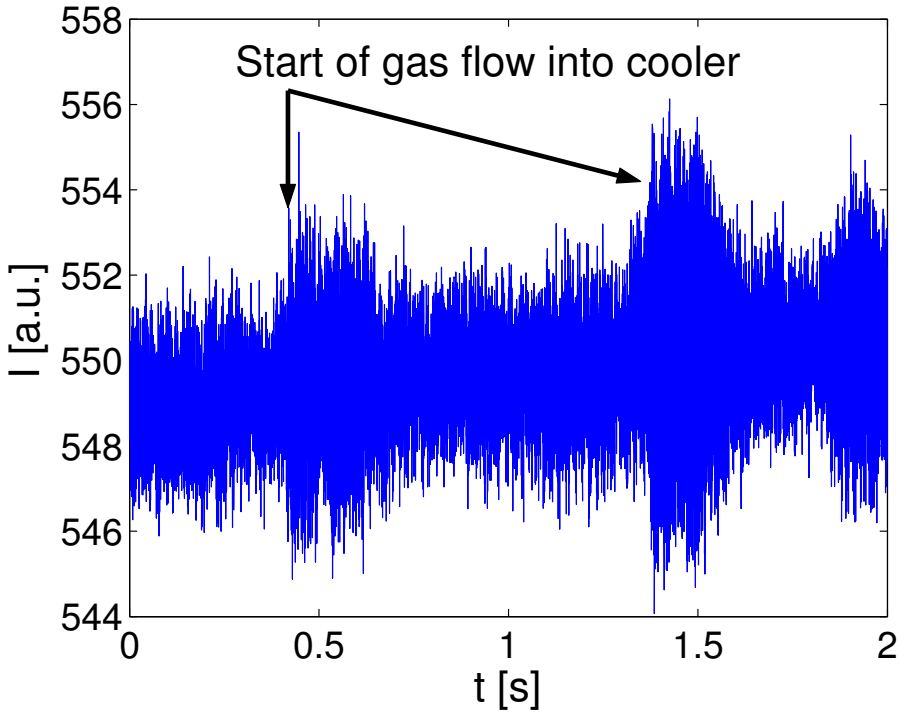

Figure 5.3: Detector current as function of time (without X-ray events), with pulse tube cooler in operation

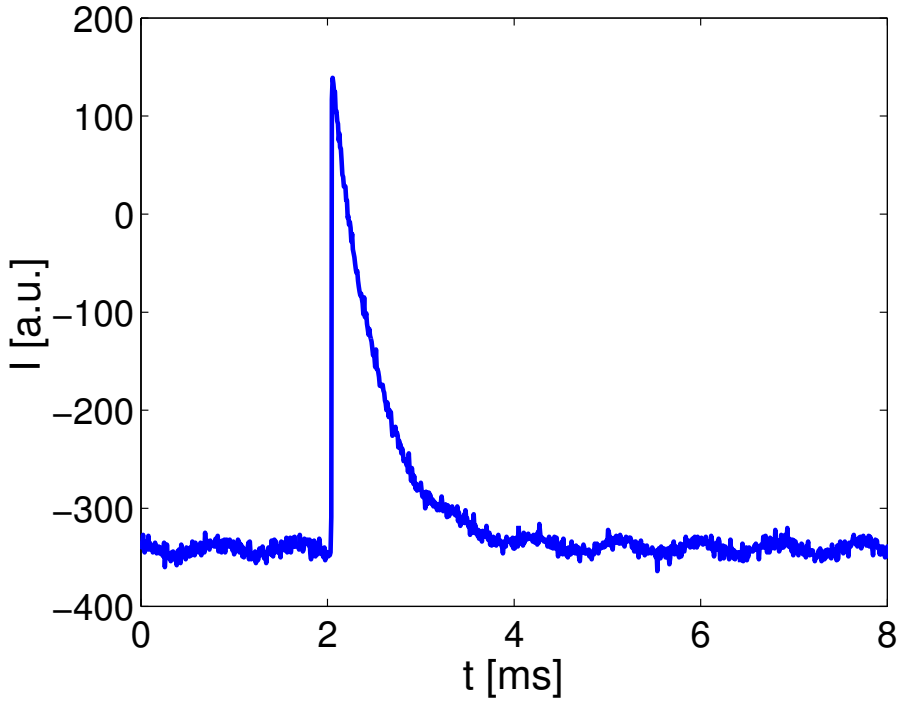

Figure 5.4: Si Kα pulse with large vibrational influence (start of gas flow into cooler); Notice the oscillation with about 1 kHz (compare with fig. 3.9)

flow into the cooler). A strong oscillation with a frequency of 1 kHz is visible. This is a frequency range where also large amplitudes in the pulse frequency spectrum can be found. So this frequency leads to a big error in the pulse amplitude determination. But also the mechanical vibrations at higher frequencies (30-50 kHz) increase the error in pulse amplitude determination. These oscillations can be detected in the noise power spectrum in fig. 5.5 and result in an increased FWHM of X-ray lines in the spectra. If the pulse tube cooler is turned off, this influence disappears and the energy resolution of the detector improves significantly. But turning off the cooler is only possible for a short time because the temperature of the 4 K stage nearly instantly increases and after about 1 minute also the bath temperature of the ADR stage increases and can not be stabilized any longer. To improve the FWHM for longer measurement times the influence of the pulse tube cooler on the electrical readout circuit has to be suppressed.

Experiments with changes in the shielding of the electrical wires in the readout circuit revealed that the most sensitive wires were the connections between the ADR stage and the SQUID. When these experiments were performed the SQUID was mounted at the 4 K stage because the used SQUIDs were not operable below a temperature of 0.9 K and could therefore not be mounted directly on the ADR stage.

A superconducting shield for these wires is difficult to realize, because the heat power flowing to the ADR stage due to the thermal link becomes too large if the wires are completely surrounded by a shield such as a Pb foil. So the foil shield has to be interrupted between the 4 K stage and the ADR pill which leads to an incomplete shielding and residues of the vibrational influence. To find a tradeoff between heat load and shielding impact is difficult and therefore the experiments to build such a shield are time consuming. A better solution is the application of a SQUID that is operable on the ADR stage. With such a SQUID (fabricated by Supracon Technologies) the critical connections can be avoided and all wires in the readout circuit can be shielded properly. Fig. 5.5 shows a comparison of the noise power spectral density with vibrational influence (SQUID mounted at 4 K stage) and of a noise power spectral density with much less vibrational influence (SQUID mounted on the ADR pill). The reduction of the vibrational noise leads to an improvement of the best achieved detector FWHM of 6.5 eV (see fig. 6.1).

5.3 Count Rate Increase with a Polycapillary Lens

5.3.1 Count Rates with TES Detectors

The SEM used for all the TES measurements in this thesis was a LEO 1550. This SEM has a quite low maximum beam current of about 1 nA at 5 kV whereas other types of SEMs have beam currents up to 1 mA. Lower beam currents are, however, typical for many high-resolution SEMs equipped with field emission guns. With low beam currents the emitted X-ray intensity is also quite low. The detected X-ray

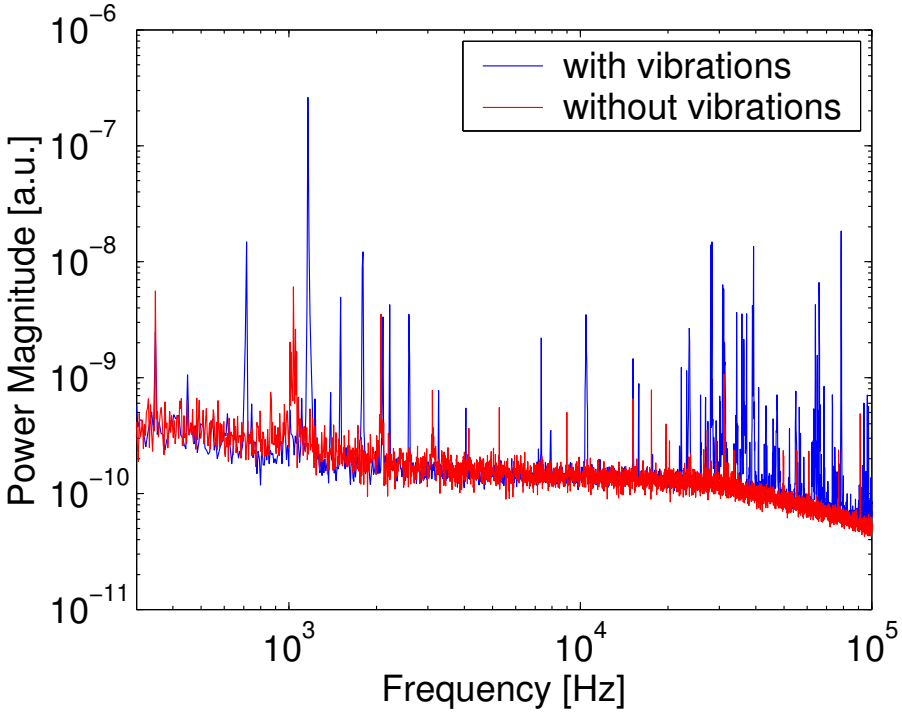

Figure 5.5: Comparison of noise power spectra with large and low vibrational influence; Notice large vibrational amplitude at about 1 kHz and peak series at about 30-50 kHz

intensity, the so called count rate of the detector, is proportional to the emitted X-ray intensity and the covered solid angle of the EDS detector. The solid angle is the ratio of absorbing area of the detector to the square of the distance between specimen and detector $\Omega = A/d^2$. Si(Li) detectors present an absorption area of about $10\,\mathrm{mm}^2$. The distance between specimen and detector is about $5\,\mathrm{cm}$. With the resulting solid angle, an X-ray spectrum can be acquired in some minutes even with high-resolution (low beam current) SEMs. The collection area of most of the TES detectors used in this work is only $0.063\,\mathrm{mm}^2$, which is 160 times lower than the area of standard Si(Li) detectors. The solid angle of TES detectors is also about 160 times lower than for Si(Li) detectors because the distance between detector and specimen is for the TES detector system approximately the same than for Si(Li) detectors. Thus TES measurements are very time consuming. In addition to the small area, the detected X-ray intensity is lowered by the absorption of low-energy X-rays in the light-blocking windows in front of the detector[1]. This problem is especially accute for elemental mappings and quantitation where a large number of X-ray events is needed to minimize statistical errors and get a satisfactory measurement result. Thus, it is of considerable importance to overcome this disadvantage.

One possible solution would be to increase the absorber area. However, this leads to an increase in heat capacity of the detector and therefore to a decrease in energy resolution. Another possibility is to increase the beam current. But this increases the beam damage to the sample and complicates the analysis of small volumes with electrical charging effects of the sample. The most promising solution for this problem is the application of an X-ray lens. For the case in study a polycapillary lens is used. This lens increases the count rate due to an increase of the effective collection area and a decrease of the distance between sample and effective collection area as seen in fig. 5.6.

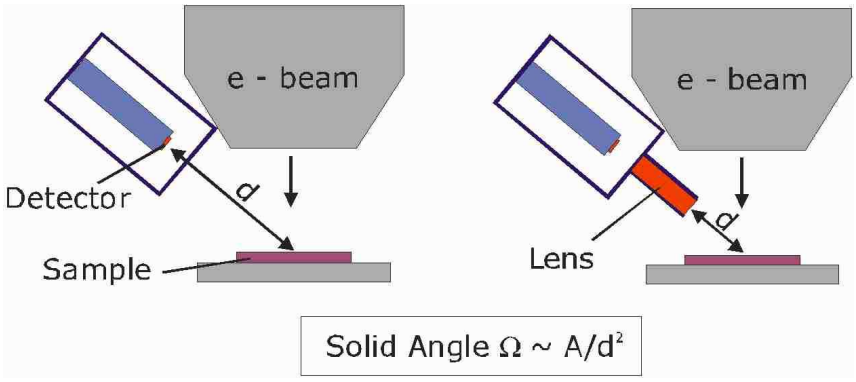

Figure 5.6: X-ray collection geometry with and without lens

[1] see fig. 6.22

5.3.2 Operation Principle

Polycapillary focusing optics, consisting of tens of thousands glass capillaries, can collect X-rays over a broad energy range. This offers manifold applications including the focusing of an X-ray beam in microbeam analysis [Sch02]. A bundle of curved capillaries is used as a lens, imaging one focal point at the sample to the other at the detector as shown in fig. 5.7. Each capillary serves as a directional guide for X-rays

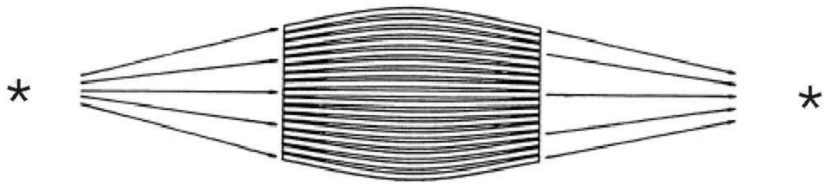

Figure 5.7: Schematic view of polycapillary lens

in a similar fashion as a solid glass fiber does for visible light. The capillaries are orientated towards the two focal spots. This works as long as the X-rays are incident on the channel walls at angles less than the critical angle for total reflection. To ensure this the dimension of each capillary has to be much smaller than its radius of curvature $R > 2d/\Theta_c^2$, where d is the diameter of the capillary, and Θ_c is the critical angle for total reflection. Polycapillary optics are currently made of glass because of its high surface smoothness and formability. For silica glass, the critical angle is,

$$\Theta_c = 30\,mrad \cdot keV/E \tag{5.1}$$

where E is the X-ray energy. This equation already indicates that the spot sizes of polycapillary lenses are energy dependent. But the spot sizes also depend on other effects like absorption processes inside the lens and inexact alignment of the capillaries with respect to each other. With these boundary conditions polycapillary lenses are designed to fit optimally to the needed energy range, solid angle and geometrical requirements in the SEM. The optics are constructed by heating a straight polycapillary bundle and drawing it into the desired profile. Each channel has to be oriented towards the source at the entrance and is directed towards the focus at the exit. The lens used in the Polaris setup was produced by XOS Technologies Inc. According to the manufacturer's specifications it has an input focal length of 9 mm with a capture angle of 19.2°, an output focal length of 22.4 mm and a transmission efficiency of 9.4 % at 930 eV. The input focal point size at 930 eV is 0.18 mm and the output focal spot size is 0.45 mm at the same energy.

5.3.3 Transmission Properties

The goal was to increase the count rate of the Polaris to enable measurement times in the magnitude of some minutes. The result was an increase in count rate by

Figure 5.8: Photo of the lens in steel enclosure

a factor of 120 as measured with a Si sample at an acceleration voltage of 5 kV and a sample current of approximately 1 nA. A plot of the dependency of count rate on acceleration voltage, both with and without lens is shown in fig. 5.9. For a more exact calculation of count rate the total number of counts over 1 minute was taken. The achieved increase in count rate enables analysis methods such as mappings, linescans (see subsection 6.4) and the analysis of low concentrations (see subsection 6.2).

The absorption of X-rays in the glass capillaries of the lens causes an energy dependant X-ray transmission function as shown in fig. 5.10. In this plot the absorption edges (see section 1.2) of oxygen and silicon, the main constituents of glass are especially noticeable: they cause sharp edges in the transmission efficiency. The energy dependant transmission function of the lens makes a major contribution to the calculation of the detection efficiency.

The shape of this energy transmission function depends strongly on the alignment of the lens - the critical angle of reflection for glass is energy dependent (Eq. 5.1) and thus, the spot size of the lens changes also with energy. This property can be illustrated by scanning an electron beam across an homogeneous sample with two or more lines at different energy e.g. a Ti-Al-alloy. Because the sample is homogeneous, the intensity of the characteristic X-ray radiation is proportional to the transmission efficiency at the corresponding energy. With a plot of the transmission efficiency with respect to the electron beam position, the spot size can be determined. Fig. 5.11 shows the intensity distribution of the Ti Lα (452 eV), the Al Kα (1486 eV) and the Ti Kα (4507 eV) line after scanning over a 500 μm $\cdot$ 500 μm

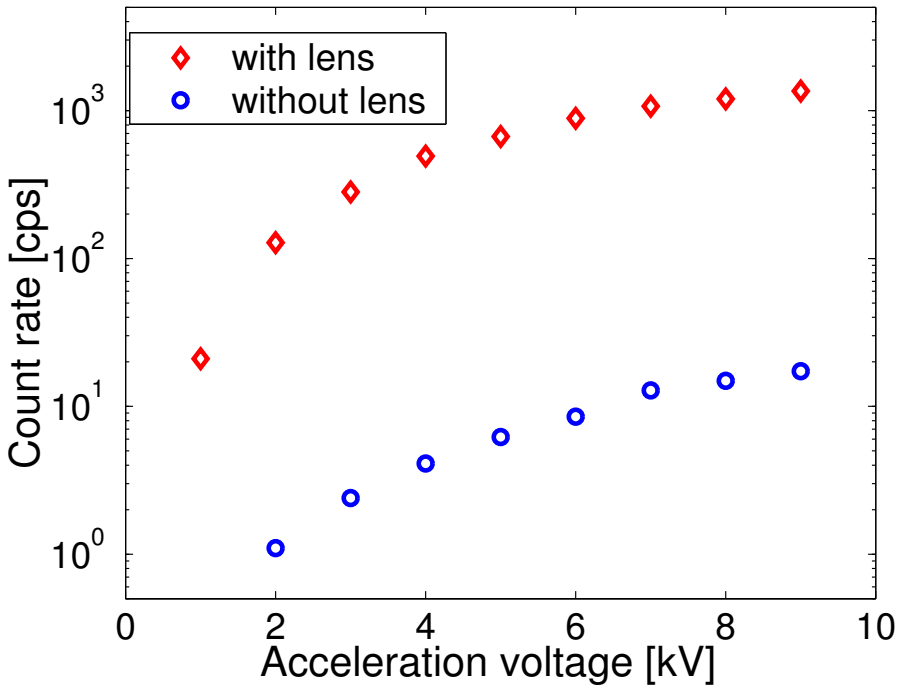

Figure 5.9: Count rate vs. acceleration voltage on Si; with and without lens for comparison. The plot with lens is normalized to the same beam current without lens

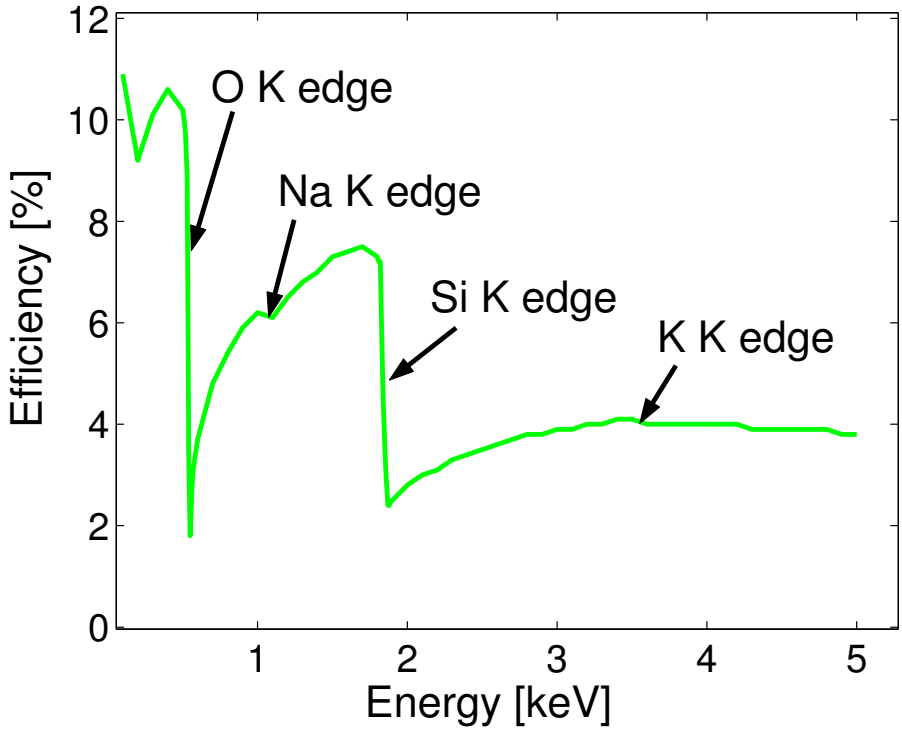

Figure 5.10: Transmission efficiency of the lens vs. X-ray energy (measured by XOS); absorption edges are marked

area of the alloy. Gaussian fits to these distributions yield spot sizes (expressed as FWHM) of 154 μm for Ti Lα (452 eV), 143 μm for Al Kα (1486 eV) and 76 μm for the Ti Kα (4507 eV). These values cannot be explained with Eq. 5.1. It can be assumed that additional effects, such as absorption processes in the lens or a non-isotropic alignment of the capillaries, contribute to these transmission profiles.

The energy dependency of the spot size leads to a change in the transmission efficiency if the lens is not aligned correctly because the decrease in count rate due to misalignment is different for different energies. Thus, intensity ratios of different characteristic X-ray peaks in measured spectra are alignment dependent. It is, therefore, extremely important to align the lens accurately, especially for quantitative measurements (see subsection 6.5).

5.3.4 Adjustment with the X-Ray Tube

To integrate the lens into the Polaris EDS system it has to be aligned to both detector and sample. A stable alignment method is then necessary to ensure accuracy inside the SEM. One possible method was demonstrated by a group at NIST [Wol97]. A translation stage was used to manipulate the lens between snout and sample to get an optimum signal gain with the lens. For the Polaris system a solution is preferred where the lens can be directly mounted to the snout. This enables the withdrawal of the snout together with the adjusted lens. Normal imaging in the SEM is somewhat easier with a withdrawn snout and the danger of damaging the lens with the sample stage is eliminated.

The application of a polycapillary lens requires that the two focal spots be adjusted towards the detector and the X-ray source. The X-ray source in the SEM is the intersection point where the electron beam enters the specimen. The adjustment is accomplished in two steps. In the first, the lens is aligned towards the detector by the use of an X-ray tube. This is done outside the SEM chamber. The second step is the adjustment of the detector with attached lens towards the intersection point of electron beam and sample.

For the adjustment of the lens towards the detector a special holder for the lens has been developed. It is attached to the snout of the Polaris, and allows the shifting of the lens parallel to the snout (z-direction), and in two orthogonal directions perpendicular to the snout (x- and y- direction). It also allows the adjustment of the angle between the snout axis and the optical axis of the lens. Four screws are used for the adjustment in z-direction while other eight screws are needed to clamp and move the lens in the other direction.

To test the adjustment of the lens a low-energy X-ray tube is used. The distance between anode and the tube's X-ray window is kept below the input focal length of the used lens so that the focal spot of the lens can be placed on the anode. The window of the tube consists of a 6 μm plastic foil and allows the transmission of low-energy X-rays. The acceleration voltage is kept below 5 keV because there are legal restrictions for the operation of X-ray tubes with higher energies. 5 keV is

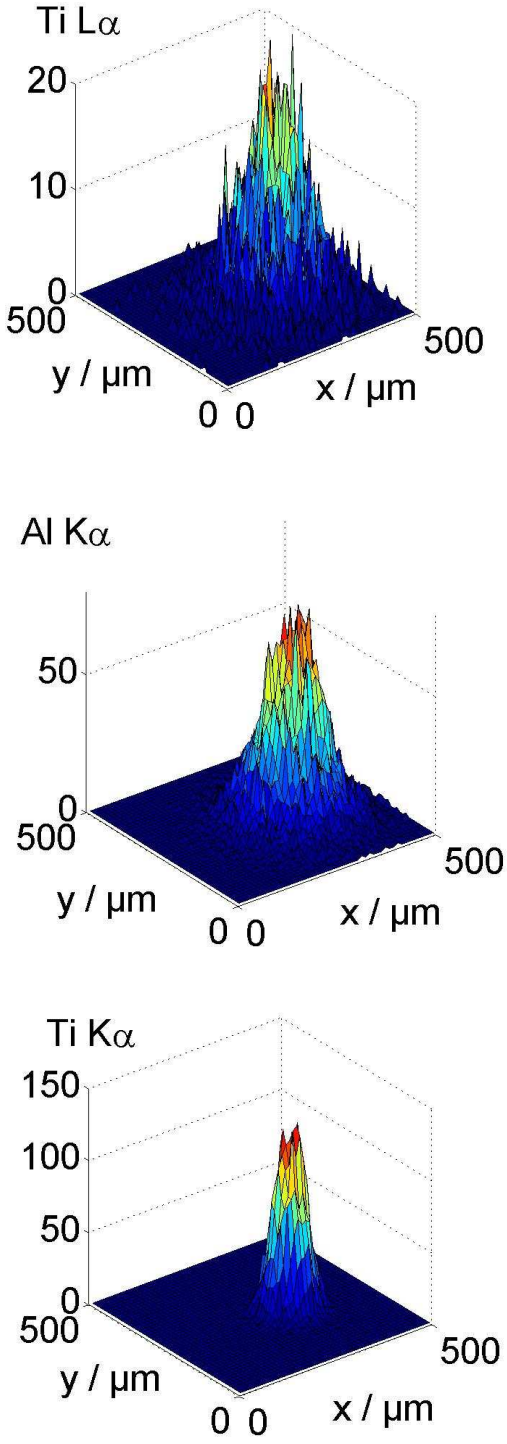

Figure 5.11: Spatial transmission profile of the lens for Ti Lα (452 eV), Al Kα (1486 eV) and Ti Kα (4507 eV)

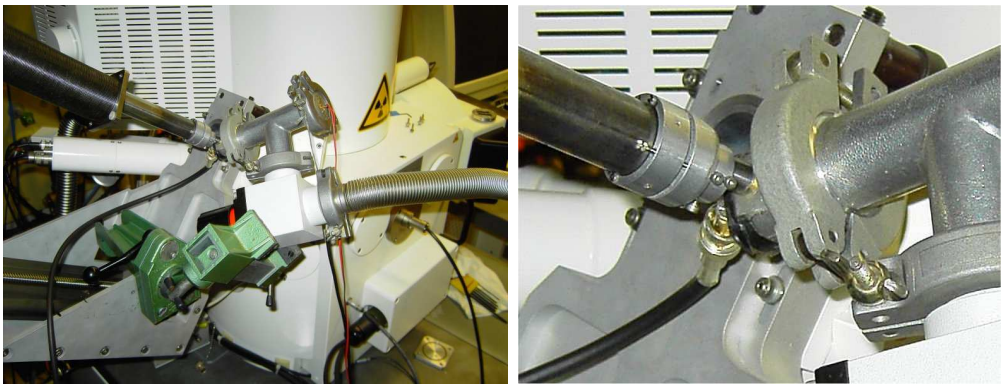

Figure 5.12: Snout with attached lens and X-ray tube, setup for lens adjustment towards detector

also sufficient because the detection efficiency of the system decreases with energies much larger than 3 keV. A small light bulb filament is used as cathode. The anode material is a Pt/Pd alloy and has an area of 1 mm^2. The alloy emits characteristic X-ray radiation at 2048 eV and at 2830 eV. With an anode of this size it can be easily ensured that the focal spot of the lens is in cover with the anode of the tube. So the output focal spot can be adjusted to the detector without bothering about the corresponding movement of the input focal spot.

The alignment of the lens towards detector begins with an estimation of the detector position inside the snout using the X-ray tube and a small aperture. This has to be done because the position of the detector inside the snout is not exactly known. The aperture is placed between X-ray tube and detector. The tube has to be aligned until X-rays are detected with the TES. As soon as this is achieved, the line defined by anode and aperture points directly at the detector.

As soon as the position of the detector is determined, the lens is aligned roughly in the direction of the detector. The distance between lens and detector is chosen to be a little larger than the focal length so that the lens focus is widened to about 1 mm^2. With this X-ray spot it is quite easy to find the detector by scanning with the lens around the estimated position of the detector. After the first X-ray events are detected by the TES the optical axis of the lens has to be aligned optimally to the detector. This is done by aligning the lens until the count rate is maximized. Afterwards the distance between lens and detector is lowered and the count rate maximized again. This procedure is repeated until the optimum distance between lens and detector is found and therefore the focal spot of the lens is adjusted towards the detector.

After aligning the lens towards detector, the snout is inserted into the SEM. Inside the SEM the optical axis of the lens can be adjusted to cross the electron beam by rotating the whole Polaris system on its mount-plate on the microscope slide. The sample has to be brought to the intersection of the optical axis and the

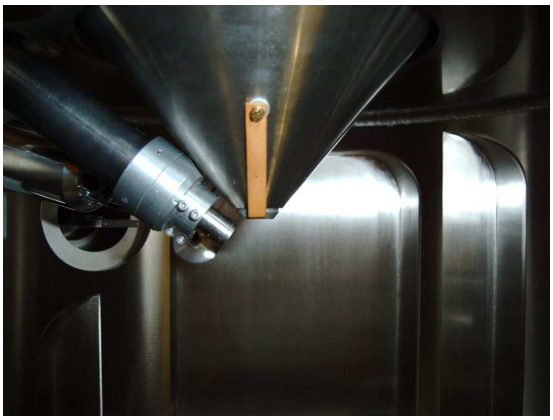

Figure 5.13: Snout with aligned lens in SEM

focussed electron beam. When this is accomplished the distance between pole piece of the SEM and the focus of the electron beam, the so called working distance, is determined. The intersection point can be recovered with another sample by setting the working distance to this measured value and changing the distance between pole piece and sample until the SEM image is focussed.

After the initial alignment, further re-alignments are easy and it is quite simple to do measurements with the Polaris TES system with attached lens.

Chapter 6

Applications of the Polaris EDS-System

6.1 Resolution of Neighboring Lines

The most important feature of the Polaris TES detector system is the ability to resolve neighboring X-ray lines of element combinations such as Ti/N, W/Si or Si/Ta. Such low-energy X-ray line combinations cannot be resolved by conventional Si(Li) detectors [Sim02] because of their insufficient energy resolution. For the analysis of small volumes such as particles or thin layers low acceleration voltages have to be used (compare section 1.2). But with the use of low acceleration voltages also only low-energy X-ray lines are excited and therefore an energy resolution is needed that is sufficient to separate these lines. The ability to resolve X-ray lines is characterized by the full width at half maximum (FWHM) of the detector response to a specific X-ray energy. The FWHM is the width of the distribution of the measured X-ray energies at half its maximum value. The FHWM of a gaussian distribution is correlated with the standard deviation σ thus:

$$FWHM = 2.35 \cdot \sigma \tag{6.1}$$

The Polaris FWHM is specified for the Al Kα line at 1486 eV. The best measured value for the FWHM was 6.5 eV obtained at a bath temperature of 53 mK and a detector bias of 100 μA with an Ir/Au detector[1]. Typical values for the FWHM were about 10 eV. Fig. 6.1 shows the related Al spectrum. This best measured value of the FWHM is a factor two better than that reported in [Hol01] although the same detector was used. The improvement was achieved by lowering the microphonic noise (see section 5.2) and the bath temperature of the cryostat. This FWHM is more than 10 times better than that of typical Si(Li) detectors (83 eV) and allows the Polaris to resolve tightly neighboring X-ray lines.

The resolution is determined by detector responsivity and detector noise. Thus, as long as the detector response is linear to the energy the resolution is expected

[1] detector 1 in table B.1

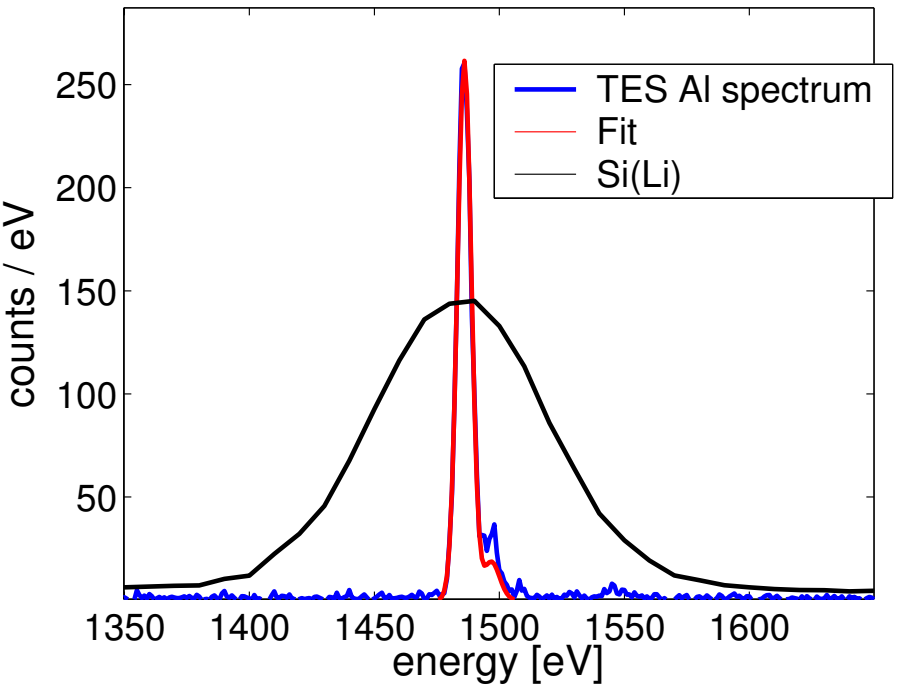

Figure 6.1: Spectrum of Al at 5 kV and corresponding fit resulting in a FWHM of 6.5 eV, measurement time was 2 min

to be constant. But also additional effects can contribute to the FWHM e.g. the detector response can depend on the position where the X-ray hits the absorber. Fig. 6.2 shows the FWHM as function of X-ray energy of one of the used detectors[2]. The shape of this function depends on the detector because it is determined by the detector's intrinsic properties such as the shape of the superconducting to normal-conducting transition. For the detector used in this measurement it remains nearly constant up to the Ti Kα (4507 eV) and then increases significantly for Fe Kα (6398 eV). Thus, for the interesting energies below 3 keV it can be taken that the FWHM is approximately constant.

One important combination of elements in the semiconductor industry is W/Si. If a low-energy electron beam is used only the M lines of W are excited. The W Mα and Si Kα are separated by 35 eV and so they cannot be resolved with Si(Li) detectors. In semiconductor devices W is used to form contacts between different conductor levels as shown in fig. 6.3. The contact hole shown below is a connection between an Al metalization and a poly-Si gate. It is typically embedded in SiO_2. An elemental mapping[3] shows the distribution of the different elements. For EDS measurements near these structures it must be possible to distinguish these elements, especially if W or SiO_2 particles have to be analyzed. Fig. 6.4 shows two spectra

[2]detector 3 in table B.1
[3]see section 6.4

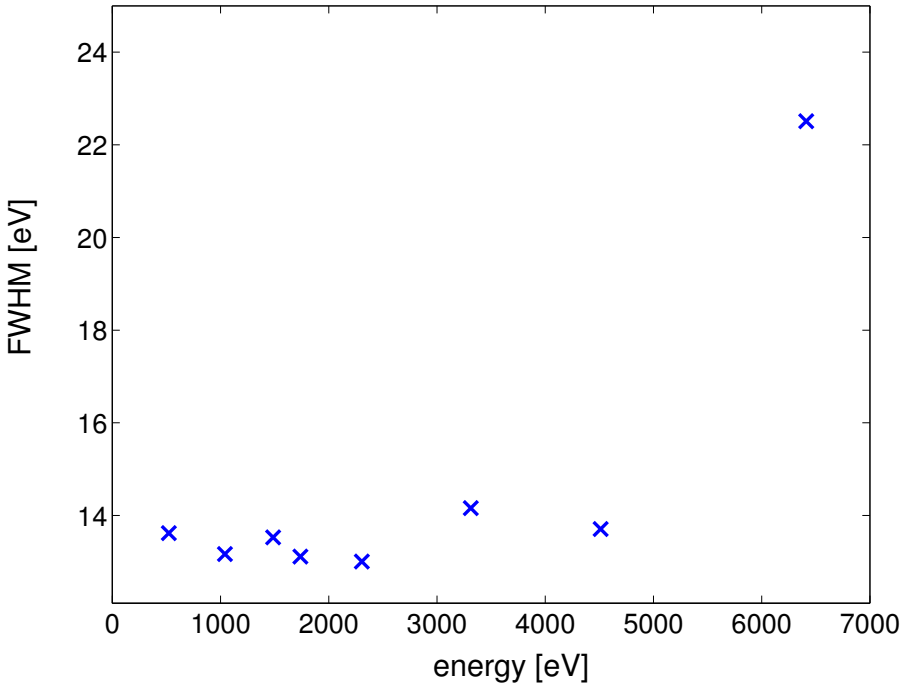

Figure 6.2: FWHM versus energy for detector 3 (see table B.1), measured with a sample of solidified lava

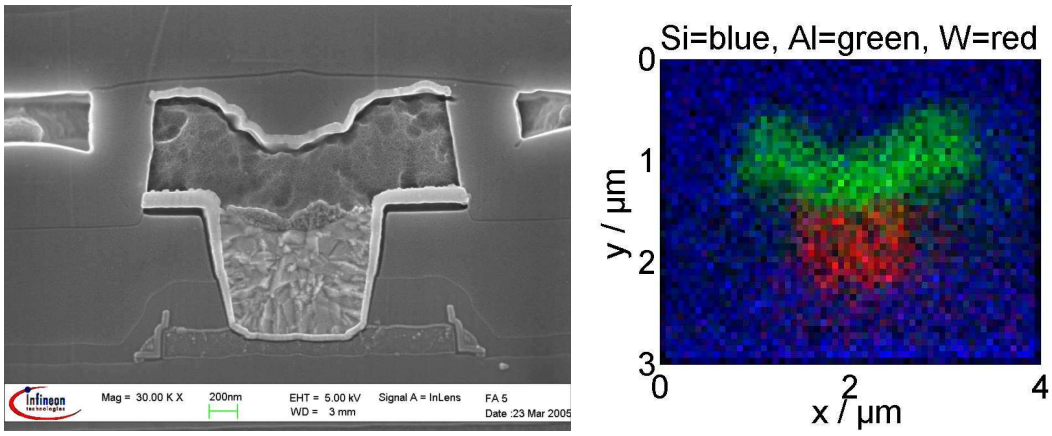

(a) SEM Image

(b) Element mapping of contact hole

Figure 6.3: W contact hole

of WSi_2. The TES spectrum clearly separates these lines whereas the peaks in the

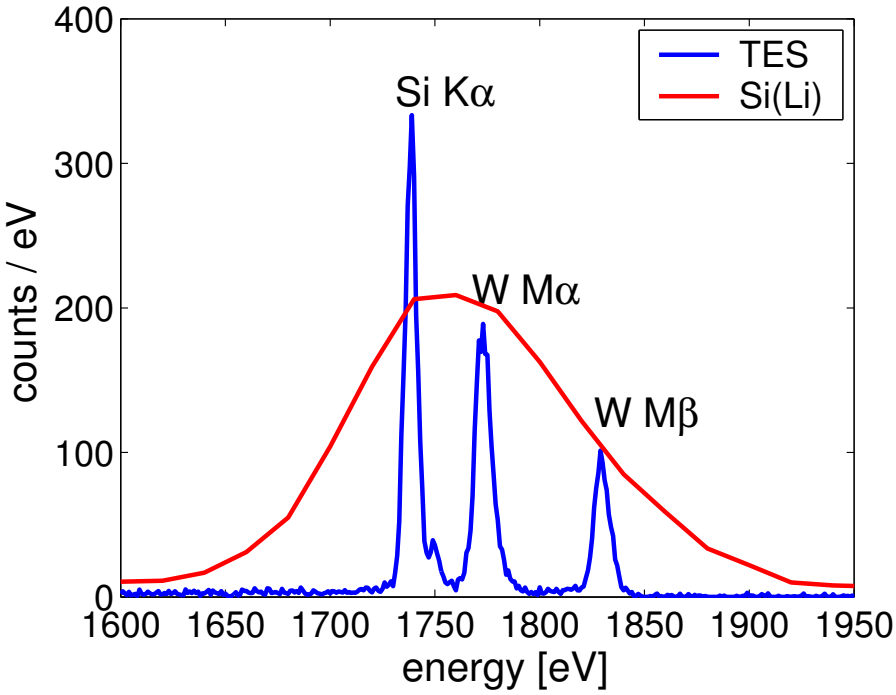

Figure 6.4: Spectrum of WSi_2 at 5 kV, measurement time: 2 min ($I_B = 100\,\mu A$, $T_{bath} = 55\,mK$, $I_{beam} = 64\,nA$)

Si(Li) spectrum are overlapping.

Another example for overlapping peaks in Si(Li) spectra is the element combination Ta/Si with a difference of 30 eV between Ta Mα (1709 eV) and Si Kα (1739 eV). The difference between Si Kα and Ta Mβ (1765 eV) is 26 eV. TaN is used as diffusion barrier between Cu and SiO_2 in contemporary devices with Cu metalization. In fig. 6.5 the peaks are clearly separated in the TES spectrum whereas in the Si(Li) spectrum only one peak can be recognized. The peak in the Si(Li) spectrum is, compared to a peak of pure Si, only broadened but the mean energy is not shifted because the Ta M peaks surround the Si peak. This is a further complication in the analysis of this material combination with Si(Li) detectors.

The layer system Ti/TiN is used as diffusion barrier between SiO_2 and W. The energy difference between Ti Lα(452 eV) and N Kα(392 eV) is 60 eV. As these elements are used in semiconductor fabrication it is also possible for particles of these materials to emerge as defects or contamination. For analysis of such particles it is important to distinct between Ti and TiN. This is especially difficult as the Ti Ll line has an energy of 390 eV and therefore overlaps completely with the N Kα line (392 eV). The intensity of the Ti Ll line is nearly the same as the intensity of Ti Kα. So only the intensity of the peak at 390 eV is different between a Ti and a TiN

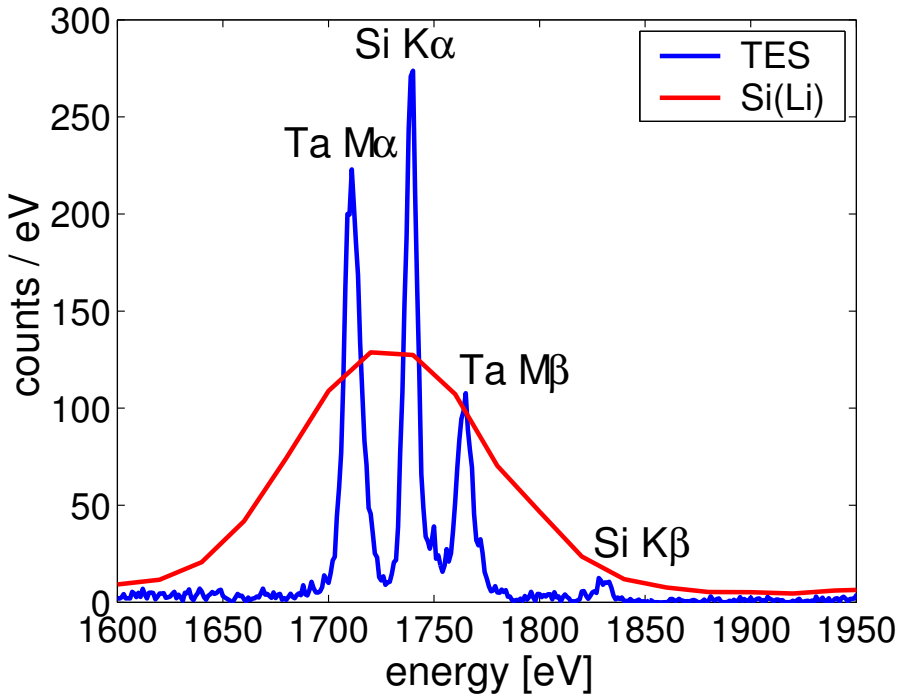

Figure 6.5: Spectrum of $TaSi_2$ at 5 kV, measurement time: 2 min ($I_B = 100\mu A$, $T_{bath} = 55mK$, $I_{beam} = 64nA$)

spectrum. To determine this intensity correctly a clear separation of the Ti Lα and the N Kα is necessary. Fig. 6.6 shows a comparison of the spectra of TiN of a TES and a Si(Li) detector.

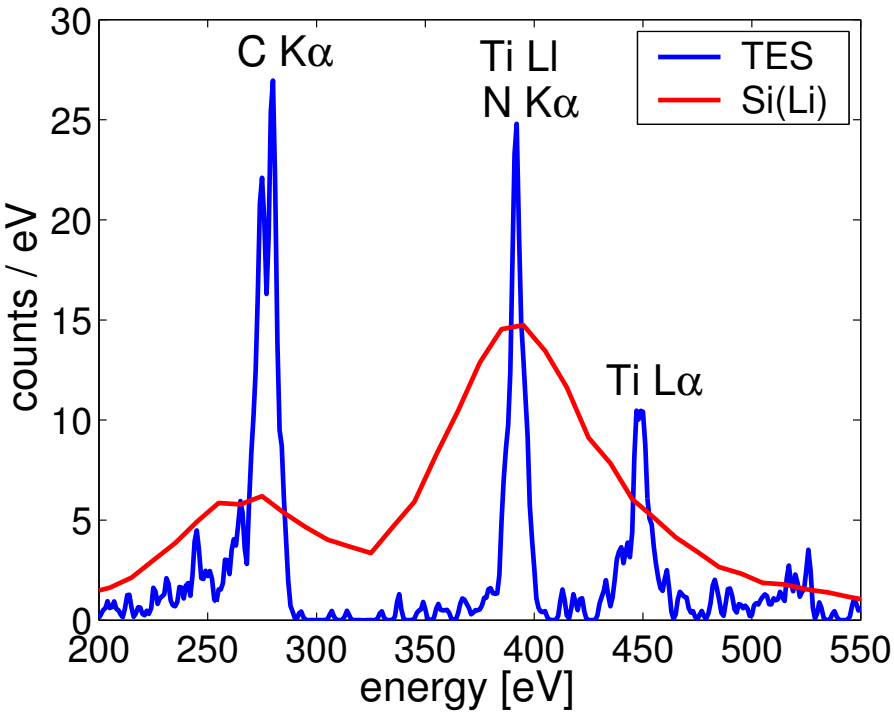

Figure 6.6: TES and Si(Li) spectrum of TiN at 5 kV, measurement time: 2 min ($I_B = 100\mu A$, $T_{bath} = 55mK$, $I_{beam} = 64nA$)

There are plenty of examples with closely neighboring X-ray lines that are important in manifold applications. The improved peak resolution and sensitivity of TES detectors adds new possibilities in EDS.

6.2 Detection of Small Concentrations

An important property of EDS systems is the detection limit for the concentration of an element in a specimen. This limit is determined by the ability to detect the characteristic peaks in a spectrum. To do this it is necessary that the peak intensity appears dominant over the statistical fluctuations of the background. The statistical lower limit of detection depends on measurement time, FWHM and count rate:

$$LLD \sim \sqrt{\frac{FWHM}{rate \cdot time}} \tag{6.2}$$

For very long measurement times there is another limit for the detection of a peak in a spectrum. The background is determined by the composition of the sample, the

acceleration voltage, the take-off angle (described in table B.2) and the efficiency of the detector. Hence, it can be difficult to calculate the background contribution. A peak in a spectrum is undetectable if the peak amplitude is lower than the uncertainty of the background in the same region. This limit is a time independent detection limit. It is, however, proportional to the peak to background ratio and therefore indirectly proportional to the FWHM of the detector for a given peak intensity[4]. Thus, with an improved peak to background ratio TES detectors have the ability to improve this limit when compared to Si(Li) detectors.

Fig. 6.7 shows a spectrum of Si doped with $1,2 \cdot 10^{19}\, As\, atoms/cm^3$, which corresponds to a mass fraction of $0,05\,\%$. The As Lα and As Lβ lines are clearly visible

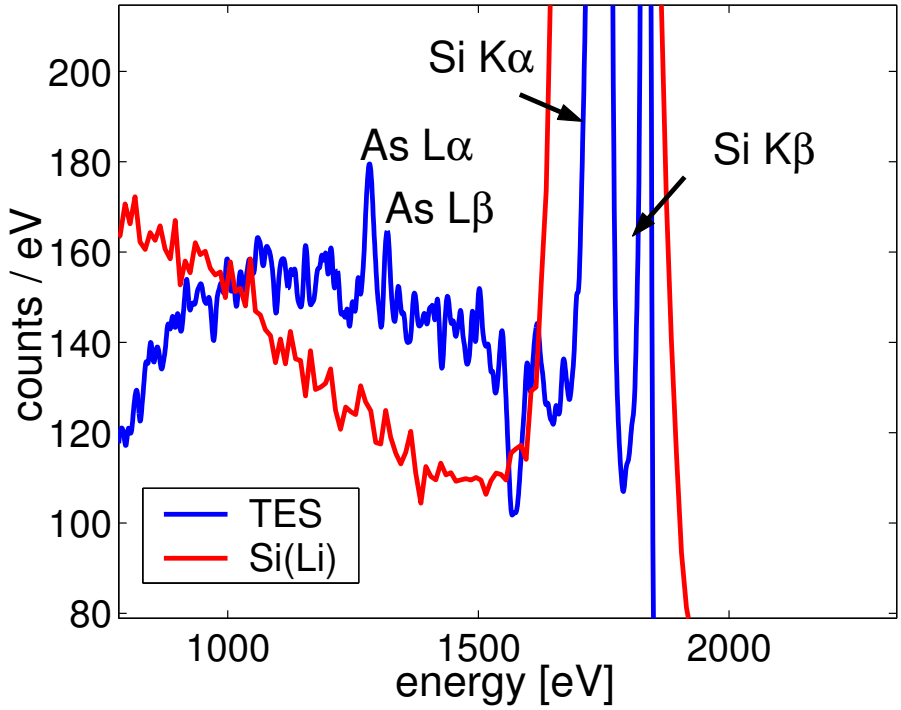

Figure 6.7: Si doped with 0,05 % As, measurement conditions for both spectra, TES and Si(Li) (acceleration voltage = 3 kV, measurement time = 2 h and I_{beam} = 180 nA)

in the TES spectrum after a measurement time of 2 h. Note that the background uncertainties in this spectrum are still dominated by statistical fluctuations which means that a far better detection limit can be achieved by increasing the measurement time further. Fig. 6.8 shows a spectrum of Si doped with $4 \cdot 10^{19}$ P atoms/cm^3 which was measured in 70 min. In this example the P peak is also clearly visible in the spectrum.

[4] see subsection 6.1

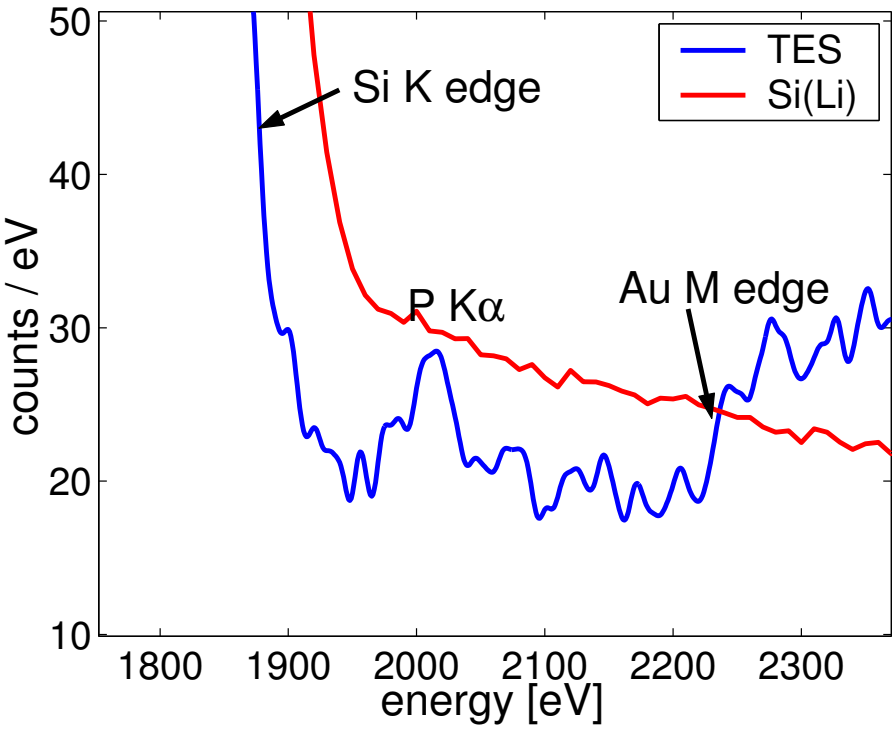

Figure 6.8: Si doped with 0,09 % P, measurement conditions for TES spectrum: (acceleration voltage=5 kV, measurement time=70 min, $I_{beam} = 620\,\mathrm{nA}$)

It is clear then that TES detectors allow a greatly improved detection limit in EDS measurements over the same time and measurement conditions when compared to the traditional Si(Li) detectors. They also improve the time independant detection limit because of the lowered background uncertainty.

6.3 Chemical Shifts

The energy of X-ray transitions and intensities are influenced by the chemical surrounding of the emitting elements [Dod68]. The change of the X-ray emission line energies due to chemical influences is called chemical shift. Large chemical shifts are seen for X-ray lines where the electron involved in the transition originates in the valence band that is affected most by the chemical bonding of the element. Chemical shifts yield information about the chemical surroundings of an element in a specimen [Gra77]. Normally, the line shifts have a magnitude measured in single electron Volts and thus cannot be detected with conventional Si(Li) detectors. Systematic measurements of this effect were done with WDS spectrometers operated in electron microprobes [Dod68]. These often cumbersome spectrometers offer energy resolutions of about 1 eV.

The possibility of detecting chemical shifts in EDS measurements opens a completely new field of application because conventional EDS spectra only contain information about the *elemental* constitution of the sample. But with the possibility of detecting chemical shifts also the *chemical* constitution can be determined, thus delivering much additional information about the sample. The excellent energy resolution of TES detectors have already been used to chemical shifts as demonstrated in [Wol00].

With the Polaris, a determination of chemical shifts is possible although detector resolution, expressed in eV, is larger than the chemical shifts. This can be achieved if the fluctuations of the detector calibration during the EDS measurement are lower than the magnitude of the chemical shifts. If the detector calibration is sufficiently stable and a sufficient number of characteristic X-ray events (N) is detected the errors of the peak positions ($FWHM_{Max}$) are much lower than the detector FWHM:

$$FWHM_{Max} = \frac{FWHM_{det}}{\sqrt{N}}$$

The detector FWHM was about 15 eV when this measurement was done. $FWHM_{Max}$ is better than 0.15 eV if more than 10000 X-ray events are measured and the detector signal is stable. In order to stabilize the detector signal, the measurement of chemical shifts was done quasi-simultaneously by scanning over a cross-section that consisted of a section of boron-phosphorous-silicate-glass (BPSG) and a section of pure Si. As each line in the scan takes about one second, drifts in detector calibration are the same for the peaks of both sections and calibration is exactly the same. Thus differences in detector drift between the two materials are eliminated.

A thin metallic Pt layer is sputtered onto the sample surface in order to ensure good electrical conductance to prevent sample charging. The Pt line is not affected by the chemical shifts because it is a metal layer. The Pt peaks should appear at exactly the same energies in the data being received from both sections of the sample. Fig. 6.9 shows a good agreement of the Pt Mα in both layers. Gaussian fits

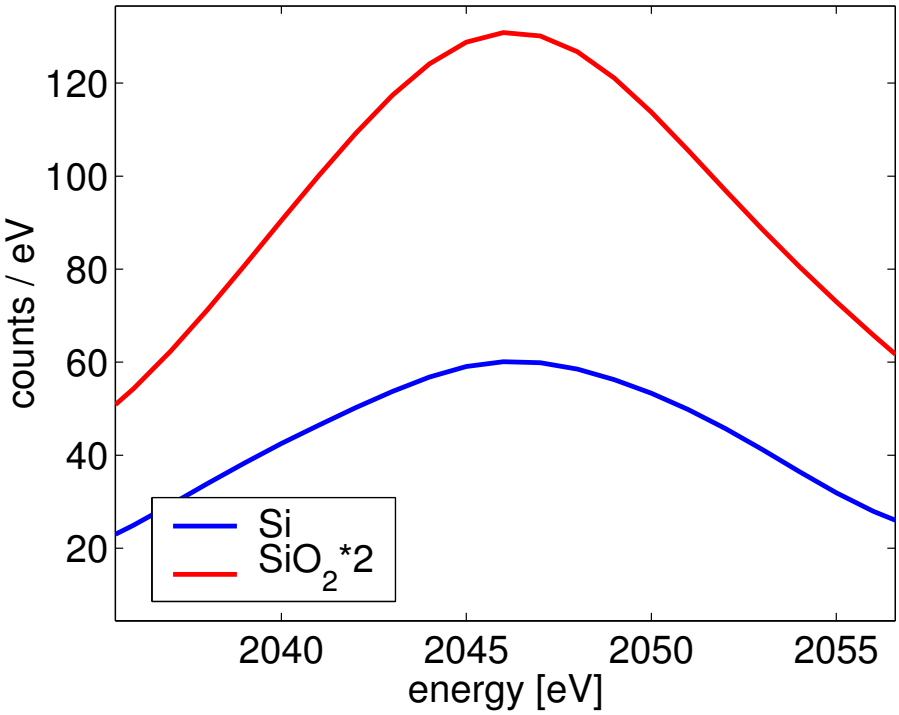

Figure 6.9: $Pt - M\alpha$ of sputter coating of both layers

of the two peaks result in a deviation of 0.1 eV between the SiO_2 layer and the Si layer. The Pt Mα line can be used to ensure that the detector calibration is identical for both layers and the chemical shift is measured correctly. So fig. 6.9 shows that the calibration is the same for both layers.

Fig. 6.10 shows a comparison of the Kα peak of pure Si to the Kα peak from the BPSG as measured with the Polaris TES system. BPSG mainly consists of $Si0_2$ mixed with about 5 % of B and P. They show a clear shift of the maximum of the Si Kα. The chemical shift between SiO_2 and Si was determined with gaussian fits to the spectra in fig. 6.10 resulting in 0.7 eV. This value is in good agreement with [Gra77] where the measurement of the chemical shift resulted in 0.58 eV. The small deviation of the value from WDS measurement can be explained with a statistical error and with a different silicon oxide. The amorphous SiO_2 in fig. 6.10 is doped with B and P, whereas in [Gra77] crystalline SiO_2 was used.

The Si Kα in Si is shifted to higher energies when oxidized whereas the energy of Kβ is lowered and the intensities of the satellite peaks change. In fig. 6.11, the

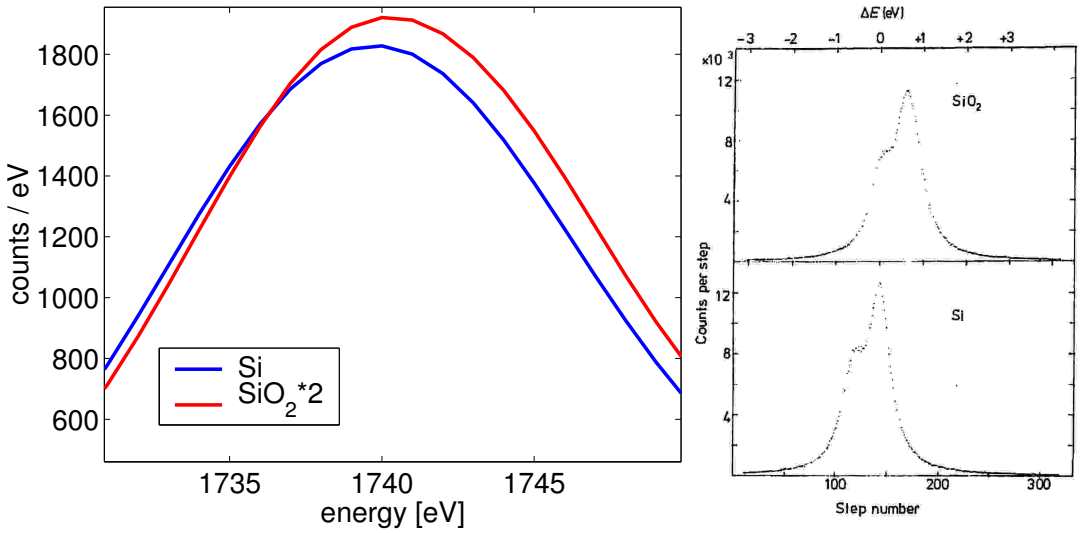

Figure 6.10: $Si - K\alpha$ of pure Si and SiO_2, measured at 4 kV with TES (left) and with WDS (right) [Gra77]

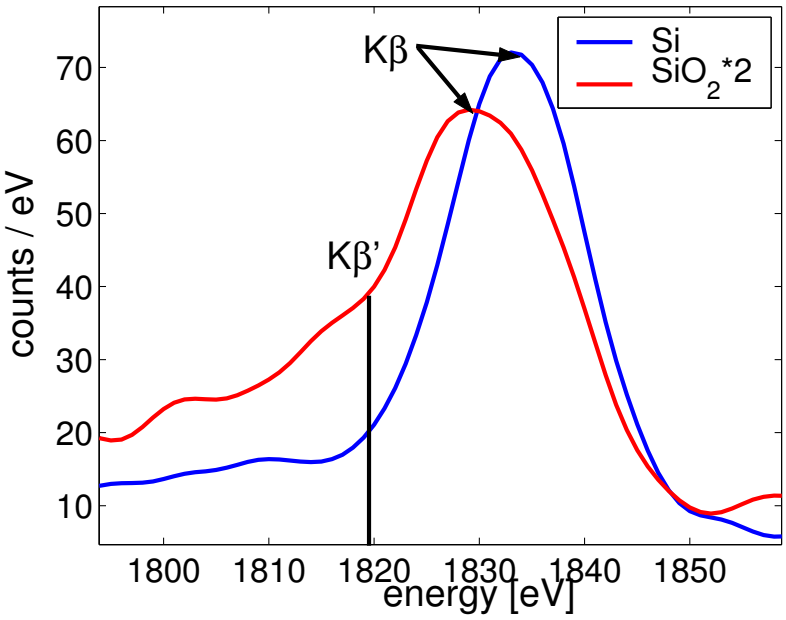

Figure 6.11: $Si\,K\beta$ of pure Si and SiO_2, measured with 4kV

Kβ spectra of Si and SiO_2 are plotted with a chemical shift of 4 eV. In [Dod68] this value was determined to 4.2 eV (fig. 6.12). Also the Kβ' peak that can only be

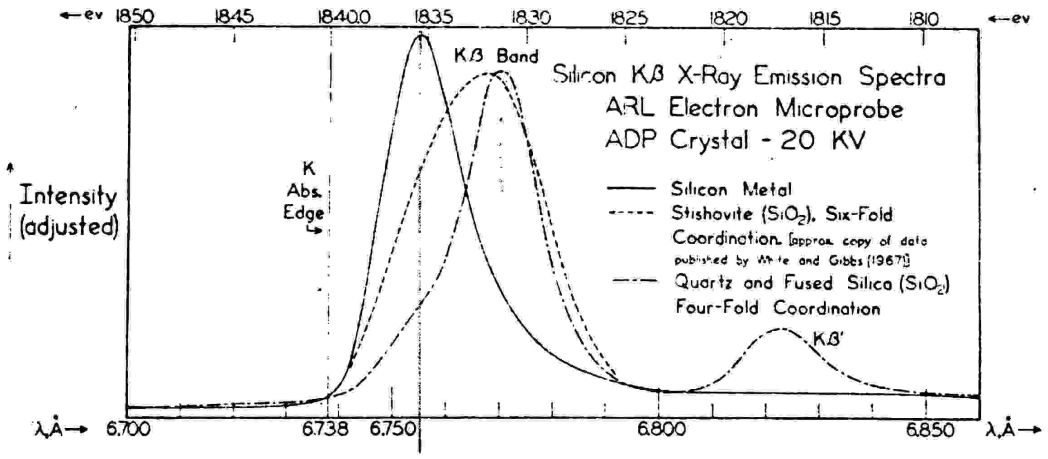

Figure 6.12: $K\beta-$bands for Si, measured with WDS [Dod68]

measured in the SiO_2 spectrum can be recognized in the TES spectrum.

So the TES chemical shift measurement is in good agreement with the WDS data although detector resolution is inferior to these systems. Thus TES EDS is able to determine chemical surroundings opening up many possibilities for new applications for this system.

6.4 Mapping and Linescan

The possibility of determining elemental distributions in one or two dimensions is an interesting and useful tool for the analysis of thin layers and small particles. The intensity distribution of a characteristic X-ray peak along a line scanned by the electron beam in a SEM is commonly called linescan. The two-dimensional distributional representation of a characteristic X-ray intensity is called element mapping. The spatial resolution of such a distribution is determined by the volume excited by the electron beam[5]. So for high-resolution mappings, for surface (or near-surface) mappings or linescans, low excitation voltages are preferred. TES detectors offer advantages for this application due to their high spectral resolution and excellent peak to background ratio. The background in EDS spectra consists mainly of bremsstrahlung. A good peak to background ratio is important because it is difficult to determine and subtract the background for each point that is scanned by the electron beam. The intensity of bremsstrahlung depends on the scanned

[5]see section 1.1

material. But position dependant differences in the intensity of bremsstrahlung can feign an elemental image. Bremsstrahlung can also hide small intensities from characteristic radiation. So a large peak to background ratio also improves the analysis results of linescans and mappings. A good energy resolution is desirable to avoid peak overlaps. If peaks can be distinguished clearly then the mappings of these peaks are unambiguous. Due to all the aforementioned advantages, TES detectors also offer the possibility of superior results for element mappings and linescans.

Most Si(Li) systems determine the position of the electron beam in the mapping or linescan by taking control over the electron beam of the SEM with the Si(Li) control electronics. The SEM is controlled with its own software which is integrated into the EDS control software. This software records mappings and linescans. In the Polaris EDS system the position of the electron beam is acquired by recording the signal of the SEM scan generator directly. The scan generator deflects the electron beam to scan, using the magnetic coils in the SEM column and it is controlled by the SEM software. The direct reading of the scan generator signal offers several advantages: The existing SEM software can be used and no additional SEM control in the EDS software is needed. The only required hardware is a link between the scan generator of the SEM and an ADC card to read the generator signal together with the detector signal.

A further advantage is that the SEM software is capable of achieving superior electron images with the application of different scanning filters and scan speeds. Thus a superior live image can be obtained during the EDS measurement, which in turn, allows real time SEM image drift correction. The SEM image will drift if the sample is charged by the electron beam, which is generally the case. The surface charge generates an electric field that deflects the beam leading to distortions in, and drifts of the SEM image. The drift can be detected in real time if the scan across the sample is sufficiently fast (image acquisition in the order of one second). This allows the operator of the system to correct the drift by shifting the beam back to its original position. Mappings over extended times can be completely automated with the use of automated drift correction.

The intensity of a characteristic X-ray line has to be determined as function of the electron beam position in order to calculate a mapping or a linescan. In typical element mappings the number of X-ray events per electron beam position is quite low so it is difficult to determine peak intensities without background. A region of interest (ROI) is a specified energy range typically of the magnitude of the detector FWHM and including a characteristic X-ray peak. During the element mapping all X-ray events with energies within the ROI are defined as belonging to the peak. The number of counts when plotted with respect to the electron beam position constitutes a mapping or linescan.

Putting it simply, a mapping or linescan is gained by scanning the electron beam across the sample and recording a spectrum from each point in the imaged area. In the integrated spectrum i.e. the spectrum from the whole scanned area, the peaks can easily be identified and the ROIs marked. A mapping of the ROIs can then be

calculated because for every X-ray event the corresponding position of the electron beam is known.

The ability to associate every X-ray pulse with a position of the electron beam during scanning also enables the selection of areas of interest in the map or line such as particles or thin layers. The spectra from these specific areas can then be post-calculated and elements can be identified that have low intensities and only occur in the areas. In the spectrum of the particular region of interest it is then also possible to quantify the elemental constitution.

In order to demonstrate the capabilities of TES mapping and linescan a test structure was used that consists of $2\mu\text{m} \cdot 2\mu\text{m}$ SiO_2 squares set in a W grid as shown in fig. 6.13. A linescan of such a structure is difficult to acquire with a Si(Li)

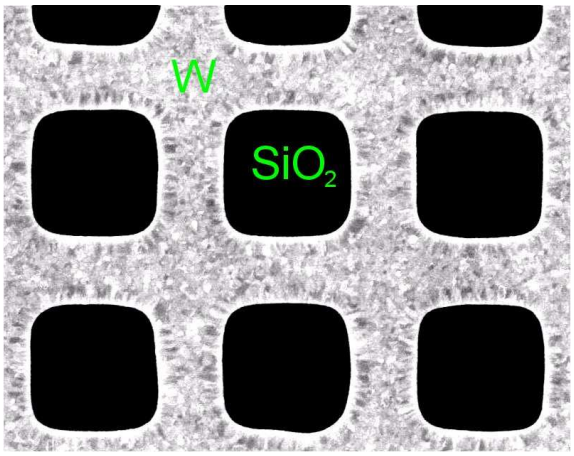

Figure 6.13: SEM image of teststructure

detector because the W Mα and Si Kα lines cannot be resolved[6]. The Si(Li) ROIs of these elements overlap because both ROIs are about 100 eV wide whereas they are only 35 eV apart. The plot of the Si(Li) linescan of this structure is shown in fig. 6.14. This linescan displays incorrect results and concludes that Si and W are distributed nearly homogeneously all over the sample. The apparent shape of the linescans of Si and W arises from two effects. One effect is that there is a small real linescan information because the Si ROI measures Si more efficiently than W. The other effect is that the *intensity* of the W M radiation in pure W is higher than the intensity of the Si K radiation in the SiO_2 area. This effect is measured by both ROIs. In the Si ROI these effects cancel each other and the intensity remains constant over the whole scan whereas in the W linescan the effects add and lead to a slightly larger intensity in the areas with W. A TES linescan however distinguishes the different elements clearly as shown in fig. 6.14b.

In the TES mapping of the test structure (fig. 6.15), the imaged structures are clearly separable (fig. 6.15) whereas in the Si(Li) mapping (fig. 6.16) the W and Si

[6]see section 6.1

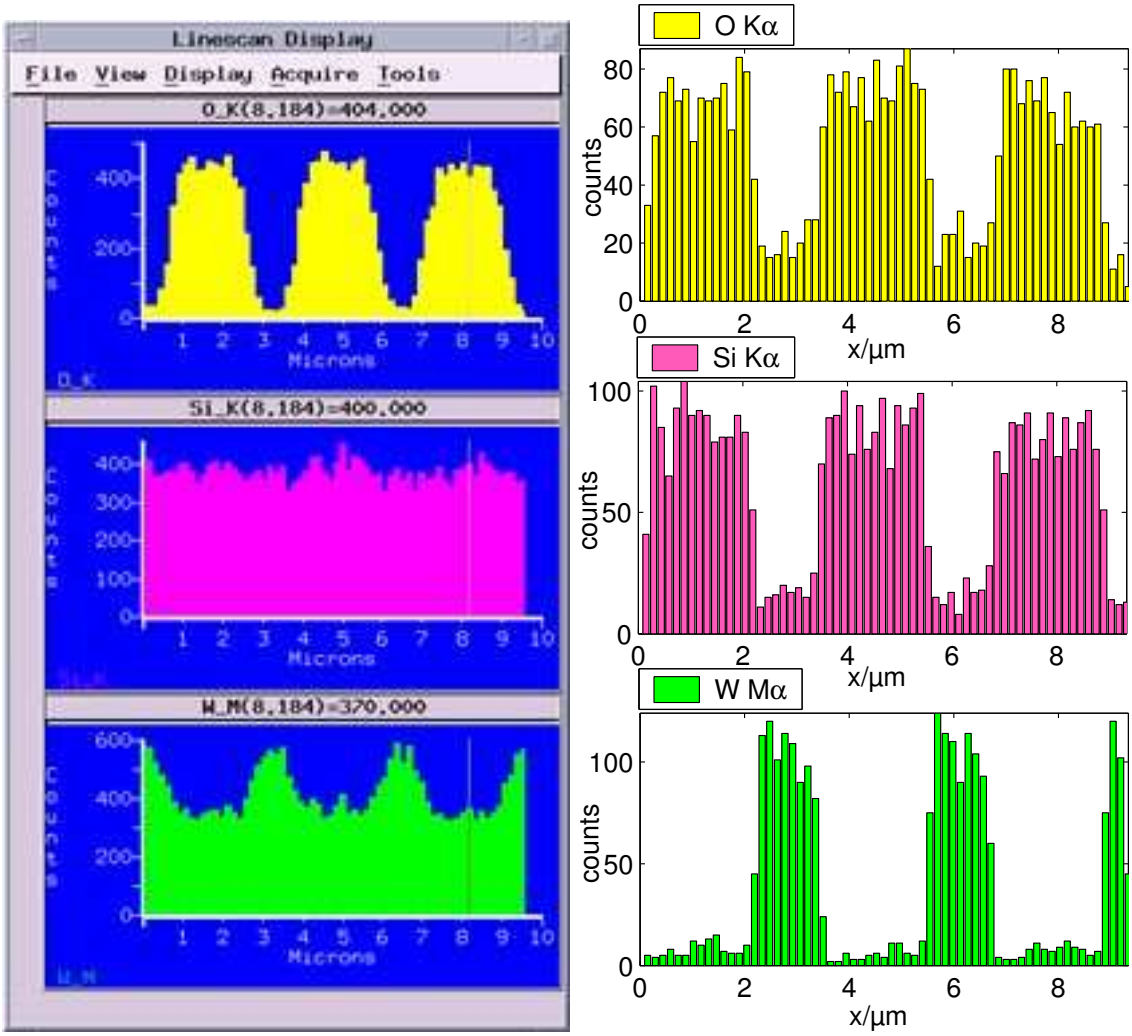

(a) Si(Li) Linescan

(b) TES Linescan, measurement time: 10min

Figure 6.14: Linescans of test structure, both measured at 4 kV acceleration voltage

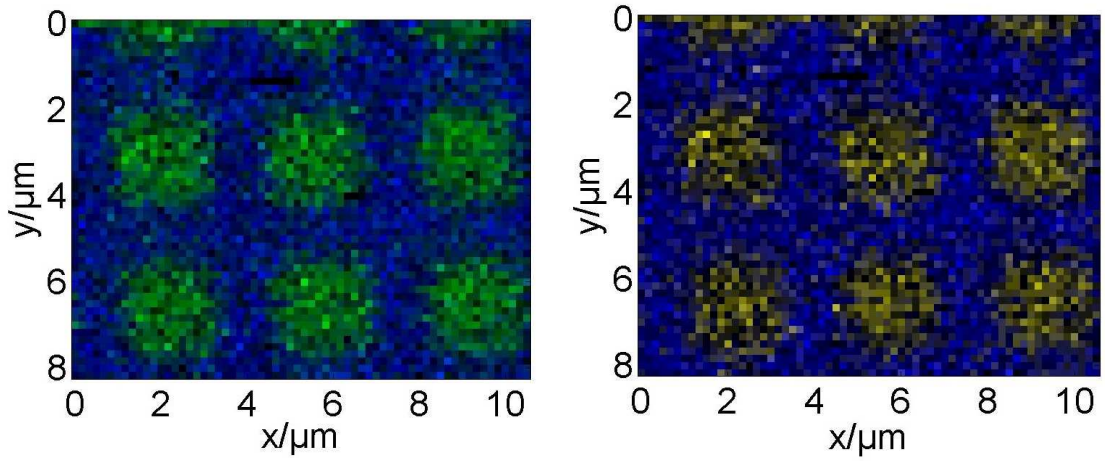

(a) Si/W mapping

(b) O/W mapping

Figure 6.15: TES mapping of teststructure (fig 6.13), blue=W, green=Si, yellow=O, measured at 5 kV

area are overlapping. The reason for the overlap is the same as in the linescan of

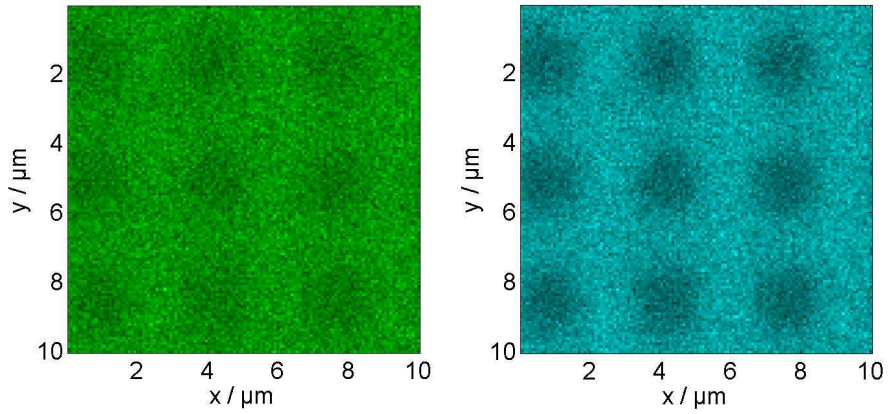

(a) Si mapping

(b) W mapping

Figure 6.16: Mapping of teststructure, measured with Si(Li) detector at 5 kV

this structure but due to a larger acceleration voltage (5 kV), the Si mapping shows a larger intensity in the W area than in the SiO_2 area, which is the opposite to what would be expected from an accurate mapping.

An example for the usefulness of linescans in failure analysis is seen in the determination of element distributions in so-called 'bumps'. Bumps are small solder balls used as a substitute for wire bonding. During thermal processing the metal bumps melt, form alloys and thus a solder bond. The composition of the alloys thus formed are of interest as they influence the soldering process. Fig. 6.17 shows a SEM image and a corresponding linescan along the cross-section of such an alloy stack. The low background and the sharp transition between the thicker layers is

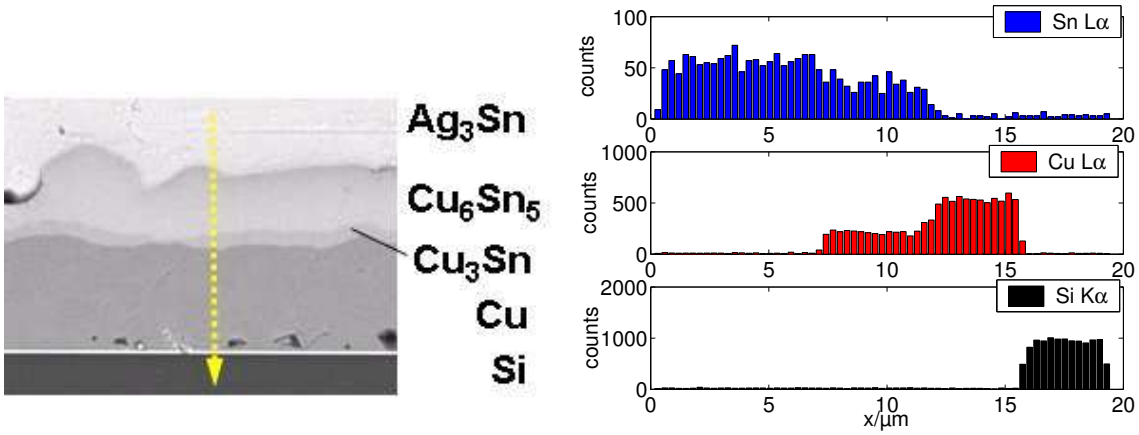

(a) SEM image of Bump cross section

(b) TES linescan

Figure 6.17: Bump measurement

especially noticeable in the TES linescan.

Element maps are useful to determine the structure and elemental distribution of particles and provide contrast to the surrounding matrix. This information can be used to find the origin of particles, therefore helping to avoid their formation. Fig. 6.18 shows a SEM-image of a defect in SiO_2 where a small residue of the material that caused a bubble has been remained on the lower right corner of the bubble (marked with black line). Si, C, O, P, W, Ga, Ti and F are found in the spectrum of the whole area, fig. 6.19 (blue line). Mappings of the whole area (fig. 6.20) show that the elements P, C, F, and O are relatively predominant in the residue in the bubble. A selected spectrum of the residue, fig. 6.19 (green line), shows a higher intensity of the X-ray radiation of these elements than the spectrum from the whole area. Identifying the elements in the residue, we can safely identify its source: The residue originates in the photo resist process. The bubbles were caused by the decomposition of the resist during the following BPSG deposition process.

Mappings and linescans are important methods in EDS analysis. These methods are realized for Polaris which shows analysis results superior to Si(Li) detector systems. The main advantages of TES mappings and linescans is an improved peak

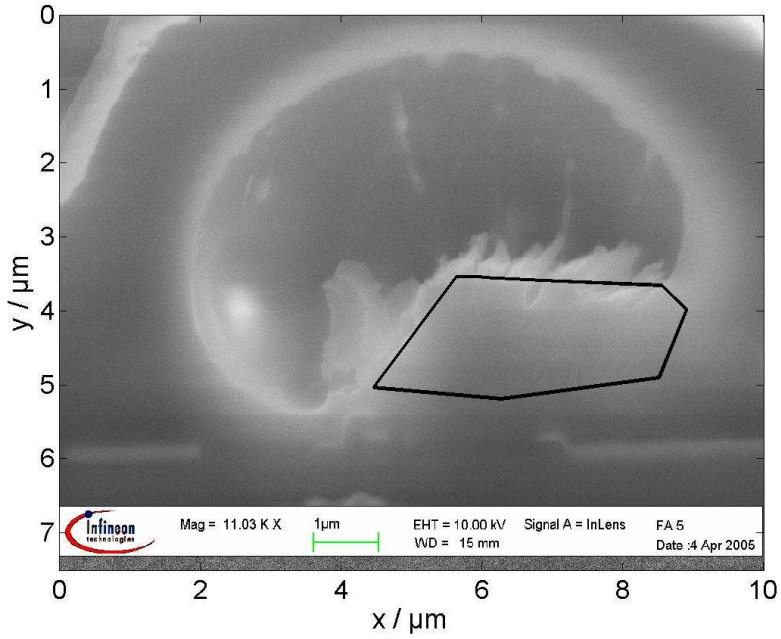

Figure 6.18: SEM image of bubble, black line marks residue

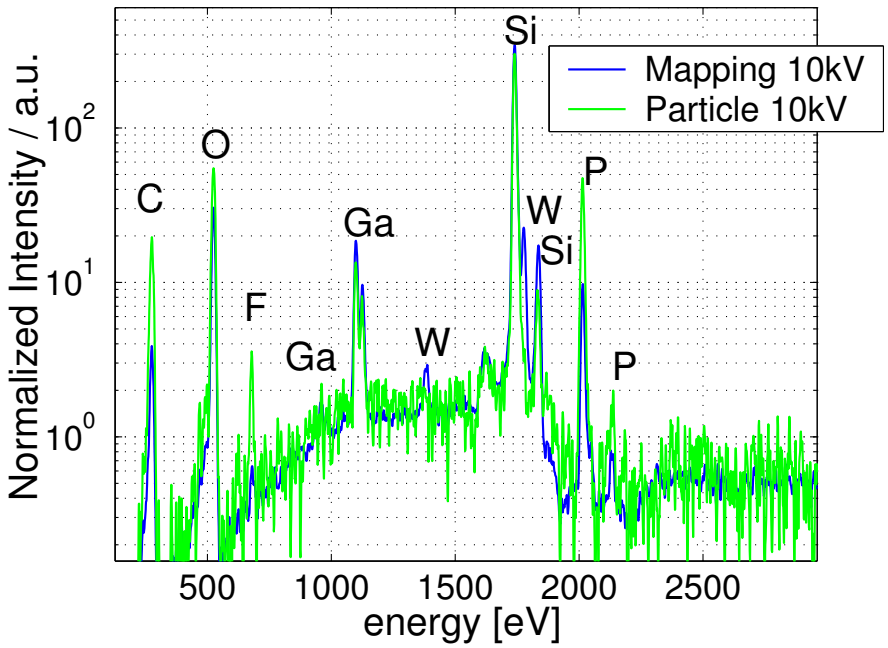

Figure 6.19: Spectrum of whole bubble (blue line) and of selected area in fig 6.18 (green line), acquired at 10 kV

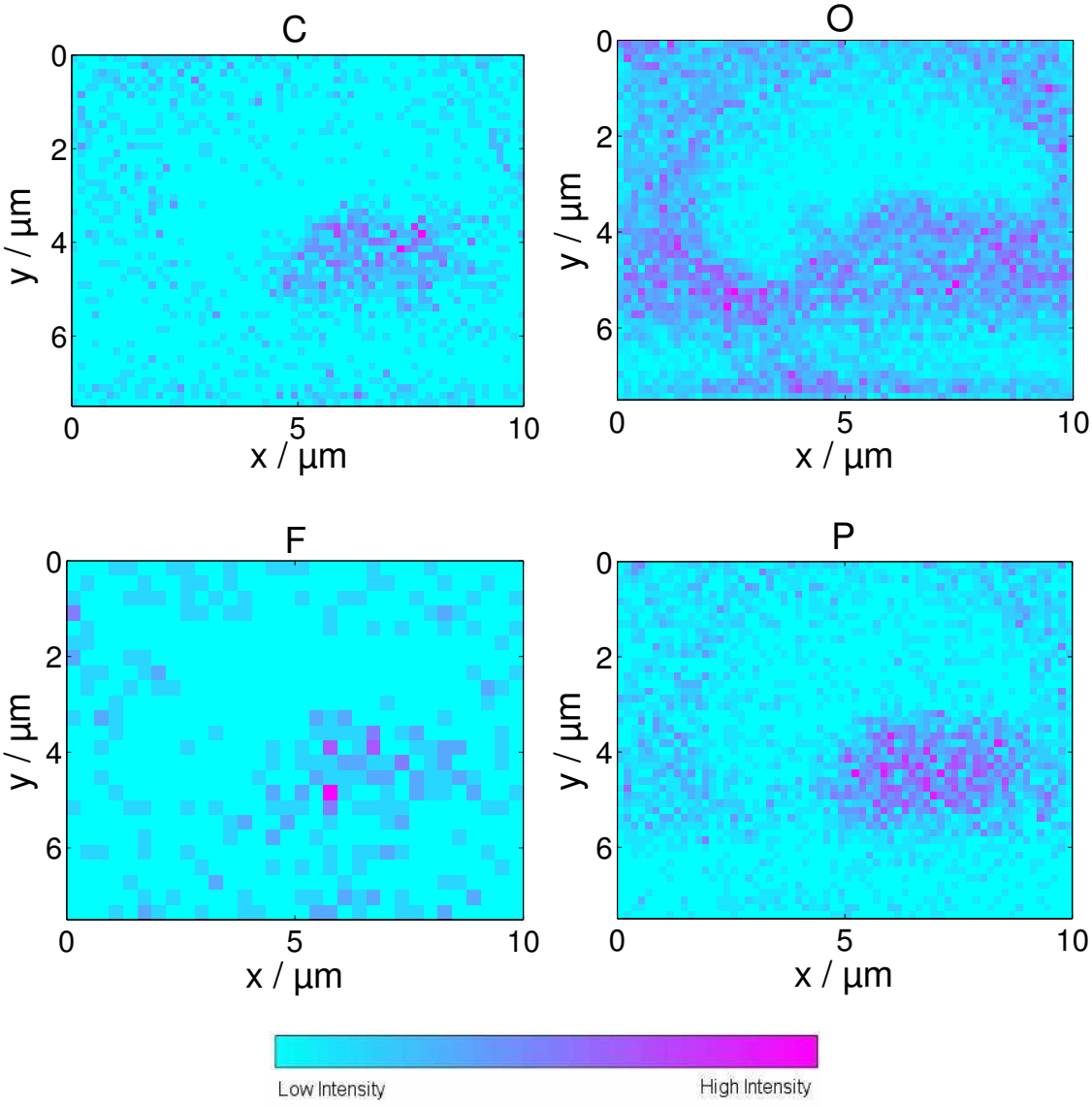

Figure 6.20: Mappings of different elements measured on the bubble

to background ratio and a better peak separation. The method used to acquire the electron beam position, developed during the work for this thesis, also offers advantages when compared with the conventional method of taking control over the electron beam.

6.5 Quantitative X-Ray Analysis

The determination of the constitution of a specimen is one of the main goals in material analysis. The EDS spectrum only displays the X-ray intensities of the elements in the specimen. But for many applications also the mass fractions of the elements identified by EDS have to be determined. The calculation of the mass fractions with help of an EDS spectrum is called electron probe quantitation.

6.5.1 Electron Probe Quantitation with Standards

In order to calculate the mass fractions of different elements, the interactions between primary electrons and specimen have to be taken into account (see chapter 1). A calculation of the dependency of the detected X-ray intensity (I) to the mass fraction (C_A) of a given element(A) leads to Eq. 1.13. If quantitation is done with Eq. 1.13, the detection efficiency $\epsilon_{det}(E)$ has to be determined. It depends on the detector windows, possible contaminations on these windows and the adjustment of the lens. A difficult problem for quantitative analysis with Eq. 1.13 is that some atomic constants such as the Coster-Kronig transition rates g_{ck} have to be known [Isa04]. But especially for M lines these constants are not known with sufficient accuracy. As in TES measurements with low excitation voltages only M lines of heavy elements are excited, quantitative analysis of heavy elements can not be done with Eq. 1.13. To avoid this problem standards with a known composition can be used. They have to be measured under the same experimental conditions as the sample that has to be quantified. If the intensities of standard and unknown sample are divided by each other, most of the constants in Eq. 1.13 are reduced. This ratio is called k-ratio [Cas60]:

$$k_i = \frac{I_{i,meas}}{I^{std}_{i,meas}} = \frac{C_i \cdot \int_0^{R_x} \Phi_i^{sample}(\rho z) \cdot exp(-\chi_i \cdot (\rho z)) \cdot d(\rho z)}{C_i^{std} \cdot \int_0^{R_{x,std}} \Phi_i^{std}(\rho z) \cdot exp(-\chi_i^{std} \cdot (\rho z)) \cdot d(\rho z)} \tag{6.3}$$

The k-ratio k_i in Eq. 6.3 can be calculated as function of the mass fractions of all elements C_i and measured as ratio of intensities of a standard and the unknown sample. As the intensity depends on the mass fractions of all elements present in the sample, standards for all constituents have to be measured leading to a system of equations that has to be solved iteratively.

6.5.2 Detection Efficiency of Polaris TES EDS System

The determination of the energy dependant detection efficiency $\epsilon_{det}(E)$ is important for standardless quantitative analysis and also for quantitative analysis with a standard database[7]. Energy dependant X-ray absorption occurs in the lens, the window system and in the detector itself. The setup of the detector windows is shown in

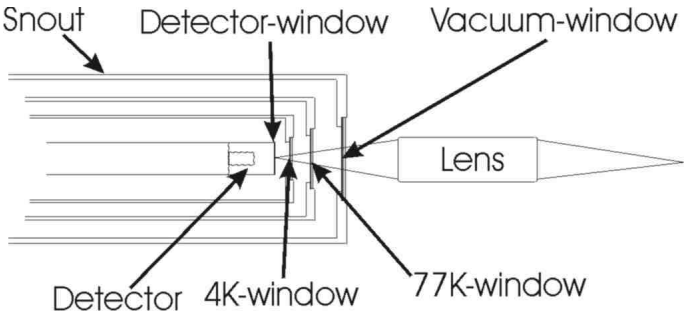

Figure 6.21: Snout of Polaris with windows and lens

fig. 6.21. The inner windows are necessary to protect the detector from infrared radiation. They consist of a parylene layer (C_8H_8) coated with a thin Al layer. The vacuum window also consists of an Al coated parylene film but is supported by a Si grid to withstand air pressure when the snout is not in the vacuum of the SEM chamber, or when the chamber is vented to allow sample exchange. The lens is used to increase the detected X-ray intensity and is described in detail in chapter 5.3. The lens manufacturer's specifications can be used to calculate the detector efficiency. The absorber of the detector, consisting of 500 nm gold, is too thin to absorb all X-rays, especially at higher energies. So the detector itself also contributes to the detection efficiency of the system. Regarding all of these contributions, ϵ_{det} can be calculated with:

$$\epsilon_{det} = T_{det} \cdot T_{4K} \cdot T_{70K} \cdot T_{Vak} \cdot T_{lens} \cdot A_{det}$$

T_i is transmission of a specific window whereas A_{det} is the absorption of the detector. The calculation of the transmission properties of windows, lens and absorber of the detector leads to an efficiency as shown in fig. 6.22.

The detection efficiency can only be calculated if the composition and thicknesses of all windows and the transmission properties of the polycapillary lens are known with sufficient accuracy and no additional absorption contributes to the detection efficiency. But if the vacuum in the detector dewar is not perfect, thin films of condensed air or water can be deposited onto the inner windows which leads to additional absorption. Another contributing effect is that the detector size can be smaller than the spot size of the lens. So the outer areas of the focal spot of the lens are not detected. The lens also exhibits chromatic effects: the size of the focus

[7] see subsection 6.5.4

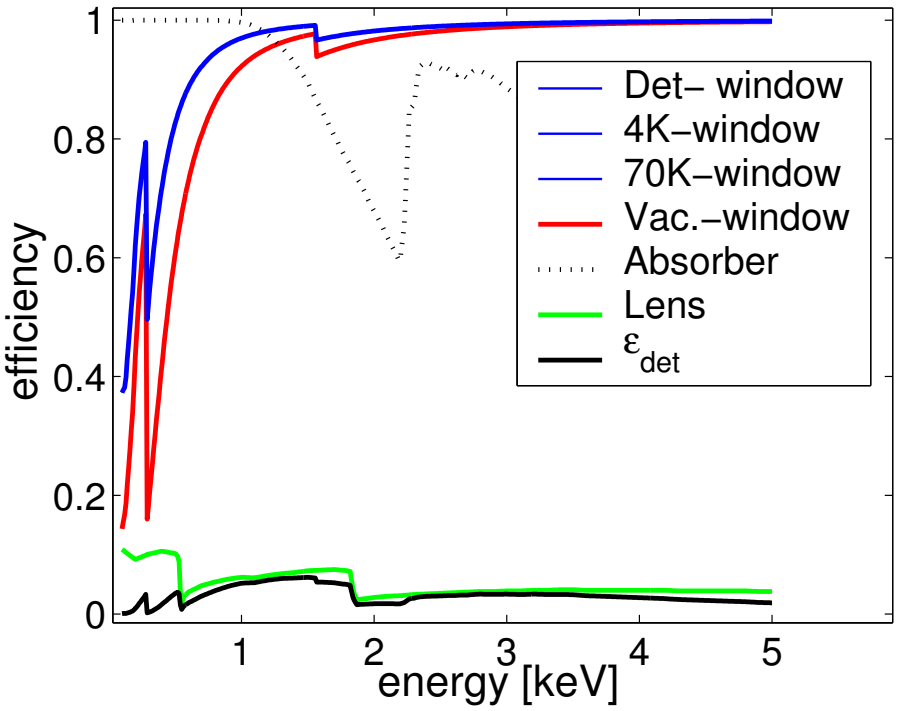

Figure 6.22: Calculation of detection efficiency of Polaris TES-EDS system.

is energy dependant[8]. This leads to a position and alignment dependant lens transmission function and thus affects the overall detection efficiency. Small deviations of the optimum lens adjustment cause changes in the lens transmission (see section 5.3.3). Additionally, window layer thicknesses can deviate from manufacturer specifications changing the window absorption. Due to these possible errors in the calculation of the detection efficiency, it is necessary to check the validity of the calculated detection efficiency experimentally.

The detection efficiency is the ratio of the measured intensity to the incident intensity, $\epsilon_{det}(E) = I_{meas}/I_{incident}$. To determine this ratio for a wide energy range the intensity of bremsstrahlung is used. The incident intensity can be calculated by Monte-Carlo simulations [Joy95] or with help of Si(Li) spectra. For the determination of the detector efficiency of the Polaris, Si(Li) spectra were used. The detection efficiency of Si(Li) detectors is known accurately (see fig. 1.11, [Isa04]) and so the incident intensity can also be determined accurately, $I_{incident} = I_{Si(Li)}/\epsilon_{Si(Li)}$. The TES detection efficiency measured at different elemental lines is plotted in fig. 6.23. In fig. 6.23 the measurements at different element lines have been normalized with an energy independent factor to fit to the maximum of the calculated detection efficiency. This is necessary because the number of incident electrons in the TES and also in the Si(Li) measurement is not exactly known. A knowledge of this factor is,

[8] see fig. 5.11

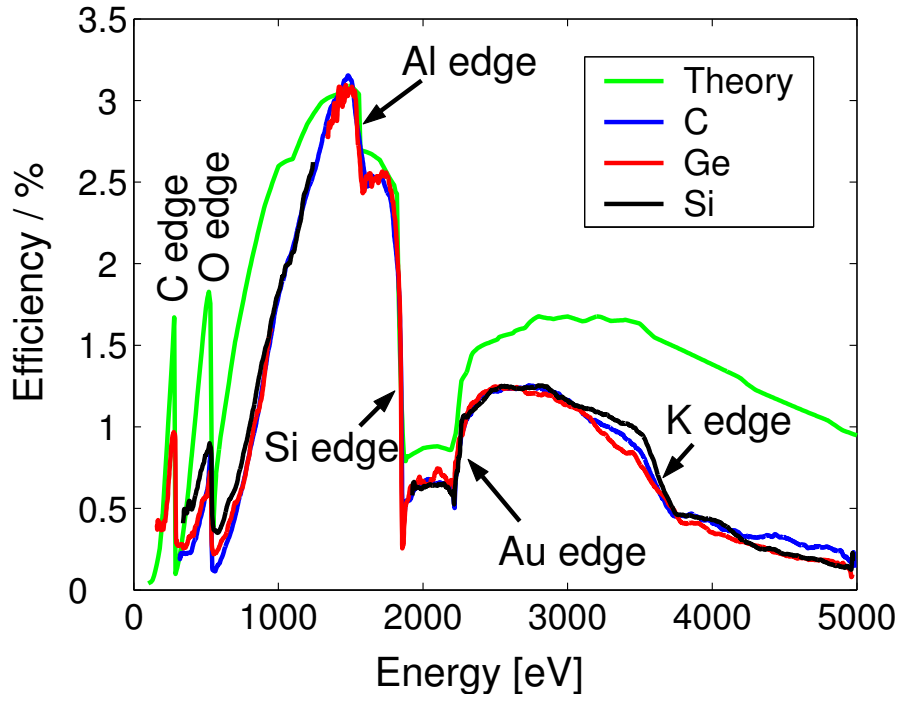

Figure 6.23: Comparison between calculated and measured detection efficiency

however, not necessary for standardless measurements because only the ratio of the detection efficiencies at different energies has to be known because the sum of the mass fractions can be normalized to 100 %.

The normalized measurements at different element lines in fig. 6.23 show very similar results and clearly deviate from the calculated detection efficiency. It can be concluded for the used Polaris system that it is necessary to determine the detection efficiency experimentally in order to use it for standardless quantitative analysis or for the quantitation with an element standard database[9].

6.5.3 Examples for Quantitative Analysis

Quantitative analysis can be done with the Polaris EDS system using the equations described in 6.5.1 [Isa04]. It is possible to quantify with standards or standardless.

Equal measurement conditions for sample and standards are very important for quantitation with standards. These conditions include time, beam current, acceleration voltage and lens adjustment. The takeoff angle Ψ and the solid angle Ω are similar for all samples and standards because they are fixed by the geometry of the system. For standardless quantitation it is necessary to determine $\epsilon_{det}(E)$ (see last subsection). The method is limited to K and L lines because atomic constants such

[9] see subsection 6.5.4

as Coster-Kronig transition probabilities are not known with sufficient accuracy for M lines.

The first example presented for electron probe quantitation with standards is WSi_2. As already mentioned in section 6.1 the elements W and Si are common materials in semiconductor industry. Si Kα and W Mα are separated by 35 eV and can not be correctly quantified by Si(Li) detectors. The stoichiometry of WSi_2 leads to mass fractions of 0.766 for W and 0.234 for Si. A quantitation with a Si(Li) detector results in 0.156 ± 0.007 for Si and 0.844 ± 0.020 for W in a measurement with 5 kV acceleration voltage. Fig. 6.24 shows a TES spectrum of WSi_2 with corresponding

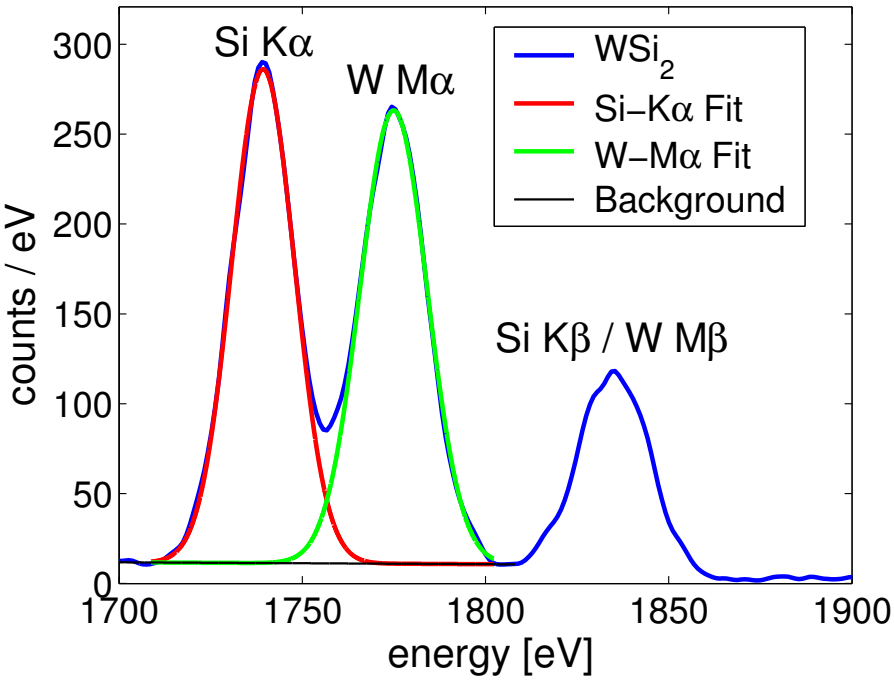

Figure 6.24: TES spectrum and concurrent peak fits of WSi_2, measured with 5 kV

gaussian fits to determine the peak intensities. Elemental Si and W are chosen as standards. The peak intensities of the standards were determined in the same way as for the quantitation sample. WSi_2 and the standards are measured at three different acceleration voltages to check if the quantitation result is independent of acceleration voltage. The results, shown in table 6.1, are in accordance with the result of the calculation with stoichiometry whereas the quantitation with a Si(Li) detector clearly deviates from this result. The errors in the TES quantitation arise mainly in the statistical uncertainties during determination of the intensities.

Another example for quantitation is Si doped with P (section 6.2). The mass fraction of P is $8.8 \cdot 10^{-4}$ according to the specification of the manufacturer. In contrast to the previous example, where mass fractions were of the same order, the mass fraction of P is extremely small. Fig. 6.25 shows the measured spectrum. GaP

	C(Si)	C(W)
5 kV	$0.22 \pm 8\%$	$0.78 \pm 2\%$
7.5 kV	$0.22 \pm 8\%$	$0.78 \pm 2\%$
10 kV	$0.23 \pm 9\%$	$0.77 \pm 2\%$

Table 6.1: Quantified mass fractions of W and Si in WSi_2, errors are relative errors

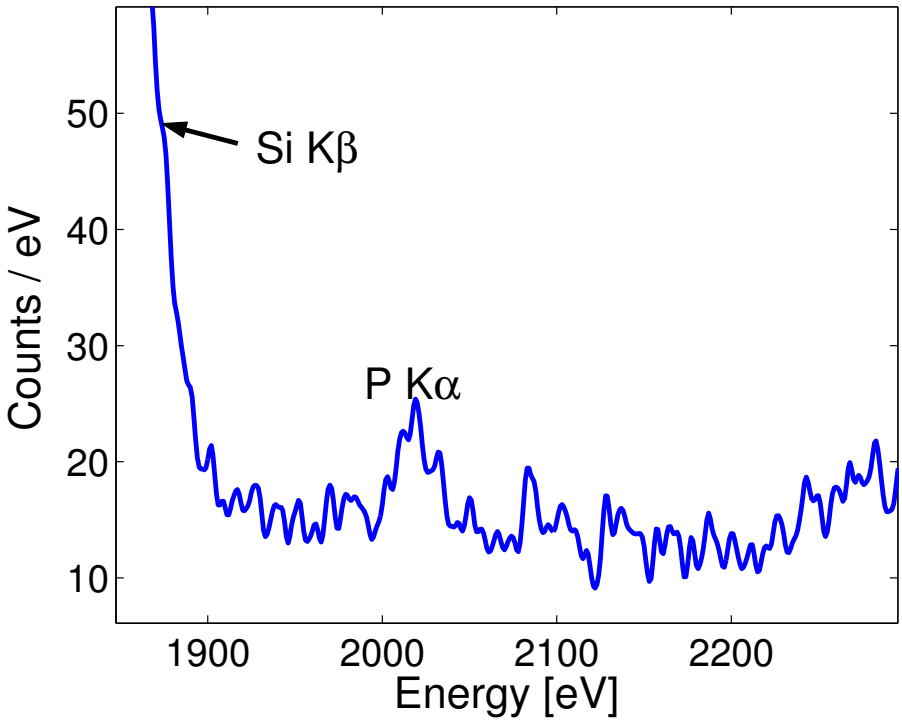

Figure 6.25: Si doped with P, measured with 10 kV

served as the standard for the quantitation of P. The Si was, for the calculation, assumed to be pure. This is a valid approximation because the deviation is much smaller than the statistical error in the measurement of the peak intensity. The resulting error for quantitation can be neglected. The quantification of this sample results in $9.2 \cdot 10^{-4} \pm 13.6$ %. The error results from the fairly low number of X-ray events in the P peak and also from uncertainties in the determination of the bremsstrahlung. Considering this error, the result is in good agreement with the specification, $8.8 \cdot 10^{-4}$. Quantitation of such low concentrations is impossible for Si(Li) detectors because the P peak is not detectable (see subsection 6.2).

Si and P are light elements emitting only X-ray K radiation. So electron probe quantitation can also be done standardless for this material because for K lines all atomic constants are fairly well known. To perform standardless quantitation the detection efficiency has to be measured as described in subsection 6.5.2. The intensity ratio of Si to P in the quantitation measurement is $1.63 \cdot 10^{-4} \pm 3 \cdot 10^{-5}$. With Eq. 1.13 a mass fraction of $1.07 \cdot 10^{-3} \pm 2 \cdot 10^{-4}$ can be determined for P. This value is in good agreement with the specified value of the wafer manufacturer, namely $8.8 \cdot 10^{-4}$. The error results from statistical uncertainties in intensity determination and also from uncertainties in the measurement of the detection efficiency.

6.5.4 Quantitation with a Standard Database

For an easy-to-use EDS system it is necessary to get fast results for quantitative analysis. If low acceleration voltages are used only the M lines of heavy elements are excited. Only these M lines can then be used for quantitative analysis. As standardless quantitative analysis is not accurate for M lines[10], it is necessary to use element standards for quantitation. To avoid the measurement of element standards for each quantitative analysis it is useful to create a database of standards once. Such a database allows the automation of the quantitation process.

For the measurement of the standard database it is important to have similar conditions for the various element standards. A deviation in the intensity ratio of one element standard to another leads to an proportional error in the quantitative analysis result. Experimental conditions such as the adjustment of the lens with respect to sample have to be adjusted very carefully. Variations of other parameters such as detection efficiency, deadtime[11], sample current and measurement time can be corrected as described in the following paragraphs.

For the measurement of the standard database it is necessary to optimize the lens adjustment carefully towards the beam of the SEM on the sample. The deviation of the focal spot from the beam-sample intersection point has to be lower than 10 μm to get an acceptable accuracy in the intensity measurement (error <4 % for 1500 eV). If the distance is too large the transmitted intensity decreases because the spatial transmission function of the lens has a gaussian shape as shown in fig. 6.26.

[10] see subsection 6.5.1

[11] see Eq. 6.4

Therefore a method is needed to achieve this accuracy in lens adjustment. A direct search of the transmission maximum is difficult because near the maximum of the distribution the statistical fluctuations in the count rate exceed the decrease in count rate near the maximum. So adjustment points are searched around the supposed maximum with about half of the maximum intensity. It is necessary that these points have similar count rates as shown in fig. 6.26. These points then define a

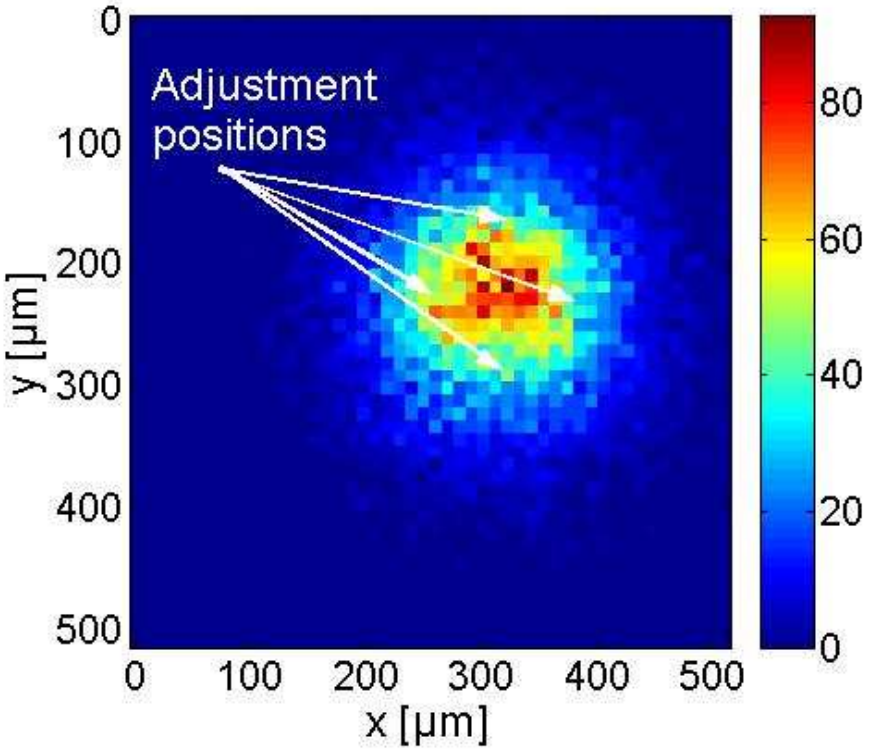

Figure 6.26: Lens transmission vs electron beam position for Al Kα with adjustment positions marked

circle and the maximum of the intensity distribution is at its center. This method is more sensitive than trying to determine the count rate maximum directly because on the edge of the gaussian distribution (fig. 6.26) the dependancy of the count rate on the beam position is much more sensitive than at the middle of the distribution. This is the case because the derivative of count rate with respect to position is much larger on the edge of the lens focus than at its center. With this method an accuracy better than 10 μm between focal center and beam-sample intersection point can be achieved for every standard in a quite short time.

Because the number of needed standards is quite large, the acquisition of the standards database has to be done over several recharge cycles of the ADR[12]. During

[12]see section 2.2

the recharge cycle the position of the detector in the snout can be changed slightly because the strong magnetic fields necessary for the recharge generate large forces on the ADR salt pill. This can lead to a small misadjustment of the detector in relation to the lens and therefore to slight changes in the amplification gain of the lens and also the energy dependency of the lens transmission. The resulting change in gain can be determined and corrected by measuring the count rate of a specified element standard after every recharge cycle. An intensity correction factor c_{cr} is determined by comparing the measured intensity to a reference. The change of the energy dependency cannot be corrected easily because a background measurement would be necessary as described in 6.5.2. A background measurement, however, takes quite a long time, consuming most of the hold time of the ADR. Fortunately, only at X-ray energies above 3 keV do deviations in detection efficiency of more than a few percent occur. So this effect can be neglected for energies below 3 keV. As almost every element has an X-ray line below 3 keV, only these lines are used for quantitation to avoid an error due to deviations in detection efficiency.

All actual intensities are stored in a database and normalized for ease of computability. This can be done by multiplying the intensity of the measured standard with the ratio of the calculated intensity (I_{pure}) of a pure element standard to the calculated intensity in the given standard $I_{pure}/I_{standard}$. This is only a mathematical conversion and produces no additional error.

The intensity of characteristic X-ray radiation is a function of the acceleration voltages of the electron beam. So it seems to be necessary to measure the standard of every interesting element with various acceleration voltages. But the calculation of this function shows a satisfying agreement with the measurement as shown in fig. 6.27. It is sufficient, then, to measure the standard database with one acceleration voltage per element standard and to consider the dependency on acceleration voltage in a post-calculation.

Another effect that has to be corrected is detector dead time. This is the time during which the detector is not able to measure X-ray events. In the TES detector system an X-ray event may have to be rejected if it follows a very short time after the previous event. The discriminated X-rays do not contribute to the detected intensity. This discrimination causes the dead time. Dead time can be calculated with:

$$t_{dead} = t_{total} \cdot \frac{N_{disc}}{N_{total}} \tag{6.4}$$

where t_{total} is the total measurement time, N_{total} the number of total counts and N_{disc} the number of discriminated counts. All measured intensities in the database have to be normalized to equal live times to avoid errors in the intensity ratio of different standards.

The intensity also has to be normalized to the beam current I_{beam} of the electron beam and the total measurement time. So the total intensity $I_{A,l}$ of element A and X-ray line l is given by:

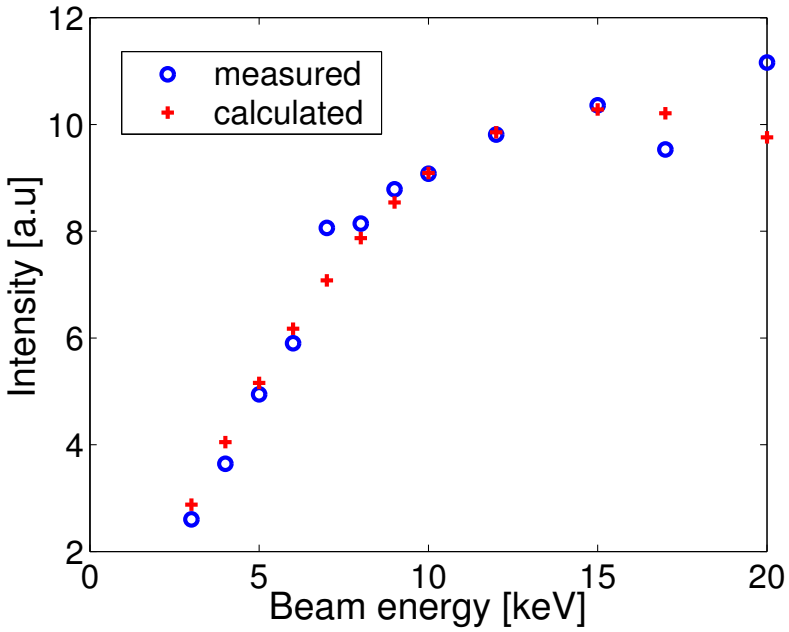

(a) Intensity of C Kα vs. beam energy

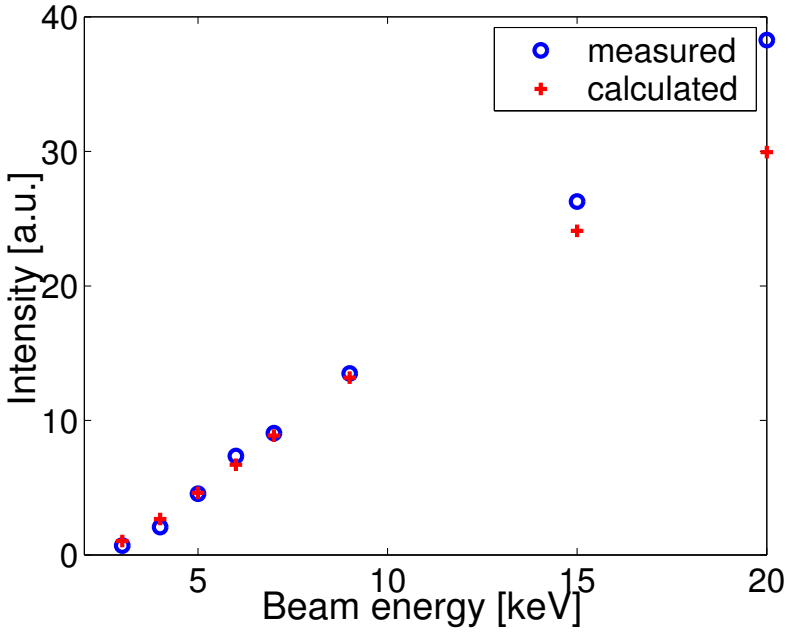

(b) Intensity of W Mα vs. beam energy

Figure 6.27: Comparison of measured and calculated intensities for a low and a high Z material

$$I_{A,l} = N_{A,l} \cdot \frac{I_{pure,calc}}{I_{standard,calc}} \cdot c_{cr} \cdot \frac{N_{total}}{N_{total} - N_{disc}} \cdot \frac{1}{t_{total} \cdot I_{beam}} \tag{6.5}$$

To use the database it is also important that the energy dependence of the detection efficiency can change due to several reasons such as warming up and cooling down the system or a replacement of the detector. It could become necessary to calculate the ratio of the detection efficiency during the measurement of the database to the new detection efficiency and correct the database with this ratio.

The accuracy of the current database is still unsatisfactory due to deviations in measurements from different standards. The best accuracy could be achieved with a TES detector system without X-ray lens as the lens causes most of the problems in the measurement of the database. The lens could be added in calculation afterwards by the determination of the ratio between background spectra with and without lens. The precondition for the measurement of a database without lens is a SEM with a sufficient beam current to allow measurements with satisfactory count rate for the measurements of the standards and also for the background.

6.6 Thickness Determination of Thin Surface Layers

Electron probe quantitation is a method to determine mass fractions of elements distributed homogeneously in a sample. But the method can also be extended to determine the thicknesses of thin surface layer systems with known mass fractions [Isa04].

Fig. 6.28 shows the depth distribution function Φ. The mass depth of the surface layer is R_f. Φ can be approximated with the surface ionization Φ_0 within the whole layer. Φ_0 is defined as the ratio of the intensity of a thin surface layer on a bulk material to the intensity of the same thin layer without bulk material. The value is always greater than 1 because electrons are backscattered from the bulk in the surface layer leading to additional ionization. The number of backscattered electrons is mainly determined by the bulk material. Thus, in order to calculate the mass layer thickness R_f it is assumed that the surface ionization Φ_0 can be calculated for the bulk material without consideration of the surface layer. This approximation is valid as long as the surface layer is much thinner than the penetration depth of the electrons. The intensity of an element which is only present in the surface layer is determined by [Pou91]:

$$\begin{aligned} I_f &\propto \int_0^{R_f} \Phi_{bulk}(\rho z) \cdot exp[-\chi_A \cdot (\rho z)] \cdot d(\rho z) \sim R_f \cdot \Phi_{0,bulk} \\ \Phi_0 &= 1 + 3.3 \cdot [1 - U_0^{2.3\eta-2}] \cdot \eta^{1.2} \\ \eta &= 1.75 \cdot 10^{-3} \overline{Z}_b + 0.37 \cdot [1 - exp(-0.015 \cdot \overline{Z}_b^{1.3})] \end{aligned}$$

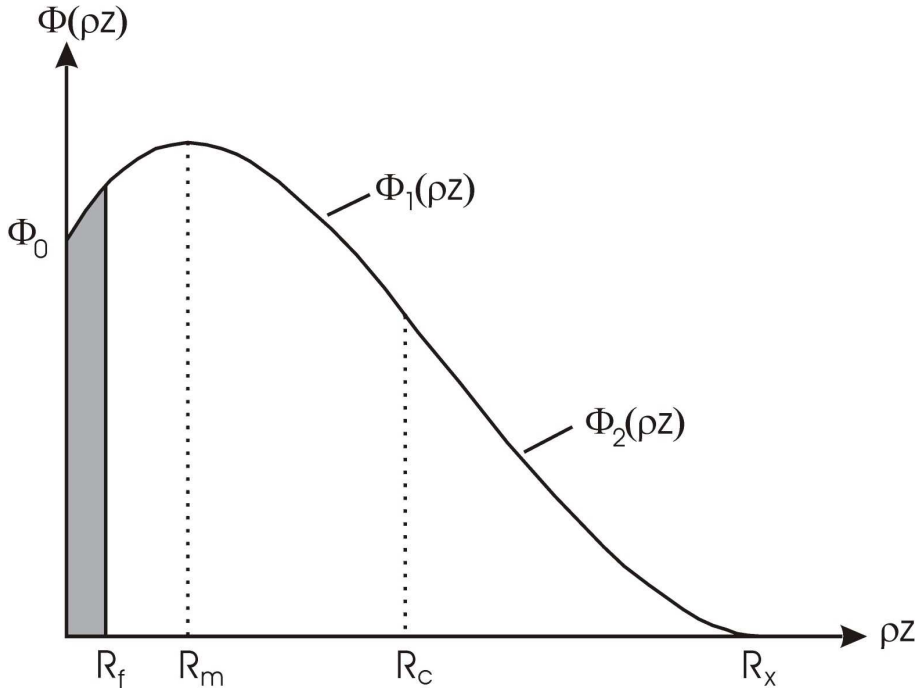

Figure 6.28: Depth distribution function Φ with surface layer (gray)

$$\overline{Z}_b = (\sum_i c_i \cdot \sqrt{Z_i})^2$$
$$U_0 = \frac{E_{beam}}{E_{X-ray}}$$

where E_{X-ray} is the critical excitation energy and E_{beam} is the beam energy. Fig. 6.29 shows Φ_0 in dependancy of $\overline{Z}_b$ for an overvoltage $U_0 = 8$. Using a standard, the constants in Eq. 1.13 can be reduced, leading to the following k-ratio:

$$k_A = \frac{c_A \cdot R_f \cdot \Phi_{0,bulk}}{c_A^{std} \cdot \int_0^{R_x^{std}} \Phi^{std}(\rho z) \cdot exp[-\chi_A^{std} \cdot (\rho z)] \cdot d(\rho z)} = \frac{I_{meas,sample}}{I_{meas,std}} \qquad (6.6)$$

If the mass fractions are known, the mass depth R_f can be calculated with Eq. 6.6. An example where thickness determination can be very useful is the gate oxide of a MOS transistor. The thickness of the SiO_2 layer on the Si substrate was determined with an ellipsometer to be $7.7 \pm 0.4\,\mathrm{nm}$ (UV Tencor). As standard for the thickness determination Al_2SiO_5 was used. the beam energy is 4 keV leading to an overvoltage of 7.6 for the O Kα line at 525 eV. Fig. 6.30 shows the spectra of the element standard and of the layer system. The red line marks the background of the O peak. In this example the background is quite difficult to determine as the energy of the O Kα peak is right below the O K absorption edge. Because of this edge the background has to be extrapolated from the low-energy side of the peak. With

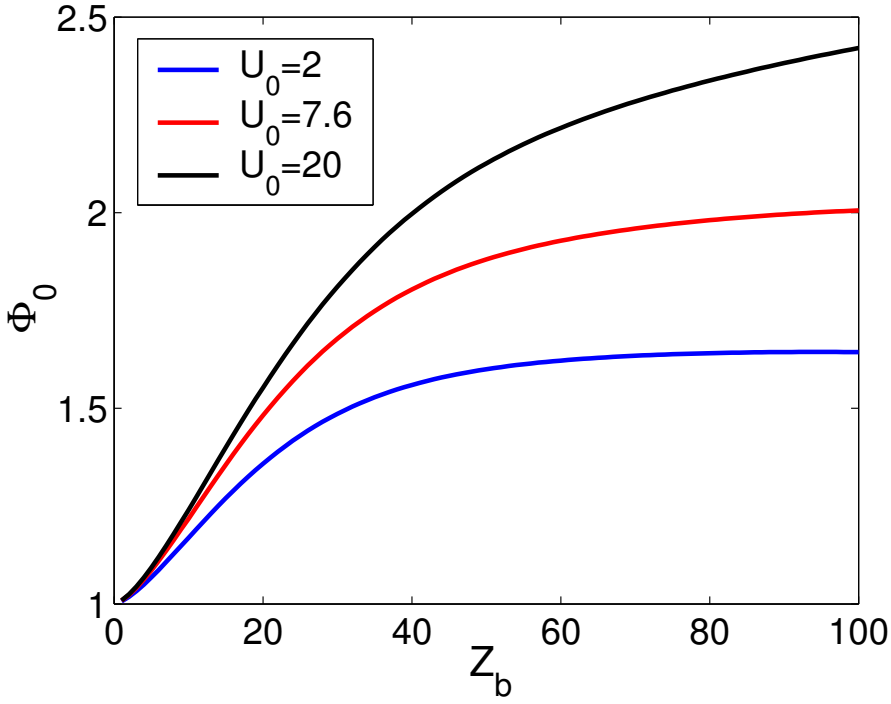

Figure 6.29: Surface ionization Φ_0 in dependency of mean atomic number $\overline{Z}_b$ for different overvoltages U_0

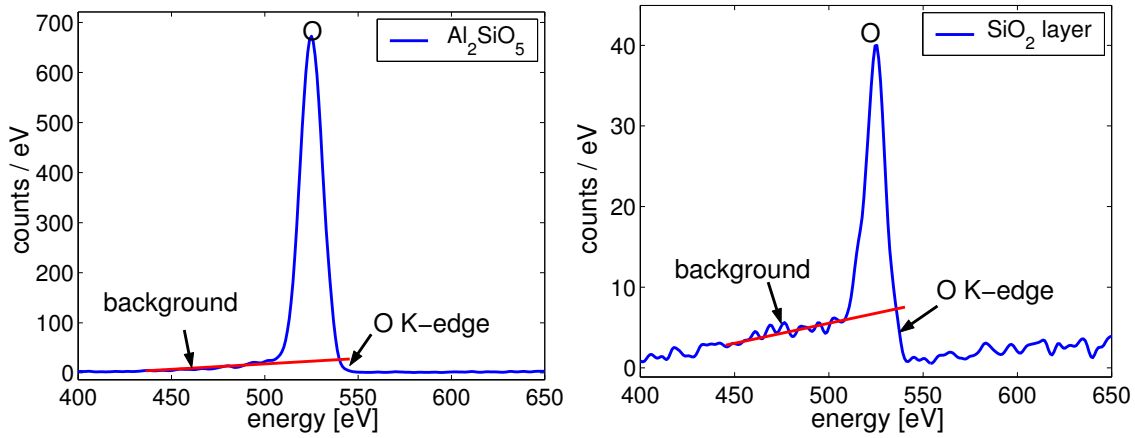

(a) Spectrum of standard

(b) Spectrum of layer system

Figure 6.30: O Kα of standard and SiO/Si layer system with a beam energy of 4 kV, measurement time: 2000 s

the marked backgrounds, the intensities were determined to be 395 ± 17 counts for the surface layer and 9500 ± 197 counts for the Al_2SiO_5 standard. This leads to a geometrical layer thickness of 8.1 ± 0.7 nm. So the result is within the error of the ellipsometer measurement of 7.7 ± 0.4 nm. The error in the EDS measurement is mainly statistical because the measured O Kα intensity of the layer is quite low.

This measurement was repeated with 2 keV beam energy to increase the peak to background ratio for the O Kα line - the penetration depth of the electrons decreases with decreasing beam energy. The result of the measurement is shown in fig. 6.31.

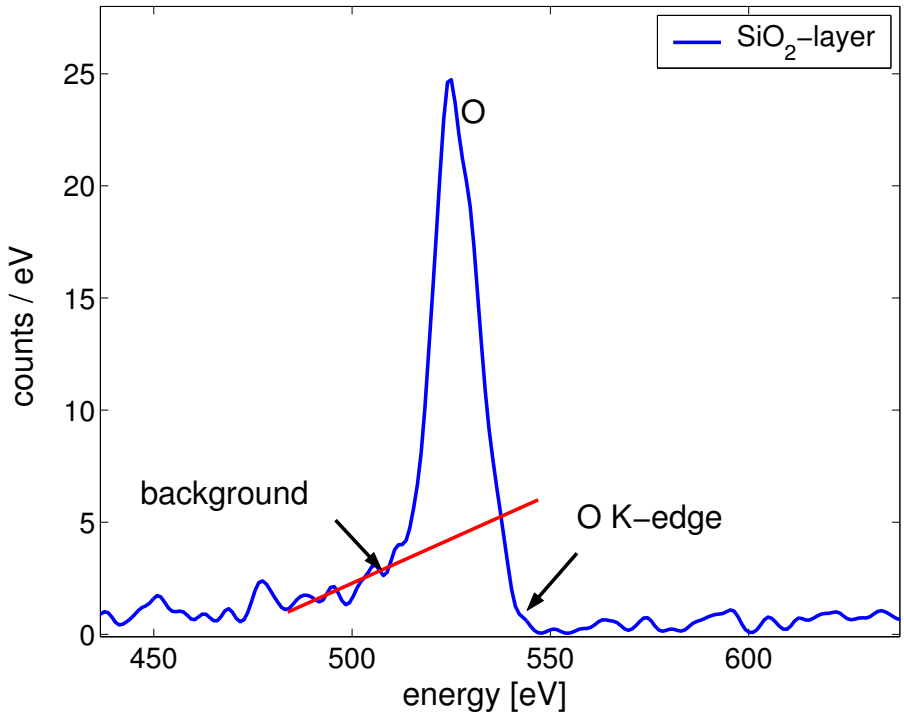

Figure 6.31: O $-$ Kα of the SiO_2/Si layer system measured with 2 keV beam energy

The k-ratio for this measurement was determined to be 0.165 ± 0.023 resulting in a layer thickness of 8.6 ± 1.2 nm. The larger deviation compared to the measurement with 4 kV can be explained with a bigger statistical error due to a decrease in count rate.

For this method it has to be presumed that the thickness of the surface layer is much lower than the penetration depth of the electrons and that the elemental mass fractions in surface layer and bulk are known. This method has the ability to deliver good results for thickness determination of thin layers and is thus suitable for various applications in thin-film technology.

Chapter 7

Summary and Outlook

Energy dispersive X-ray spectroscopy (EDS) is the measurement of X-rays generated when an electron beam impinges on a sample. In combination with scanning electron microscopes (SEMs) EDS is an important method for determining elemental constitutions of volumes with sizes less than one micrometer. The energy spectrum of the X-rays includes the characteristic radiation from the elements in the specimen and therefore allows their identification. Typically, semiconducting detectors such as lithium-drifted silicon detectors are used for EDS. These detectors are fast and easy-to-use but the energy resolution is unsatisfactory for many contemporary applications. With the application of high-resolution, low-temperature detectors such as transition edge sensors (TES) this disadvantage can be overcome. The TES is a calorimetric detector that determines the energy of X-rays by measuring the heat deposited by an impingent X-ray in a small metallic absorber. The temperature rise caused by the absorption is measured with a superconducting phase transition thermometer. The resistance of such a thermometer is in its phase transition very sensitive to small temperature changes and allows a very accurate measurement of the X-ray energy.

In this thesis the introduction and improvement of a fully automated TES-EDS detector system in the industrial environment of a failure analysis lab is described. The detector is cooled by a mechanical pulse tube cooler in combination with an adiabatic demagnetization refrigerator (ADR). The application of a mechanical cooler has the advantage of cryogen-free operation and a comparatively low weight. The vibrational influence caused by this cooler on the SEM could be suppressed (vibrations in SEM image < 3 nm) and an acceptable operation of the SEM was therefore made possible. Further, the vibrational influence of the pulse tube on the detector signal could be reduced significantly with the application of a SQUID that can be operated on the ADR stage (in the order of magnitude of 100 mK). This SQUID enabled the wires which were most affected by cooler vibrations to be expended. With the suppression of the vibrational influence and the improvement of the ADR cooling performance, the energy resolution was improved to 6.5 eV FWHM.

Due to non-linearities in the phase transition of a TES, the measured signal is

not linearly proportional to X-ray energy. Thus, the calibration of a TES detector system is problematic. In this thesis a method for calibrating the detector to an accuracy of the order of electron Volts using pulse shape analysis is introduced. This method is based on the calculation of the electrical energy of each pulse as defined by the electrothermal feedback of the detector. The achieved calibration accuracy of this method is well below the FWHM of an X-ray peak and further facilitates peak identification.

The absorber areas of the larger detectors used in this thesis were $250\,\mu\mathrm{m} \cdot 250\,\mu\mathrm{m}$ which is very small in contrast to the area of a typical semiconducting EDS detector ($10 - 30\,\mathrm{mm}^2$). The measured X-ray intensity is proportional to the covered solid angle of the detector ($\Omega = A/d^2$). Because the distance d between sample and detector is nearly similar for Si(Li) and TES detectors, the number of absorbed X-rays in the described TES detectors is quite small compared to Si(Li) detectors. Thus, the measurement time for standard EDS analysis can be unacceptably long when using TES detectors. Some methods such as mapping or the detection of small concentrations are therefore nearly impossible. In order to solve this problem a polycapillary X-ray lens was added to the system. This lens greatly increases the covered solid angle and improves the X-ray intensity by a factor of 120. Spectrum acquisition thus becomes sufficiently fast to enable analysis methods such as elemental mapping or the determination of dopant concentrations.

The most important feature of the Polaris TES-EDS system is the ability to resolve low-energy X-ray lines of material combinations important for semiconductor industry (e.g. W/Si, Ta/Si or TiN). With a typical energy resolution of about 10 eV, a clear separation of these lines can be shown.

The improved detection limit of TES detectors compared to Si(Li) detectors is another advantage for EDS analysis. The detection of elemental concentrations below 10^{-4} could be demonstrated. With a sufficiently long measurement time elements with even lower concentrations can be detected.

Further, preliminary measurements were done demonstrating the ability to detect the chemical shifting of emission lines. The chemical shift of the Si K lines in SiO_2 compared to the Si K lines in pure Si was measured. The results are in accordance with measurements done by WDS spectrometers. The ability to detect chemical shifts opens a completely new field in EDS analysis because it allows the detection of the chemical constitution of a small volumes in a specimen.

The two-dimensional image of the elemental distributions on a sample is called element mapping. A mapping is acquired by counting the number of characteristic X-rays as function of the electron beam position. The application of TES detectors for this method enables an improved peak separation in EDS mappings and additionally the background in element mappings is reduced.

Electron probe quantitation is the determination of elemental mass fractions in a specimen using the X-ray spectra. The mass fractions can be calculated using the theory of the generation of X-rays in a sample during to electron beam interaction. This method could be applied to the Polaris TES-EDS system and various examples

could be measured. The accuracy of the acquired results was sufficient because the measurements were mainly limited by statistical errors and therefore a function of measurement time.

A special application of electron probe quantitation is the thickness determination of thin surface layers. As example a 7.7 nm thick SiO_2 layer on a Si bulk was measured. The calculated layer thickness had an error below 10 % of the layer specification that was mainly caused by the counting statistics of the measurements. With increased measurement times it is possible to deliver accurate thickness measurements of such thin layers.

The main tasks for the applications of TES detectors in an industrial environment could be achieved. An easy-to-use detector system was developed offering many advantages over traditional EDS instruments. For optimum performance of the Polaris detector system some further improvements are possible. For instance, an optimized polycapillary lens could help to decrease the distance between the pole piece of the SEM and the specimen. This would improve the imaging quality of the SEM and thus simplify the identification of small structures. Another advance would be the improvement of the detector resolution due to sharper and more linear phase transitions of the TES. This would lead to a better peak to background ratio and therefore a better detection limit. With an improved peak resolution also the routine analysis of chemical shifts could be enabled.

Appendix A

Special Terms and Abbreviations

ADR: *A*diabatic *D*emagnetization *R*efrigerator (see section 2.2)

Bremsstrahlung: Bremsstrahlung is generated by inelastic scattering of primary electrons. The electrons are decelerated due to this scattering. The energy lost due to the deceleration is emitted as X-rays with an continuous energy spectrum. The range of the spectrum is from nearly zero to the electron beam energy. Bremsstrahlung is the main source of background in the electron beam excited X-ray spectrum.

Count rate: The number of measured X-rays per time unit

Detection efficiency ϵ: ϵ is the ratio of detected to incident X-rays. It is typically a function of X-ray energy.

EDS: *E*nergy *D*ispersive X-ray *S*pectroscopy

Excitation Volume: Volume, where the electron energy is still larger than the ionization energy of a given element; it is therefore the volume where characteristic X-rays of the given element are emitted;

FWHM: *F*ull *W*idth at *H*alf *M*aximum; The FWHM is the energy range where the distribution of the measured X-ray energies has more than half the value of the maximum. For a gaussian distribution the FHWM is correlated with the standard deviation σ: $FWHM = 2.35 \cdot \sigma$

Interaction Volume: Volume where the interactions between primary beam electrons and specimen take place.

PTBR: *P*eak *T*o *B*ackground *R*atio

ROI: A region of interest (ROI) is a specified energy range typically of the magnitude of the detector FWHM and including a characteristic X-ray peak.

SEM: *S*canning *E*lectron *M*icroscope;

Si(Li) detector: Lithium-drifted silicon detector, used for EDS

Ω: The solid angle Ω is the ratio of the absorbing area of the detector to the distance between specimen and detector.

SQUID: *S*uperconducting *QU*antum *I*nterference *D*evice (see section 3.2)

TES: *T*ransition *E*dge *S*ensor

Working distance: The working distance is defined as the distance between the lower pole piece and the position of the sample at which the electrons are focussed onto the sample.

WDS: *W*avelength *D*ispersive *S*pectrometer

Z: Atomic number

Appendix B

Tables

Nr. of detector	1	2	3
Fabricated at	TU München	IPHT Jena	IPHT Jena
Type of thermometer	Ir/Au	Mo/PdAu	Mo/PdAu
Size of thermometer	$400\mu\text{m} \cdot 400\mu\text{m}$	$400\mu\text{m} \cdot 400\mu\text{m}$	$300\mu\text{m} \cdot 300\mu\text{m}$
Size of absorber	$250\mu\text{m} \cdot 250\mu\text{m}$	$250\mu\text{m} \cdot 250\mu\text{m}$	$130\mu\text{m} \cdot 130\mu\text{m}$
Transition temperature	110mK	160mK	160mK

Table B.1: Properties of the three different detectors used in the TES EDS system Polaris

Symbol	explanation
Ω	solid angle of detector
ϵ_{det}	detection efficiency
ω_A^l	fluorescence yield of level l of element A
g_A^l	weight of line resulting from ionization of level l of el. A
f	ratio between secondary and primary intensity
g_{ck}	Coster-Kronig transition rate
N_0	Avogadro's number
A_A	atomic mass of element A
Q_A^l	ionization cross section of level l of element A
N_e	number of incident electrons
Φ	depth distribution function of primary ionizations
ρz	mass depth
χ_A	$(\mu/\rho)_A \cdot cosec(\Psi)$ with (μ/ρ) mass absorption coefficient
Ψ	take off angle of detector

Table B.2: Explanation of the expressions in Eq. 1.13

Bibliography

[Ale99] A. Alessandrello et al., Phys. Rev. **82** (3), 513 (1999)

[And66] C. A. Anderson, M. F. Hasler, Proc. 4th Intl.Conf. on X-ray optics and Microanalysis, Hermann, Paris, 310, (1966)

[Bea67] J.A. Bearden, A. F. Burr, Rev. of Mod. Phys. **39**, 78 (1967)

[Bet33] H. A. Bethe, Handbook of Physics, Vol. 24, Springer, Berlin, p. 273, (1933)

[Cas51] R. Castaing, PhD thesis, University of Paris (1951)

[Cas55] R. Castaing, and J. Deschamps, J. Phys. Radium **16**, 304 (1955)

[Cas60] R. Castaing, Advances in Electronics and Electron Physics, Vol. XIII, L. Marton, ed., Academic Press, New York, 317 (1960)

[Dod68] C. G. Dodd and G.L. Glen, J. appl. phys. **39** (12), 5377 (1968)

[Dru01] D. Drung, Improved Direct-Coupled SQUID Read-Out Electronics with Automated Bias Voltage Tuning, IEEE Trans. Appl. Supercond. **11** (1), 880 (2001)

[Ens00] C. Enns, S. Hunklinger, Tieftemperaturphysik, Springer (2000)

[Fle04] Fleischmann et al, Nucl. Instr. and Meth. **A 520**, 27 (2004)

[Fri03] J. J. Friel, X-ray and image analysis in electron microscopy, second edition, Princeton gamma-tech, 2003

[Gal03] M. Galeazzi, D. McCammon, Microcalorimeter and bolometer model, J. Appl. Phys. **93** (8), 4856 (2003)

[Gol03] J. Goldstein, D. Newbury, D. Joy, C. Lyman, P. Echlin, E. Lifshun, L. Sawyer, J. Michael, Scanning Electron Microscopy and X-ray Microanalysis, Kluwer Academic, New York, (2003)

[Gra77] G. Graeffe, H. Huslen and M. Karras, J. Phys. B: At. Mol. Phys. **10** , 3219 (1977)

[Höh98] J. Höhne, PhD thesis, Technische Universität München (1998)

[Hol01] C. Hollerith, Diploma thesis, Technische Universität München (2001)

[1] C. Hollerith, D. Wernicke, M. Bühler, F. v. Feilitzsch, M. Huber, J. Höhne, T. Hertrich, J. Jochum, K. Phelan, M. Stark, B. Simmnacher, R. Weiland, W. Westphal, Nucl. Instrum. and Meth. **A 520**, 606 (2004)

[Hov97] P. Hovington, D. Drouin, R. Gauvin, CASINO: A New Monte Carlo Code in C Language for Electron Beam Interaction- Part1: Description of the Program, Scanning Vol. 19, 1 (1997)

[Hub04] M. Huber, PhD thesis, Technische Universität München (2004)

[Hyp] http://hyperphysics.phy-astr.gsu.edu/hbase/solids/squid.html

[Hyp2] http://www.cxro.lbl.gov/optical.constants/atten2.html

[Irw95] K. D. Irwin, An application of electrothermal feedback for high resolution cryogenic particle detection, Appl. Phys. Lett. **66**(15), 1998 (1995)

[Irw98] K. D. Irwin, G. C. Hilton, D. A. Wollman, and J. M. Martinis, J. of Appl. Phys., **83**(8), 3978 (1998)

[Isa04] C. Isaila, Diploma thesis, Technische Universität München (2004)

[Joh70] G. G. Johnson, Jr., and E. W. White, X-ray Emission and keV Tables for nondiffractive analysis, ASTM Data Series DS 46, (1970)

[Joy95] D. Joy, Monte Carlo Modeling for Electron Microscopy and Microanalysis, Oxford University Press (1995)

[Par87] T. W. Parks, and C. S. Burrus, Digital Filter design, John Wiley & Sons, chapter 7, section 7.3.3, (1987)

[Pou91] J.L. Pouchou, F. Pichoir, Quantitative Analysis of homogeneous or Stratified Microvolumes Applying the Model PAP, ed. by K.F.J. Heinrich and D.E. Newbury, Plenum Press, New York, (1991)

[Prö95] F.Pröbst et al., J. of Low Temp. Phys. **100**, 69 (1995)

[Ree93] S.J.B. Reed, Electron Microprobe Analysis, 2nd edition, Cambridge university press, (1993)

[Rot04] K. Rottler, Diploma thesis, Technische Universität München (2004)

[Sch02] P. Schields et al., Powder Diffraction **17**(2), 70 (2002)

[Sei90] W. Seidel, PhD thesis, TU München (1990) and W. Seidel, D. Dummer, F. Pröbst, Low temperature detectors for neutrons and dark matter, Oxford 91, edited by C. Booth and G. L. Salmon, Edition Frontier, C48, (1991)

[Sie31] M. Siegbahn, Spektroskopie der Röntgenstrahlen, Julius Springer Verlag, (1931)

[Sim02] B. Simmnacher, R. Weiland, E. Langer, M. Bühler, J. Höhne, C. Hollerith, Proceedings of the 28th Symposium for Testing and Failure Analysis (ISTFA), Phoenix/AZ, November 2002, 87 (2002)

[Som77] A. Sommerfeld, Thermodynamik und Statistik, Verlag Harri Deutsch (1977)

[Wan98] C. Wang, G. Thummes, and C. Heiden, Performance Study on a two-stage 4K pulse tube cooler, Proceedings of Advances in Cryogenic Engineering, Vol. 43, edited by P. Kittel, Plenum Press, (1998)

[Web29] D. L. Webster, W. W. Nicholas and M. Siegbahn, International Critical Tables, E.W. Washburn, Ed. (McGraw-Hill Book Co., Inc. , New York 1929), Vol. 6, p. 35

[Wei04] D. Weill, J. Rice, Michael Shaffer, J. Donovan, Electron beam microanalysis theory and application, Lecture notes, university of oregon, (2004)

[Wie50] N. Wiener, Extrapolation, Interpolation and Smoothing of Stationary Time Series, The Technology Press and Wiley, New York (1950)

[Wol97] D.A. Wollman, K.D. Irwin, G.C. Hilton, L.L. Dulcie, Dale E. Newbury, John, M. Martinis, Journal of Microscopy **188**, 196 (1997)

[Wol00] D.A. Wollman, J.M. Martinis, S.W. Nam, G.C. Hilton, K.D. Irwin, D.A. Rudman, N.F. Bergren, S. Deiker, M.E. Huber, D.E. Newbury, Elec. Dev. Fail. Anal. News, **2** (4), 1 (2000)

[Yua99] J. Yuan, J.M. Pfotenhauer, Cryogenics **39** (4), 283 (1999)

Acknowledgements

At the end I want to thank all people that contributed to this work:

- To my bosses during this work:
  - Prof. Dr. Franz v. Feilitzsch, for the support and the backing of this work, his advice and many interesting talks about physics and also about forestry and hunting
  - Dr. Rainer Weiland, Infineon Technologies, for the encouragement of many new methods such as mapping and the graphical user interface, for discussions about detector physics and skitours and the advice in various matters
  - Dr. Jens Höhne, Vericold Technologies, for many hints and discussions and the organization of many parts of the MESA project
- To the members of E15:
  - Beatrice van Bellen, for the help in organizational matters and the assistance with the ARTEM proposal
  - Prof. Dr. Josef Jochum, for many talks about noise and the physics of TES detectors.
  - Dr. Michael S. Huber, for the unforgettable time when we started the first measurements of tunnel junctions in the Polaris (day and night) and the journey to Berlin.
  - Klemens Rottler, also for spending some time with me in the loneliness of the basement only with SEMs and tunnel junctions and for helpful hints for this thesis.
  - Dr. Walter Potzel, especially for the help and advice with the chapter about linearization of the detector signal
  - All other people of E15 for the always friendly atmosphere
- To the members of Vericold Technologies:

  - Dr. Matthias Bühler for many hints about the system, especially in the beginning of this work, where he was always willing to spend his time explaining the secrets of low temperature physics in general and the interiors of the Polaris spectrometer.
  - Kevin Phelan, for providing me with cooler control and data acquisition software, for the support of many new ideas with his programming skills and the improvement of this thesis concerning the Irish language
  - Doreen Wernicke for enduring the never ending problems of the detector production and the support with detectors for this work
  - Dr. Theo Hertrich for the construction of the new rotary valve holder

- To the members of Infineon Technologies:
  - Dr. Birgit Simmnacher, for organizing most of the used specimen, the organization of the MESA meetings that proved to be very helpful and the supervision of this work. Also thanks for having good humor all the time (especially in terms of safety).
  - Christian Isaila, for the time he endured me and the cellar in Perlach during his diploma thesis and the contribution to the improvements of Polaris especially his work for quantitative analysis
  - Matthias Brandstetter for the support at the measurement of the quantitation database
  - Zhu Qi for the beginning and the witty naming of 'SpecCheck'
  - To the members of FA 5, Giovanni Arcuti, Willi Argyo, Angela Collantes, Dr. Bodo Danzfuss, Dr. Hermann Doyen, Franz Hagl, Dieter Lesiak, Catrin Klein, Peter Meis, Uwe Papenberg, Markus Reiss, Hans Rettenmaier, Anneliese Stanciu, Ekkehard Wildenauer, Dr. Jesper Wittborn, for many samples and the perfect atmosphere where it was always a pleasure to work
  - To the members of the complete failure analysis lab Munich and their head Dr. Siegfried Görlich for the support of this work, samples and equipment

- To all other persons and institutes that supported me, especially:
  - Dr. Thorsten May, IPHT Jena for providing detectors
  - Christoph Wendt for the correction of this work
  - Dr. Ed Kenik for providing the NIST standard for our measurements
  - Florian Huber for providing the lava multi-element standard

- To everyone I forgot to mention, thanks for every help and support I received